NTNU – Trondheim
Norwegian University of
Science and Technology

Bearing capacity failure envelope of suction caissons subjected to combined loading

Fortsettelse fra prosjektoppgave

Erik Sørlie

Civil and Environmental Engineering
Submission date: June 2013
Supervisor: Gudmund Reidar Eiksund, BAT
Co-supervisor: Corneliu Athanasiu, Multiconsult

Norwegian University of Science and Technology
Department of Civil and Transport Engineering

NORWEGIAN UNIVERSITY OF SCIENCE AND TECHNOLOGY
DEPARTMENT OF CIVIL AND TRANSPORT ENGINEERING

Report Title: "Bearing capacity failure envelope of suction caissons subjected to combined loading"	Date: 10/6-2013 Number of pages 130 (I-XIII, 1-117)			
	Master Thesis	x	Project Work	
Name: Erik Sørlie				
Professor in charge/supervisor: Gudmund Eiksund and Steinar Nordal				
Other external professional contacts/supervisors: Corneliu Athanasiu				

Abstract:

The objective of the master thesis is to use the failure envelope approach to determine the ultimate capacities of a suction anchor, and to establish a strain-hardening elasto-plastic model in terms of loads and displacements at padeye.

Numerical analysis in Plaxis 3D has been executed for the suction anchor, which has formed a capacity surface in terms of combined loading at the padeye. General loading at padeye will result in six force components, which can be expressed by three independent variables due to constrained loading conditions. Empirical yield surfaces, that take all six force components into account, have been curve-fitted to the Plaxis results. The yield surfaces have been used together with load-displacement relations to establish an elasto-plastic formulation with respect to loads and displacements in terms of the padeye. The results were further generalized, and can be used to estimate the response of other suction anchors.

The elasto-plasticity has been implemented by isotropic hardening, governed by a curve-fitting hyperbola. The formulation was implemented in Excel as a spreadsheet that provided accurate results for most load combinations. The sheadsheet is applicable for both tensile and compression forces, and laod histories for up to 10 steps can be applied. Each load step in the spreadsheet was divided into 100 load increments. The spreadsheet was made in a general way, where the input parameters were the ultimate force components, the eccentricities to the neutral planes, the elastic stiffness coefficients and empirical curve-fitting coefficients with respect to both the yield surface and the hardening law.

Mesh refinements and hand calculations have been applied. Comparisons show that most load cases have an adequate convergence; however the torsional capacity was overestimated with about 50%. Analysis without an activated padeye showed that the overestimation was caused by the flow around mechanism close to the padeye. The author will recommened to model the anchor without a padeye for later studies, and rather apply a set of force vectors that give the same load.

Keywords:

1. Offshore Geotechnical Engineering
2. Suction Anchor
3. Combined loading
4. Elasto-plasticity

MASTER DEGREE THESIS

(TBA4900 Geotechnical Engineering, Mater Thesis)

Spring 2013

for

Erik Sørlie

Bearing capacity failure envelope of suction caissons subjected to combined loading

BACKGROUND

There is an increasing focus on use of the failure envelope approach to determine ultimate states of offshore suction caisson anchors subjected to combined loading (six components of force and moments). The reason for that is that this approach considers explicitly the independent load components and allows graphical interpretation of the safety factor associated to different load paths.

The master thesis will use the PLAXIS 3D model of a suction caisson anchor, developed in Project thesis, to determine the bearing capacity envelope (combination of vertical load, horizontal loads and moments that cause failure of the supporting soil). The results from PLAXIS 3D analyses will be used to determine the failure envelope and to express it analytically in non-dimensional form. Numerical experiments will be undertaken to study the possibility of establishing strain hardening elasto-plastic model in terms of forces and displacement (force resultant model).

Task description

In developed the Project thesis from 2012, using the PLAXIS 3D results, it was already established a relation (failure envelope) between horizontal and vertical component of the tension force at failure for a given geometry of a suction caisson and a given soil profile. It was also found that this relation can be approximated by a non-dimensional form for all element net refinements (number of elements).

The main goals with the master thesis are:

1. Perform a parameteric study to determine the optimum number of elements that ensures convergence and realistic results
2. Find out whether the suction caisson can be considered rigid (i.e. it only translates and rotates but has no deflections)
3. Find out non-dimensional analytical expression for failure envelope.
4. Study the possibility of establishing an elasto-plastic model in terms of forces and displacements. This requires establishing whether a yield surface and a hardening parameter can be established. For example if the analytical expression of the failure envelope in terms of vertical and horizontal load components at the pad eye is

$$(\frac{H}{H_{oult}})^a + (\frac{V}{V_{oult}})^b + (\frac{M_z}{M_{zoult}})^c = 1$$

it might be possible that yield surfaces can be expressed in terms of a hardening parameter (which can be mobilization degree f = τ/s_u) and if

Ho = Hoult*f , Vo = Voult*f, and Mzo = Mzoult*f , then the yield surface has the equation:

$$F = (\frac{H}{H_o})^a + (\frac{V}{V_o})^b + (\frac{M_z}{M_{zo}})^c - 1 = 0$$

In addition, the elastic force-displacement relationship must be defined as:

$$\{Q\} = \begin{Bmatrix} V \\ H \\ Mz \end{Bmatrix} = \begin{bmatrix} K11 & K12 & K13 \\ K21 & K22 & K23 \\ K31 & K32 & K33 \end{bmatrix} \cdot \begin{Bmatrix} \delta_{ve} \\ \delta_{he} \\ \theta_{ze} \end{Bmatrix} = [K] \cdot \{\delta_e\}$$

And a flow rule:

$$\{\delta_p\} = \lambda \cdot \{\frac{\partial F}{\partial Q}\}$$

The formulation of an elasto-plastic model can be used to determine the stiffness of suction caisson and to construct force-displacement curves along different loading paths.

Professor in charge: Gudmund Eiksund and Steinar Nordal

Other supervisors: Corneliu Athenasiu

Department of Civil and Transport Engineering, NTNU

Date: 06.06.2013

_____

Professor in charge (signature)

Preface

This report is a thesis performed in the spring of 2013 at Geotechnical Division at Norwegian University of Science and Technology, NTNU. It is an analytical report that contains analyses from Plaxis 3D, as well as an implementation of an elasto-plastic model.

The duration of the work on the thesis has been 21 weeks, included the Easter. The scope of the thesis corresponds to 30 credits, which equals one semester of work. The emphasis of the work has been the following:

- Literature study 20 %
- Modeling and interpretation in Plaxis 3D 30 %
- Establishment of an elasto-plastic model 30 %
- Report writing 20 %

I would like to thank my external supervisor Corneliu Athanasiu and Multiconsult AS for providing an interesting and challenging exercise and for given me good advices throughout the process.

I would also like to thank my supervisors at NTNU, Gudmund Eiksund and Steinar Nordal. Thanks to great discussions and good consulting, the work has become more exiting. I will also like to thank the rest of the geotechnical division and NTNU in general for five great years. The submission of the thesis implies that an era of my life is over. Thanks to you, I feel that I am ready for the next one.

When I started to work on the thesis, I wanted to produce a comprehensive report that could actually be used in practice. Weather I have succeeded or not is left to be determined. One thing has at least become more and more clear to me during the process; do not believe in the answers from a finite element study if you don't have many good reasons to do so.

I hope that the reader will find my thesis interesting, and maybe learn something as well. If there is something that you might wonder about, please do not hesitate to contact me.

Trondheim, 10th of June, 2013

_____

Erik Sørlie

Summary

The focus of the master thesis is to use the failure envelope approach to determine the ultimate capacities of a suction anchor, and to establish a strain-hardening elasto-plastic model in terms of loads and displacements at padeye.

Numerical analysis in Plaxis 3D has been executed for the suction anchor, which has formed a capacity surface in terms of combined loading at the padeye. The padeye is the connection between the mooring chain and the anchor, and is located about 2/3 of the anchor length below the seabed. The suction anchor had an aspect ratio L/D=5, positioned in normally consolidated soft clay, where undrained conditions with a linear strength profile were assumed. Six force components will be presented during general loading; three translation forces and three moments. Since the forces will be applied to the anchor through the padeye, the force components will have constraint relations, which make it possible to visualize to the response in terms of three independent variables.

Two empirical yield surfaces that accounted for all six force components were curve-fitted to the obtained capacity surface, and gave appropriate agreement. The average difference between one of the empirical yield surfaces and the corresponding Plaxis response were 0.70%. The yield surfaces were further used, together with load deflection relations, to establish an elasto-plastic model in terms of loads and deflections at padeye position. The formulation was implemented as a spreadsheet in Excel. The results were then generalized, so that the results can be applied to other suction anchors.

Mesh refinements and hand calculations were performed in order to ensure that the results from the numerical study were reasonable. The agreement was adequate to most load cases, however the torsional resisanse were overestimated with about 50%. The reason is that the flow-around mechanism that was developed around the padeye, gave an unrealistic resistance. An advice for later projects would then be to model the padeye either as a rigid link or simply model the padeye forces as a set of load vectors at the anchor.

The results showed that a misorientation angle of 5 degrees of the padeye with respect to the mooring chain will decrease the capacity with about 3%, while the capacity will be decreased with about 12% when the misorientation was 10 degrees. When a larger misorientation degree is present, the capacity is governed by the ultimate torsional resistance.

The results from the inclined loading showed that the capacity will increase from 0 to 20 degrees, while the capacity is governed by the ultimate vertical resistance when the inclination angle is 30 degree and more. The results also show that it would be beneficial to lower the padeye position with 2-3 meters.

The failure mechanisms can roughly be divided into three parts. The failure mechanism when the inclination angle is between 0 and 20 degrees is characterized by rotation about the base of the anchor. When the inclination angle is 30 degrees or more, the anchor will translate vertically, and a reversed end bearing mechanism is developed. However, when the torsional angle is 20 degrees or more, the anchor will rotate about its own axis.

The analyses use a linearly- perfectly plastic Mohr-Coulomb material model, and are calculated in terms of initial reference position.

Contents

1 Introduction 1

1.1 Background to the master thesis 1

1.2 The purpose of the master thesis 1

1.3 The limitations of the master thesis 1

1.4 Structure of the report 2

2 Offshore geotechnical engineering 3

2.1 Geotechnical engineering 3

2.2 Offshore geotechnical engineering 4

2.3 Platform types 5

2.3.1 Gravity based structures (GBS) 6

2.3.2 Jacket platforms 6

2.3.3 Jack-up platforms 7

2.3.4 Compliant towers 7

2.3.5 Tension-leg platforms (TLP) 8

2.3.6 FPSs and FPSOs 8

2.4 Applications in offshore geotechnical engineering 8

2.4.1 Piled foundations 8

2.4.2 Shallow foundations 9

2.4.3 Anchors 10

2.4.4 Gravity anchors 11

2.4.5 Suction anchors 11

2.4.6 Drag anchors 11

2.4.7 Suction embedded plate anchors 12

2.4.8 Dynamically penetrating anchors 12

3 Theory 13

3.1 Selected theory of soil mechanics 13

3.1.1 Stresses 13

3.1.2 The principle of effective stress 14

3.1.3 Lateral earth pressure 14

3.1.4 Failure criteria and drainage conditions 15

3.1.5 Bearing capacity 15

3.2 Research on suction anchors 17

3.2.1 Installation 17

3.2.2 Operational conditions 18
3.3 Theory of elasto-plasticity 25
3.3.1 Yield criterion 26
3.3.2 Flow rule 27
3.3.3 Hardening rule 27
3.4 The finite element method 28
4 Soil modeling 30
4.1 Modeling considerations 30
4.2 Soil parameters 30
4.2.1 Strength parameters 30
4.2.2 Stiffness parameters 32
4.2.3 Initial conditions 33
4.3 Properties of the system 33
4.4 Plaxis 3D 36
4.5 Soil volume 38
4.6 Failure definition 38
4.7 Mesh refinements 38
5 Results 41
5.1 Combined loading 41
5.1.1 Load-deflection curves 42
5.1.2 Failure mechanisms 45
5.1.3 Failure surfaces in two dimensions 48
5.1.4 Three-dimensional plots 51
5.2 Hand calculations 52
5.2.1 Horizontal capacity 52
5.2.2 Vertical capacity 53
5.2.3 Bending moment capacity 54
5.2.4 Torsional capacity 54
5.2.5 Stiffness 55
5.2.6 Summary of the hand calculations 55
5.3 Single-force components with Plaxis 3D 56
5.4 Stiffness of the anchor 60
5.5 Elastic soil response 61
5.6 Load cycles 63

5.7 Curve-fitting yield surfaces 65
5.7.1 The first curve-fitting yield surface 65
5.7.2 The second curve-fitting yield surface 67
6 Elasto-plastic formulation 75
6.1 Formulation 75
6.1.1 Compatibility 75
6.1.2 Stiffness and flexibility matrixes 75
6.1.3 Yield criterion 76
6.1.4 Flow rule 76
6.1.5 Hardening rule 77
6.1.6 Putting it all together 81
6.2 Implementation 83
6.2.1 Solution steps 83
6.2.2 Elasto-plastic spreadsheet 84
6.3 Elasto-plastic response 87
6.3.1 Response against Plaxis results 87
6.3.2 Two-way loading 89
6.3.3 Normality 89
6.4 Elasto-plasticity: Summary 90
7 Generalization 91
7.1 Non-dimensional results 91
7.2 Normalized strength 93
7.3 Non-dimensional stiffness 97
7.4 Elasto-plasticity generalization 101
8 Discussion 102
8.1 Modeling considerations 102
8.2 Reliability of the model 104
8.3 Observations of the capacities 106
8.4 Evaluation of the empirical data 107
8.5 How to apply the generalized results 108
9 Conclusion & further work 109
9.1 Conclusion 109
9.2 Further work 109
References 110

10 Attachments 112
10.1 Attachment A - Horizontal capacity (Deng & Carter, 2000) 113
10.2 Attachment B - Incremental displacements, horizontal planes 114
10.3 Attachment C - Flow around mechanism padeye, incremental displacements 115
10.4 Attachment D - Example elasto-plasticity 116
10.5 Attachment E - Deflection space Plaxis, β=0 117

Figures

Figure 1 - The first offshore installation, 1947 (Randolph and Gourvenec, 2011) 4
Figure 2 - Na Kita development, the world's deepest platform, around 2,000 meters (Randolph and Gourvenec, 2011) 4
Figure 3 - Gullfaks C - Gravity-based structure, 216 m depth (Randolph and Gourvenic, 2011)..... 4
Figure 4 - catenary, taut and vertical mooring systems..... 5
Figure 5 - Overview of anchoring types (Randolph and Gourvenic, 2011) 5
Figure 6 - Platform types; (a) Jack-up, (b) GBS, (c) Jacket, (d) Compliant tower, (e) TLP, (f) FPS (Wilson, 2003)..... 6
Figure 7 - Examples of GBS (Dean, 2009) 6
Figure 8 - Typical jacket (Dean, 2009) 7
Figure 9 - Jacket construction; (a) fabrication, (b) transportation, (c) upending, (d) pile construction, (e) deck and topside installation, (f) pipeline attached (Dean, 2009) 7
Figure 10 - Jack-ups; before and after installation (Dean, 2009) 7
Figure 11 - TLP (Randolph & Gouvenec, 2011) 7
Figure 12 - FPS and FPSO (Randolph & Gourvenec, 2011) 8
Figure 13 - Steel jacket with driven piles - North Rankin A (Randolph, Gourvenec, 2011)..... 8
Figure 14 - Flow around mechanism (Randolph & Gourvenec, 2011) 9
Figure 15 - Failure mechanism short pile, horizontal loaded (Randolph & Gourvenec, 2011) 9
Figure 16 - Different applications with shallow foundations. (a)-(b); Gravity-based structures, (c); Tension-leg platform, (d); Jacket, (e); Subsea frame (Randolph & Gourvenec, 2011) 9
Figure 17 - Typical jack-up platform with corresponding spudcan foundations (Randolph & Gourvenec, 2011)..... 10
Figure 18 - Buoyant platforms (Randolph & Gourvenec, 2011) 10
Figure 19 - Gravity box anchor (Randolph & Gourvenec, 2011)..... 11
Figure 20 - Suction caissons for Laminaria field (Randolph & Gourvenec, 2011)..... 11
Figure 21 - Vertically loaded anchor (Randolph & Gourvenec, 2011) 11
Figure 22 - Fluke anchor (Randolph & Gourvenec, 2011)..... 11
Figure 23 - Suction embedded plate anchor (Randolph & Gourvenec, 2011) 12
Figure 24 - Typical dynamically penetrating anchors (Randolph & Gourvenec, 2011) 12
Figure 25 - Stresses in space (Plaxis, 2010) 13
Figure 26 - Stress zones with Mohr-Coulomb (Emdal et al. 2004) 15
Figure 27 - Installation stages with suction anchor (Randolph & Gourvenec, 2011) 17
Figure 28 - Plug stability (Randolph & Gouvenec, 2011)..... 17
Figure 29 - Failure mechanisms: (a) drained, (b) partly drained, (c) undrained conditions (Thorel et al., 2005)..... 18
Figure 30 - Current-induced torsion (Lee et al., 2005)..... 20
Figure 31 - Failure mechanisms for horizontally loaded suction anchors: (a) translational movement, (b) rotational movement, (Randolph & Gourvenec, 2011)..... 21
Figure 32 - Upper and lower bound solution flow-around mechanism (Martin & Randolph, 2006) 21
Figure 33 - Horizontal capacity (Randolph et al., 1998)..... 22
Figure 34 - Capacity with padeye positions (Supachawarote et al., 2004) 22
Figure 35 - HV-load space (El-Sherbiny et al. 2005) 23
Figure 36 - HV-load space (Taiebat & Carter (2005) 23

Figure 37 - Normalized HVT-space (Taiebat & Carter (2005) *24*
Figure 38 - Vertical loaded pile, Poisson's ratio of 0.5 (Poulos & David, 1974) *24*
Figure 39 - Lateral fixed loaded pile (Poulos & David, 1974) *25*
Figure 40 - Elasto-plastic response: (a) material without initial yielding plateau, (b) elastic-perfectly plastic response, (c) hardening material (Irgens, 2008) *26*
Figure 41 - Yield criteria in ∏-plane; von Mises, general yield criterion and Tresca (Irgens, 2008) *27*
Figure 42 - Kinematic and isotropic hardening (Irgens, 2008) *27*
Figure 43 - Shear strength profile *31*
Figure 44 - Thixotropy strength ratio (Jostad & Andersen, 2002) *31*
Figure 45 - Linearly elastic-perfectly plastic material model (Plaxis, 2010) *33*
Figure 46 - Geometry suction anchor. Dimensions in meters when not specified *34*
Figure 47 - Relation between the translational forces *35*
Figure 48 – Elastic and plastic planes and eccentricities *36*
Figure 49 - Soil elements with Plaxis 3D (Plaxis, 2010) *36*
Figure 50 - Area elements with Plaxis 3D (Plaxis, 2010) *36*
Figure 51 - Illustration of interface elements with Plaxis 3D (Plaxis, 2010) *37*
Figure 52 - Mesh refinements; (a) 4,900 el. (b) 11,900 el. (c) 20,500 el. (d) 53,700 el. (e) 182,000 el. . *39*
Figure 53 - Convergence - failure load against number of soil elements *40*
Figure 54 - Locations were a dense mesh is required *40*
Figure 55 - Analyses overview *41*
Figure 56 - Load-deflection curve, β=0 degrees *42*
Figure 57 - Load-deflection curve, beta=5 degrees *43*
Figure 58 - Load-deflection, β=10 degrees *43*
Figure 59 - Load-deflection curve, β=20 degrees *44*
Figure 60 - Load-deflection curve, beta=45 deg *44*
Figure 61 - Load-deflection curve, β=90 degrees *45*
Figure 62 - Incremental strains, β=0 degrees: (a) α=0 degrees, (b) α=20 degrees, (c) α=45 degrees, (d) α=90 degrees *46*
Figure 63 - Incremental disp., β=0 degrees: (a) α=0 degrees, (b) α=20 degrees, (c) α=45 degrees, (d) α=90 degrees *47*
Figure 64 - Incremental displacements anchor,β=0: (a) α=0, (b) α=10, (c) α=20, (d) α=30, (e) α=45, (f) α=60, (g) α=90 ..... *48*
Figure 65 - HV space *48*
Figure 66 - Failure load P with the angles alpha and beta *49*
Figure 67 - HV space, failure defined as 5 m deflection *50*
Figure 68 - Yield surface in HV space; deflection criteria: 0.2 m, 0.4 m, 0.6 m, 0.8 m and 1 m *50*
Figure 69 - HxHyV space *51*
Figure 70 - P-αβ-space *51*
Figure 71 - Horizontal capacity (Randolph, 1998) *52*
Figure 72 - Factor flow-around mechanism (Martin & Randolph, 2006) *52*
Figure 73 - Diagrams for the suction anchor *53*
Figure 74 - Influence factor axially loaded pile (Poulos & David, 1974) *55*
Figure 75 - Parametric study of ez *57*
Figure 76 - Incremental displacements; parametric study of ez *58*
Figure 77 - Load-deflection curves *59*

Figure 78 - Load-displacement curve parametric stiffness *61*
Figure 79 - Load deflection; deflections measured in the x-direction *62*
Figure 80 - Load deflection; deflection measured in the y-direction *62*
Figure 81 - Load deflection; deflection measured in the z-direction *63*
Figure 82 - Loads and deflections in the x-direction *64*
Figure 83 - Loads and deflections in the y-direction *64*
Figure 84 - Loads and deflections in the z-direction *64*
Figure 85 - Strip load; hand calculated and simplified *67*
Figure 86 - Reduction due to padeye position *69*
Figure 87 - Yield surfaces, β=0 degrees *70*
Figure 88 - Yield surfaces, β=5 degrees *71*
Figure 89 - Yield surfaces, β=10 degrees *71*
Figure 90 - Yield surfaces, β=20 degrees *72*
Figure 91 - Yield surfaces, β=45 degrees *72*
Figure 92 - Yield surfaces, β=90 degrees *73*
Figure 93 - Plaxis results versus yield surface 2 ..... *74*
Figure 94 - Empirical curve fitting for hardening; loading in the x-direction *78*
Figure 95 - Empirical curve fitting for hardening; loading in the y-direction *79*
Figure 96 - Empirical curve fitting for hardening; loading in the z-direction *79*
Figure 97 - Empirical coefficient values hyperbola *80*
Figure 98 - Hardening curve, α=30 degrees, β=10 degrees; interpolated and optimized based on three LC, hyperbola *80*
Figure 99 - Hardening curve, α=30 degrees, β=10 degrees; weighted interpolation and optimized based on three LC *81*
Figure 100 - Elasto-plastic response; Plaxis and empirical results, β=0 degrees *87*
Figure 101 - Elasto-plastic response; Plaxis and empirical results, β=10 degrees *88*
Figure 102 - Load cycle in the x-direction; Plaxis and empirical isotropic response *89*
Figure 103 - Normality; plastic displacement vectors *90*
Figure 104 - Non-dimensional HV space *92*
Figure 105 - Non-dimensional capacity *92*
Figure 106 - Vertical capacity factor; wall roughness = 0.4, 0.6, 0.8, Nc=9, W'/(LDsu)=0.54, su(L)/su=1.89 ..... *93*
Figure 107 - Normalized results *93*
Figure 108 - Normalized HV space with constant mobilized torque *95*
Figure 109 - Parametric padeye positions, ez=0-5 meters *96*
Figure 110 - Plaxis results compared to hand calculations *96*
Figure 111 - The suction anchor; difference between elastic and plastic eccentricities *100*
Figure 112 - Response caused by applied bending moment; (a) failure mechanism, (b) linearly-elastic response *101*
Figure 113- Updated and unchanged mesh for vertical load case *102*
Figure 114 - Updated and unchanged mesh for the load case pointed in y-direction *103*
Figure 115 - Results from hand calculations and from Plaxis *104*
Figure 116 – Respnce with and without the padeye with respect to torsion, inc disp; (a) with padeye (b) without padeye, (c) response *105*
Figure 117 - Comparisons yield surfaces *107*

Tables

Table 1 - Mesh refinements 39
Table 2 - Failure loads from padeye loads 42
Table 3 - Results from hand calculations 56
Table 4 - Eccentricities and ultimate forces 59
Table 5 - E-modulus load cases 60
Table 6 - Empirical coefficients 66
Table 7 - Empirical coefficients 70
Table 8 - Input parameters 85
Table 9 - Load history 85
Table 10 - Calculation process for Load Step 1, which is further divided into 100 smaller increments 86
Table 11 - Output data 86

1 Introduction

1.1 Background to the master thesis

In recent years, the offshore industry has moved towards deeper waters. Floating platforms have become more common, and triggered new geotechnical solutions, like the suction anchor that is the subject of the master thesis. The anchor will be subjected to combined loads from the platform, caused by environmental loads. The forces are applied to the system through a connection called a padeye.

The master thesis is an extension of a project work last semester by the same author. The project focused on the ultimate capacity of a suction anchor subjected to combined loads in undrained condition. The analysis from that project is replaced with new analyses; the master thesis will for that reason be an independent work.

1.2 The purpose of the master thesis

The purpose of the master thesis is to determine the failure envelope and to establish an elasto-plastic model of a suction anchor for combined loads by numerical analyses. Six force components will be presented during general loading; one vertical and two horizontal forces, two bending moments and a torsional moment. Since the forces will be applied to the anchor through the padeye, the force components will have constraint relations. The interaction between these constraint forces will form a yield surface in the loading space. The numerical yield surface will be approximated empirically by curve fitting. The yield surface, together with load-deflection relations, will be used to determine the elasto-plastic formulation in terms of padeye loads and deflections. The elasto-plastic formulation will be at a macro level, and measure the relation between padeye forces and displacements, rather than the usual relation between stresses and strains.

A suction anchor will always have some degree of misorientation due to the installation. The misorientation of the padeye with respect to the plane of the mooring chain induces a torsional moment. One of the aims of the thesis is to determine the impact on the torsional angle due to the response.

The numerical analysis will be carried out in Plaxis 3D. In order to obtain results with a sufficient reliability, mesh refinements and hand calculations will be executed. It will also be studied whether the anchor can be considered rigid, which is important for the soil-structure interaction.

The results from the analysis will also be presented in a non-dimensional matter, so that the work can be applied to similar situations.

1.3 The limitations of the master thesis

The work is limited to one specific suction anchor, with a length-to-depth ratio equal to 5. The analysis is limited to the undrained condition, where the undrained strength of the soil is almost proportional to the depth. The soil has been modeled with a linear-perfectly plastic Mohr-Coulomb material model. The forces are applied to the system through a load vector at the padeye, which is located almost 2/3 of the length of the anchor from the anchor top. The load vector varies from 0 to 90 degrees with respect to the padeye and the mooring chain and from 0 to 90 degrees between the horizontal plane and the inclination angle.

1.4 Structure of the report

The report has the following structure:

Chapter 2 provides an introduction to the topic and offshore geotechnical engineering in general.

Chapter 3 is the theoretical chapter. Basic geotechnical theory, research on suction anchors, elasto-plastic theory and basics in finite elements will be presented here.

Chapter 4 covers the soil modeling. The soil and structure parameters will be covered, as well as the model for the report. Plaxis 3D will be discussed briefly and mesh refinements are addressed in this chapter, since these are essential for convergence.

Chapter 5 covers the results. The results from the different load cases from Plaxis 3D will be presented, and some failure mechanisms will be shown. The results will be approximated numerically by curve fitting, and the elastic stiffness of the system will be constructed.

Chapter 6 is devoted to the elasto-plastic formulation. The formulation by means of deflections and loads applied at padeye, the implementation of the formulation and the results will be presented.

Chapter 7 gives the results in a generalized way, so that the results from the thesis can be used regarded to other suction anchors. The results will also be presented in a non-dimensional way. Results from hand calculations will also be included.

Chapter 8 discusses the results and the modeling considerations. The results and their reliability, the empirical curve fitting and the elasto-plastic formulation will be discussed. In addition, guidelines for applying the work to other projects will be given.

Chapter 9 concludes the work and outlines proposals for further work.

2 Offshore geotechnical engineering

This chapter provides an introduction to the subject of suction anchors. Firstly, an overview of geotechnical engineering will be presented, and then offshore geotechnical engineering will be introduced. Finally, a summary of applications in offshore geotechnics will be presented.

2.1 Geotechnical engineering

Geotechnical engineering deals with the physical properties of the soil. The objective of a geotechnical calculation is usually to ensure adequate stability of the system and evaluate the corresponding deformation. Geotechnical engineering is a large field and contains several applications like:

- Slope stability
- Settlements calculations
- Seepage analysis
- Bearing capacity
- Earth pressure analysis

The disciplines of geotechnics are applied to all civil engineering problems:

- Roads and railways
- Natural slopes
- Dam engineering
- House and building design
- Bridge design
- Tunneling
- Platform design
- Port facilities

In all applications, it is essential to obtain information about the physical properties of the site, and laboratory tests are usually performed prior to design. Unlike when dealing with structural materials, the uncertainty in material behavior is a large consideration. (Wood, 2009)

2.2 Offshore geotechnical engineering

Randolph & Gourvenec (2011) provides a comprehensive introduction of the field, and is the reference most widely used thoughtout this chapter.

Offshore geotechnical engineering is a relatively young discipline, the first fixed installation being installed in 1947. Today, there are more than 7,000 platforms around the world. Developments in recent years have moved towards deeper waters. In 1970, the definition of deep water was 50-100 meters, while the definition today is 500 meters and deeper. (Randolph & Gourvenec, 2011)

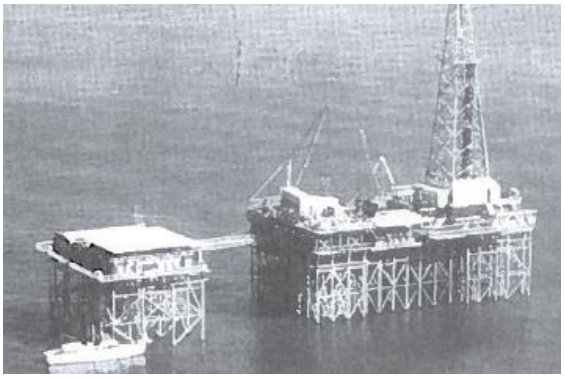

Figure 1 - The first offshore installation, 1947 (Randolph and Gourvenec, 2011)

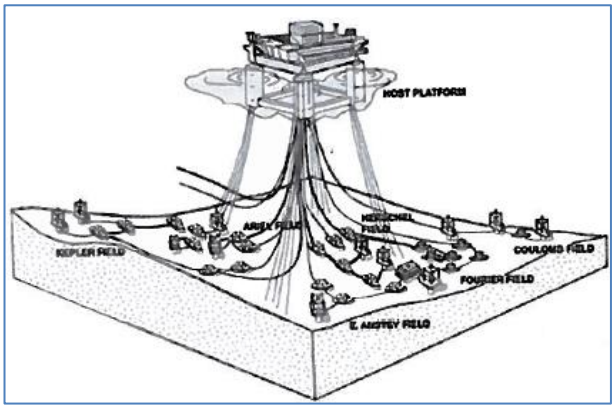

Figure 2 - Na Kita development, the world's deepest platform, around 2,000 meters (Randolph and Gourvenec, 2011)

The principles in offshore geotechnics are the same as for traditional geotechnics, although there are some differences:

- Site investigations are more expensive.
- Soil conditions are often more difficult
- Structural loads are usually significantly larger
- The focus is more on capacity rather than deformations, although the stiffness is important for the dynamical response of the system

Platforms can be divided into two groups: Fixed platforms and floating platforms. The fixed platform can further be divided into jackets and gravity-based structures. Jackets usually have a foundation concept consisting of pile groups in each corner. Traditionally, gravity-based structures have been directly embedded is permitted by beneficial soil conditions. However, when depths became larger, and soil conditions became less favorable, bucket foundation was adopted.

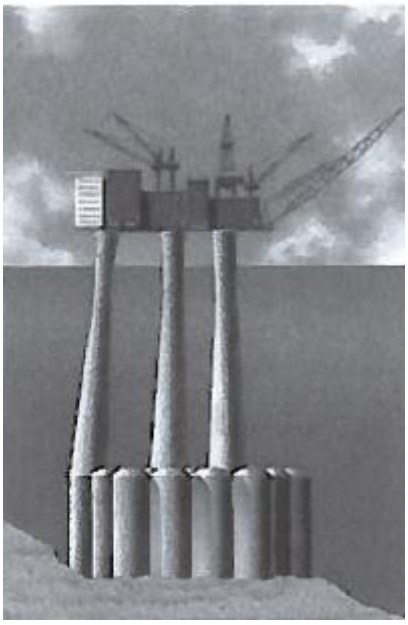

Figure 3 - Gullfaks C - Gravity-based structure, 216 m depth (Randolph and Gourvenic, 2011)

In deeper waters, floating platforms are preferable. The anchoring keeps the platform in position. The mooring chain between the platform and the anchoring system can be either loose or taut. When a catenary mooring system is applied, the cables are resting on the seabed, thus imposing large horizontal loads on the anchors. For a taut mooring system, the load inclination is usually more towards the vertical. The load inclination in the mooring system may for that reason vary from horizontal to vertical, depending on the mooring system. (Randolph & Gourvenec, 2011)

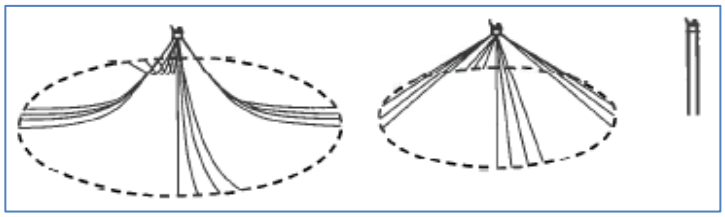

Figure 4 - catenary, taut and vertical mooring systems (Randoph & Gourvenec, 2011)

As a consequence of increasingly deeper waters, new anchoring systems have been developed for floating platforms:

- Anchor piles
- Suction caisson
- Suction embedded plate anchors
- Dynamically penetrating anchors

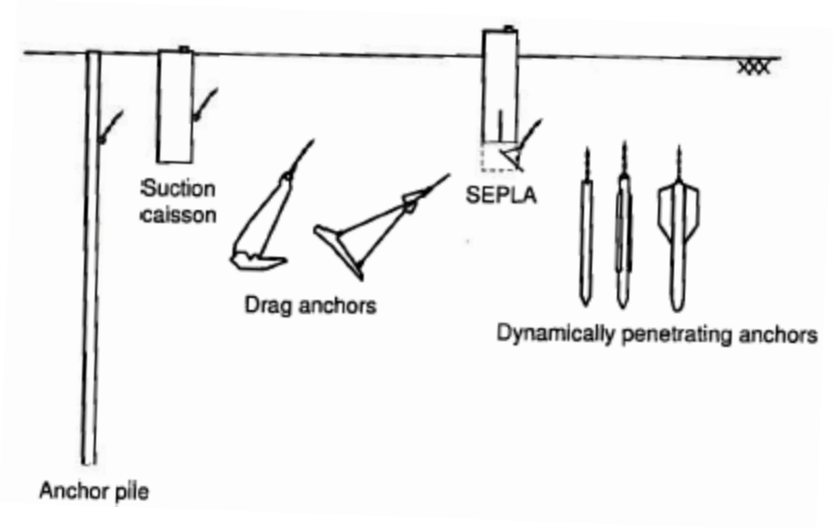

Figure 5 - Overview of anchoring types (Randolph and Gourvenic, 2011)

2.3 Platform types

There are numerous platform types, and which platform is best suited for a given project depends on several factors. Some commonly used platform types will be introduced in the following sections.

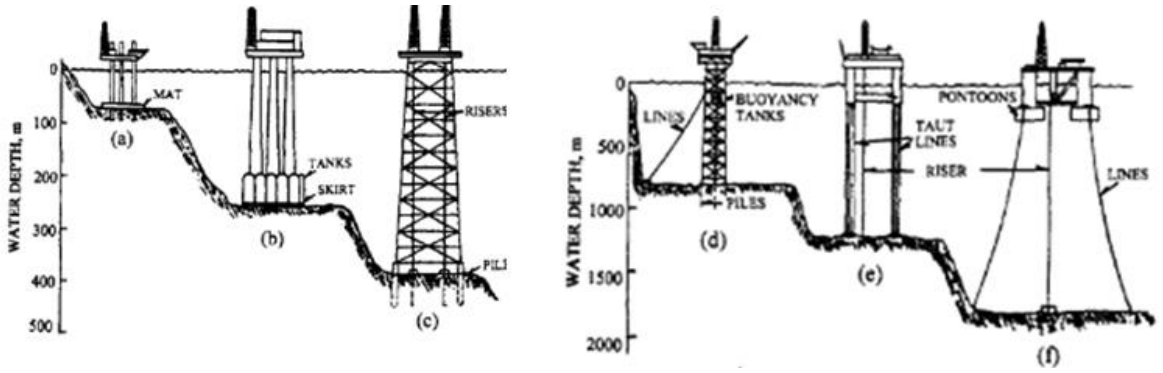

Figure 6 - Platform types; (a) Jack-up, (b) GBS, (c) Jacket, (d) Compliant tower, (e) TLP, (f) FPS (Wilson, 2003)

2.3.1 Gravity based structures (GBS)

Gravity based structures are large concrete platforms using their weight to sustain the environmental loads. The structures are either installed directly at the seabed, or on concrete buckets. GBSs have been used in waters of up to 300 meters. The topside is supported by one or more concrete legs. In the case of bucket foundations, installation is achieved by self-weight and suction, when required. (Dean, 2009)

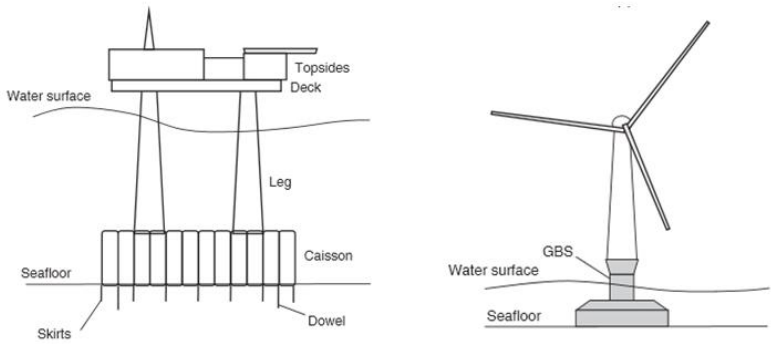

Figure 7 - Examples of GBS (Dean, 2009)

2.3.2 Jacket platforms

Jackets are the most commonly used platform type for offshore facilities. The jacket consists of an open framed steel structure, with legs horizontal bracing and diagonal bracing. Jackets are usually supported by piles, but alternatives like suction anchors have also been applied. In some cases, the jacket will temporarily be supported by mudmats before pile installation. The piles are then driven, and a grouted connection between the mudmats and the piles is installed. The deck, the topside and the pipeline are then installed, and the structure is subsequently ready to sustain the environmental loads. (Dean, 2009)

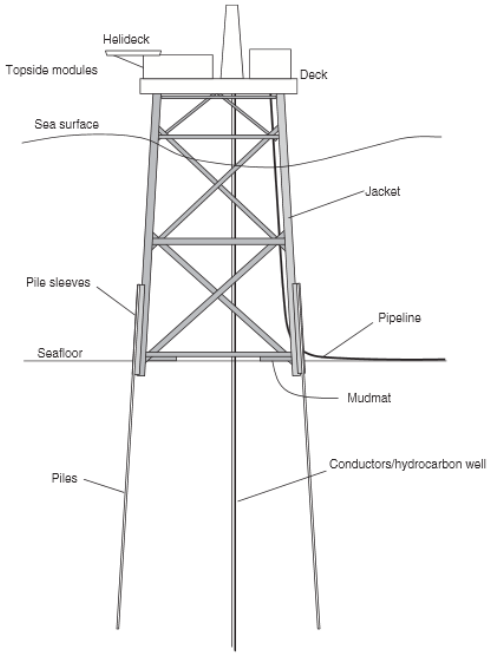

Figure 8 - Typical jacket (Dean, 2009)

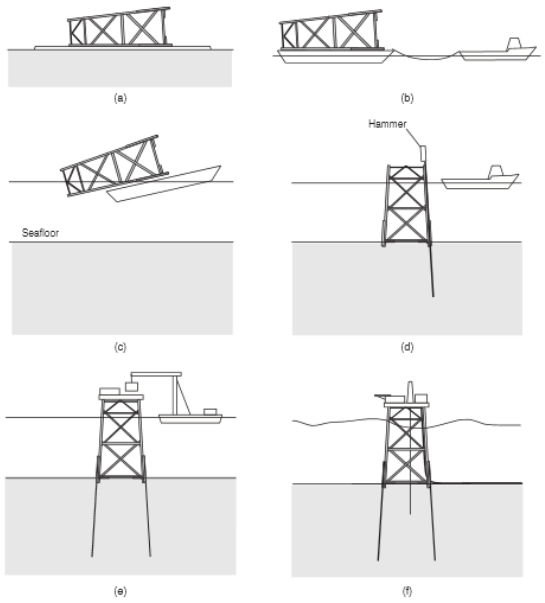

Figure 9 - Jacket construction; (a) fabrication, (b) transportation, (c) upending, (d) pile construction, (e) deck and topside installation, (f) pipeline attached (Dean, 2009)

2.3.3 Jack-up platforms

The jack-up platform is a mobile platform that consists of a topside with holes that are attached to at least three framed legs. The framed legs are attached to circular shallow foundations called spudcans, which may have a diameter up to 20 meters. Jack-ups can operate in waters of up to approximately 150 meters. Firstly, the topside with corresponding legs is floated to the desired position, where the legs are lowered and penetrated into the seabed. After installation, a proof load is applied to the system, to ensure that the foundation will have sufficient capacity. (Dean, 2009)

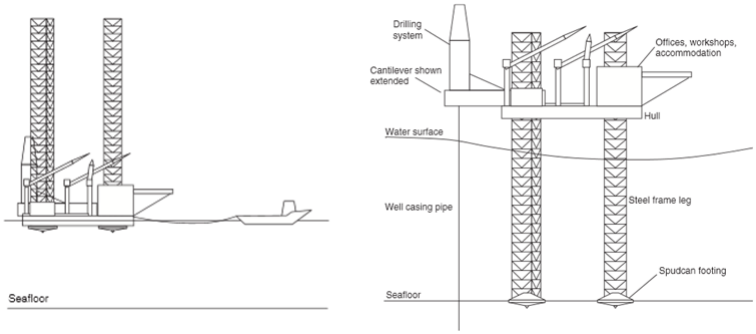

Figure 10 - Jack-ups; before and after installation (Dean, 2009)

2.3.4 Compliant towers

The compliant tower is a platform suited for waters of 300-800 meters, consisting of a tubular steel truss. The structure is much lighter than a jacket structure, and is designed to flex with the waves. The structure may be strengthened by laterally spreading mooring chains supported by anchors. The truss is usually supported by piles. Due to the flexible response, the crew is evacuated when storms and hurricanes are expected. (Wilson, 2003)

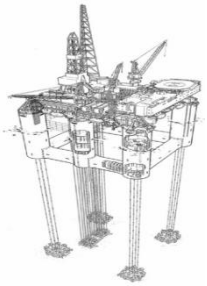

Figure 11 - TLP (Randolph & Gouvenec, 2011)

2.3.5 Tension-leg platforms (TLP)

The tension-leg platform is a floating structure, supported by vertically taut cables. The cables are designed to remain taut for all loadings. The platform has a large mass, which gives a slight response due to the environmental loads. The platform can be economically competitive in waters of between 300-1200 meters. The cables are usually fixed to foundations anchored by driven piles. In the mid-1990s, 11 TLPs had been installed; three in the North Sea and eight in the Gulf of Mexico. (Wilson, 2003)

2.3.6 FPSs and FPSOs

In ultra-deep waters, floating production systems (FPS) and floating production, storage and offloading platforms (FPSO) may be attractive solutions. The platforms are linked to subsea wells, which are fixed to the seabed. The floating production platforms will receive and process oil from subsea wells; often from several fields. The deepest platform currently installed is a FPS, at about 2,000 meters. Many FPSOs are converted oil tankers. The FPSO processes and stores the oil from several subsea wells. Both types of platform are anchored. (Leffler et al. 2011)

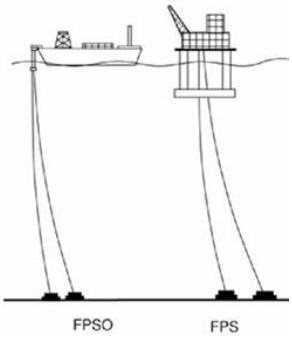

Figure 12 - FPS and FPSO (Randolph & Gourvenec, 2011)

2.4 Applications in offshore geotechnical engineering

This section will introduce foundation solutions commonly used for offshore platforms. The choice of solution depends on several factors. Soil conditions are of great importance, and several different foundation solutions might be appropriate for any given platform type.

2.4.1 Piled foundations

Piled foundation is an attractive solution in situations where soft soil and high horizontal loads are present. The piles will then transfer the structural loads to layers with increased strength. Piles are especially common for jackets, but might also be used for anchoring floating facilities like TLPs. The piles will then be subjected to pull-out forces. The piles are normally installed by driven construction regarded to offshore facilities. (Randolph & Gourvenec, 2011)

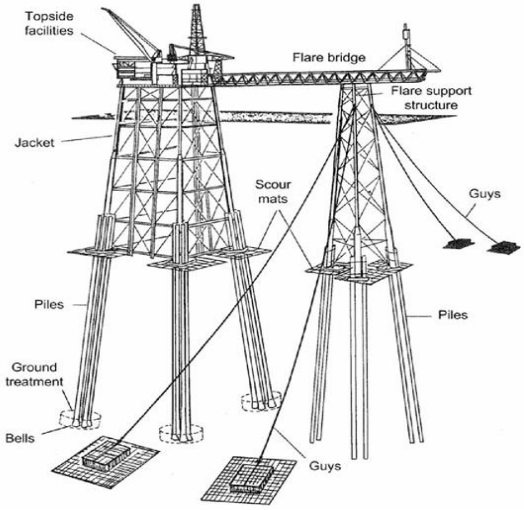

Figure 13 - Steel jacket with driven piles - North Rankin A (Randolph, Gourvenec, 2011)

Piles in the offshore context usually take a large portion of horizontal loads. However, the interaction between the vertical and the horizontal loads for slender piles is usually limited, since the horizontal component is mostly taken by the upper part, while most of the vertical component is taken by the lower part of the pile. (Randolph & Gourvenec, 2011)

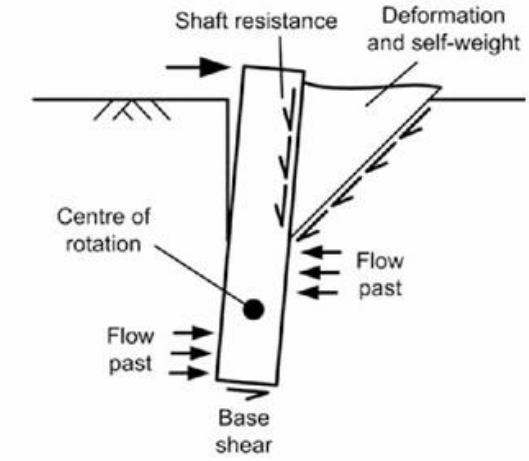

Figure 15 - Failure mechanism short pile, horizontal loaded (Randolph & Gourvenec, 2011)

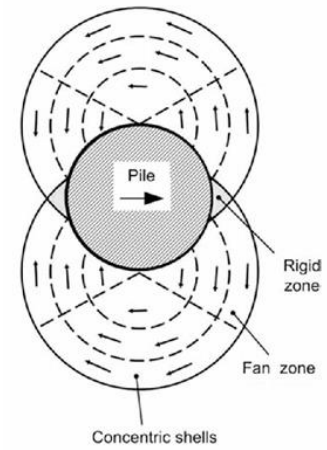

Figure 14 - Flow around mechanism (Randolph & Gourvenec, 2011)

2.4.2 Shallow foundations

Shallow foundations are advantageous when soil conditions at the seabed are favorable. Shallow foundations are often applied with jackets, gravity-based structures and jack-ups. Jackets are often supported by steel mudmats before the installation of piles. Gravity-based structures are either installed directly on the seabed or on bucket foundations. Jack-ups are usually supported by spudcans, which are circular plates that are, during installation, pushed until the desired capacity is achieved. (Randolph & Gourvenec, 2011)

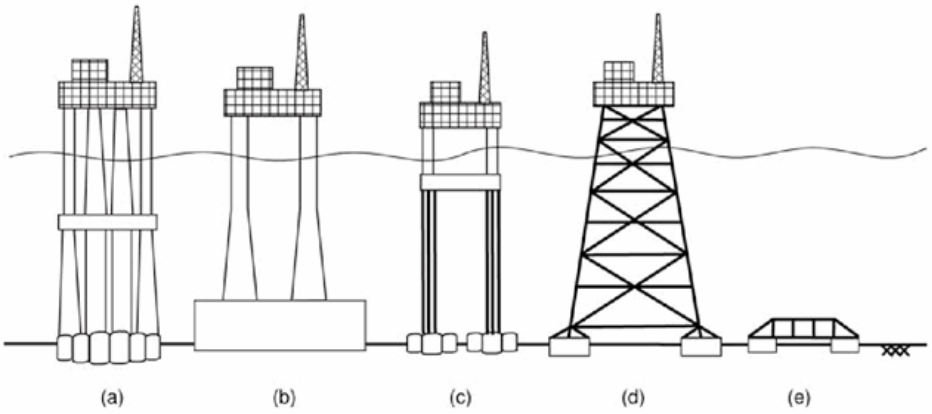

Figure 16 - Different applications with shallow foundations. (a)-(b); Gravity-based structures, (c); Tension-leg platform, (d); Jacket, (e); Subsea frame (Randolph & Gourvenec, 2011)

In the early development of gravity-based structures, soil conditions were beneficial due to heavily over-consolidated soil, and direct foundations were used. Later on, when the offshore industry moved towards deeper waters, soil conditions became less favorable and bucket foundations were required. The buckets are installed by self-weight only, in cases where the weight of the platform is adequate relative to the surrounding soil. Otherwise, suction will be applied in the final stage of installation. In case of floating facilities, suction is usually applied during installation. (Randolph & Gourvenec, 2011)

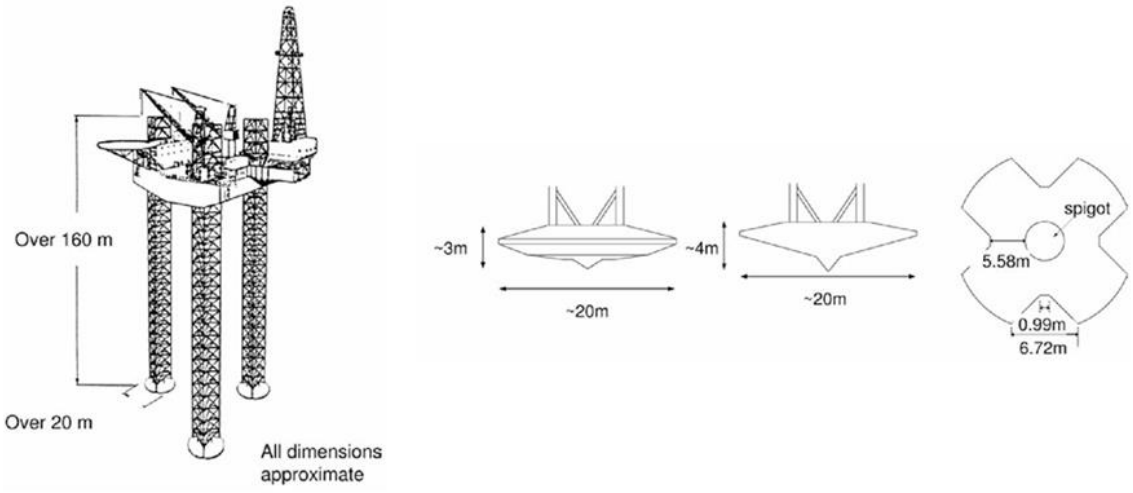

Figure 17 - Typical jack-up platform with corresponding spudcan foundations (Randolph & Gourvenec, 2011)

2.4.3 Anchors

Anchors are required to keep floating facilities in position. Floating facilities are suited for deep waters, where fixed platforms would not be economical. (Wilson, 2003)

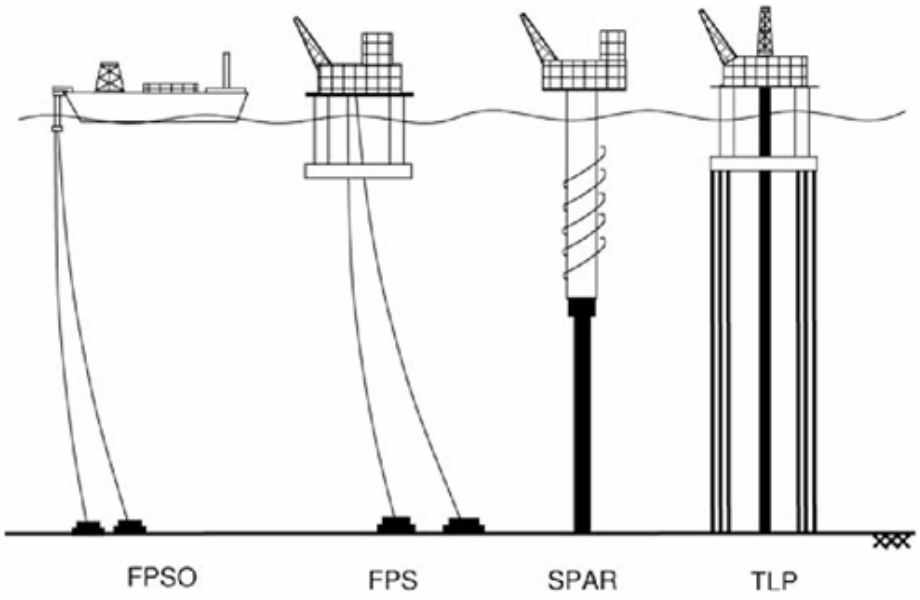

Figure 18 - Buoyant platforms (Randolph & Gourvenec, 2011)

The increasing focus on deep waters has triggered new anchor solutions. The loads from the platform are transferred to the anchor system by mooring chains that are attached to an amplified connection. The cables between the platform and the anchors can be either taut or loose. The appropriate foundation solution depends on the loading and the soil conditions. (Randolph & Gourvenec, 2011) The most common anchor systems will now be presented separately, although anchor piles will not be covered, since these have already been presented.

2.4.4 Gravity anchors

Gravity anchors can be applied if the required holding capacity is limited. The capacity is generated from dead weight and friction between the anchor and the seabed. A large portion of the dead weight is often due to filled rocks. (Randolph & Gourvenec, 2011)

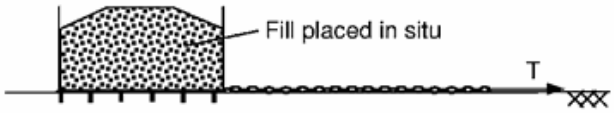

Figure 19 - Gravity box anchor (Randolph & Gourvenec, 2011)

2.4.5 Suction anchors

Suction anchors are large steel cylinders, with a typical length-to-depth ratio of 2-6. Suction anchors are most commonly used with FPSs and FPSOs. Suction anchors are installed in two steps; firstly the anchor penetrates by self-weight, then suction is applied by pumping water out of the top. One of the advantages of suction anchors is the simple installation that accurately puts the anchor in position. (Randolph & Gourvenec, 2011) The research on suction anchors will be covered in chapter 3.2.

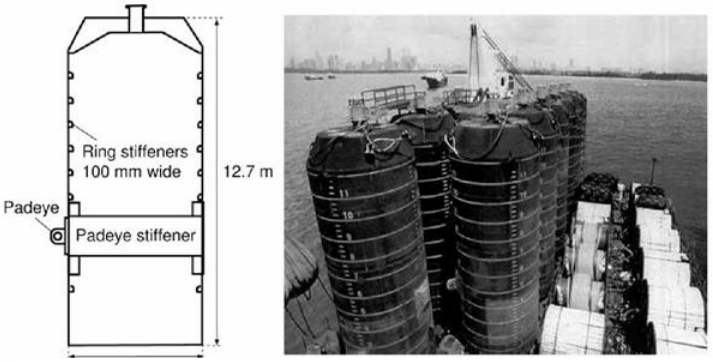

Figure 20 - Suction caissons for Laminaria field (Randolph & Gourvenec, 2011)

2.4.6 Drag anchors

Drag anchors are characterized by their installation, where the anchor is positioned by a drag length. The anchors are relatively light and have a large capacity-to-weight ratio. The capacity of drag anchors comes from the soil in front of the anchor. Drag anchors can further be divided into fluke anchors and vertically loaded anchors. Fluke anchors are applied when the load is mostly horizontal. Despite their benefits, drag anchors require a more complicated installation, where it might be challenging to achieve the desired position. The experience with drag anchors on permanent floating facilities is also limited. (Randolph & Gouvenec, 2011)

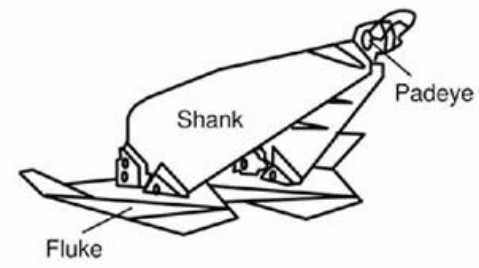

Figure 22 - Fluke anchor (Randolph & Gourvenec, 2011)

Figure 21 - Vertically loaded anchor (Randolph & Gourvenec, 2011)

2.4.7 Suction embedded plate anchors

The suction embedded plate anchor is similar to the suction anchor, although a plate is fitted at the bottom of the anchor. The anchor combines the benefits of a suction anchor and a plate anchor in the sense that installation is efficient, and the plate makes the system more economical. Although the anchor is more optimized than the suction anchor, the installation phase requires more time and there is limited experience with the anchor (Randolph & Gourvenec, 2011).

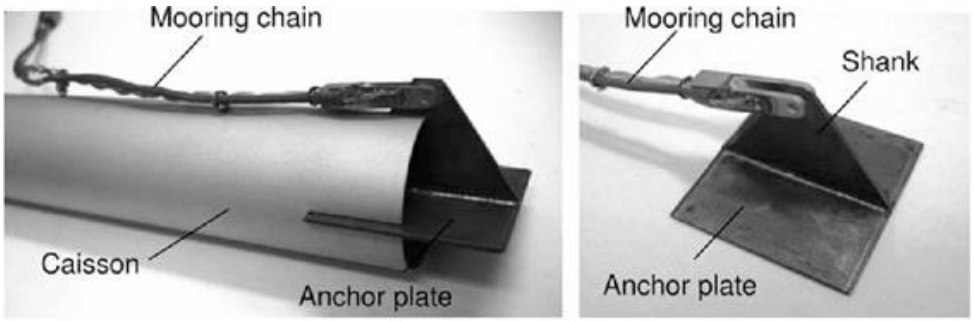

Figure 23 - Suction embedded plate anchor (Randolph & Gourvenec, 2011)

2.4.8 Dynamically penetrating anchors

The dynamically penetrating anchors have a missile-like shape and are well suited for penetration into the soil. The anchors are released about 20-50 meters above the seabed and will reach velocities in the range of 25-35 m/s. The advantages of these anchors are their simple production and installation. The primary disadvantage is the lack of experience. (Randolph & Gourvenec, 2011).

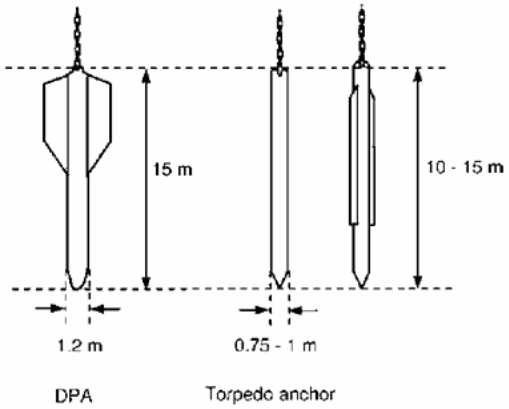

Figure 24 - Typical dynamically penetrating anchors (Randolph & Gourvenec, 2011)

3 Theory

This theory chapter will provide a framework for the topics discussed in the thesis. Firstly, the most relevant theory of soil mechanics will be outlined, before mentioning research on suction anchors. Thereafter, a review of the theory of elasto-plasticity will be given, before introducing the finite element method.

3.1 Selected theory of soil mechanics

Since the scope on this thesis is limited to the ultimate capacity and the stiffness relations, the theory part will focus on these topics.

3.1.1 Stresses

The stresses in the soil will in general be related to loading history and the strains in the soil. Unlike structural materials, the relation between stresses and strains will usually not be linear. It is still common to assume linear elasticity in settlement calculations and to model the elastic range of an elasto-plastic material as linearly-elastic. The elastic relations between the stresses and the strains are dependent of the Young's modules (Young, 1845) and the Poisson's ratio (Poisson, 1833). The constitutive relations are the following (Augustin, 1828):

$$\begin{Bmatrix} \sigma_x \\ \sigma_y \\ \sigma_z \\ \tau_{xy} \\ \tau_{yz} \\ \tau_{zx} \end{Bmatrix} = \frac{E}{(1+\upsilon)(1-2\upsilon)} \begin{bmatrix} (1-\upsilon) & \upsilon & \upsilon & 0 & 0 & 0 \\ \upsilon & (1-\upsilon) & \upsilon & 0 & 0 & 0 \\ \upsilon & \upsilon & (1-\upsilon) & 0 & 0 & 0 \\ 0 & 0 & 0 & (1-2\upsilon)/2 & 0 & 0 \\ 0 & 0 & 0 & 0 & (1-2\upsilon)/2 & 0 \\ 0 & 0 & 0 & 0 & 0 & (1-2\upsilon)/2 \end{bmatrix} \begin{Bmatrix} \varepsilon_x \\ \varepsilon_y \\ \varepsilon_z \\ \gamma_{xy} \\ \gamma_{yz} \\ \gamma_{zx} \end{Bmatrix} \quad (3.1)$$

where σ is normal stress
τ is shear stress
E is the Young's modulus
υ is the Poisson's ratio
ε is normal strains
γ is shear strains

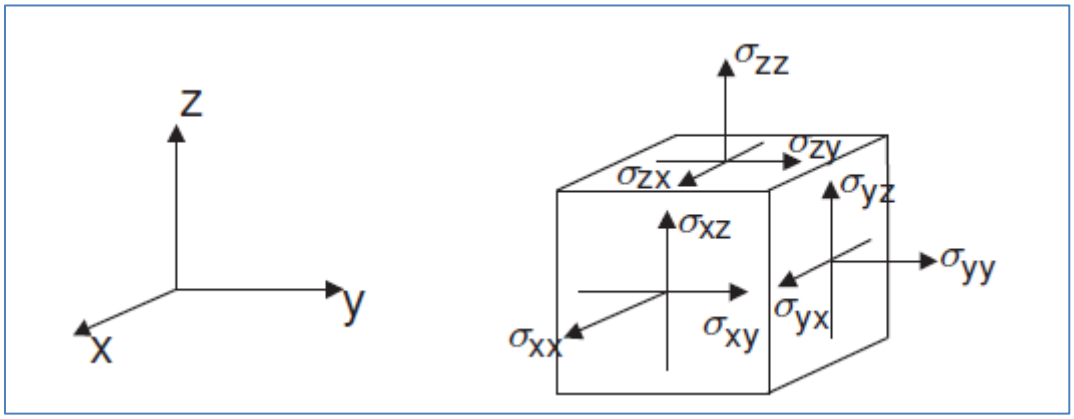

Figure 25 - Stresses in space (Plaxis, 2010)

The stresses can also be written in a matrix format (Augustin, 1828):

$$[\sigma] = \begin{bmatrix} \sigma_{xx} & \sigma_{xy} & \sigma_{xz} \\ \sigma_{yx} & \sigma_{yy} & \sigma_{yz} \\ \sigma_{zx} & \sigma_{zy} & \sigma_{zz} \end{bmatrix} \tag{3.2}$$

The Cartesian stress matrix can be transposed to the principal directions where the diagonal area of the matrix is non-zero. The three principal stresses are obtained by solving an eigenvalue problem consisting of the Cartesian stress matrix and a diagonal of the unknown principal stress, leading to (Irgens, 2008):

$$\sigma^3 - I * \sigma^2 + II * \sigma - III = 0 \tag{3.3}$$

where I, II and III are stress invariants, with the following form (Irgens, 2008) :

$$\begin{aligned} I &= \sigma_1 + \sigma_2 + \sigma_3 \\ II &= \sigma_1 * \sigma_2 + \sigma_2 * \sigma_3 + \sigma_3 * \sigma_1 \\ III &= \sigma_1 * \sigma_2 * \sigma_3 \end{aligned} \tag{3.4}$$

The maximum shear stress on a critical plane will be the difference between the largest and the smallest principal stress divided by two (Irgens, 2008):

$$\tau_c = (\sigma_1 - \sigma_3)/2 \tag{3.5}$$

3.1.2 The principle of effective stress

The stresses in the soil can be divided into two components; the effective stress state and the pore pressure (Terzaghi, 1943). The principle can be written with matrix notation:

$$\{\sigma'\} = \{\sigma\} - \{u\} \tag{3.6}$$

where:

$$\{\sigma\} = \begin{Bmatrix} \sigma_x \\ \sigma_y \\ \sigma_z \\ \tau_{xy} \\ \tau_{yz} \\ \tau_{zx} \end{Bmatrix}, \quad \{\sigma'\} = \begin{Bmatrix} \sigma'_x \\ \sigma'_y \\ \sigma'_z \\ \tau_{xy} \\ \tau_{yz} \\ \tau_{zx} \end{Bmatrix}, \quad \{u\} = u \begin{Bmatrix} 1 \\ 1 \\ 1 \\ 0 \\ 0 \\ 0 \end{Bmatrix} \tag{3.7}$$

The strength of the soil is governed by the effective stresses in both drained and undrained conditions. However, for undrained conditions the total stresses can also be applied.

3.1.3 Lateral earth pressure

The lateral earth pressure is the horizontal normal stress of soil on a vertical plane. Unlike hydrostatic pressure, the earth pressure will in general not be isotropic. While the vertical earth pressure is governed by the subjected loads, the lateral earth pressure will be dependent on loading history, vertical earth pressure and the friction angle and/or the Poisson's ratio. (Plaxis, 2010) Rankine (1857) introduced the earth pressure coefficient k, that is the limit ratio between horizontal/vertical and

vertical/horizontal earth pressures. When the horizontal stress is larger than the vertical stress, the soil is in a passive state, and when the vertical stress is larger, the soil is in an active state.

3.1.4 Failure criteria and drainage conditions

In order to estimate failure, a failure criterion is required. The Tresca and the Mohr-Coulomb criteria are commonly used as failure criteria in soil mechanics. Tresca is used in undrained conditions where the consolidation due to loading is insignificant, and can be used regarded to both effective and total stresses (Nordal, 2010):

$$\tau_c = (\sigma'_1 - \sigma'_3)/2 = (\sigma_1 - \sigma_3)/2 \tag{3.8}$$

Coulomb (1776) introduced a failure criterion in terms of the normal stress at critical plane and the friction angle. It was later modified to the Mohr-Coulomb criterion, that is commonly expressed (Nordal, 2010):

$$\tau_c = c + \sigma'_c * tan\phi \tag{3.9}$$

where τ_c is the critical shear stress
σ'_1, σ'_3, σ_1 and σ_3 are respectively principal effective and total stress components
c is the cohesion
ϕ is the friction angle

The main difference between Tresca and Mohr-Coulomb is that Tresca is pressure insensitive, while Mohr-Coulomb depends on the stress level. During effective stress analysis, the Tresca criterion will be governed by the Mohr-Coulomb criterion in undrained condition. The Tresca criterion is implemented in Plaxis with a Mohr-Coulomb material model, where the cohesion equals the undrained shear strength and the friction angle equals zero. (Plaxis, 2010)

3.1.5 Bearing capacity

Bearing capacity is the ultimate response that the system can resist. At failure, a kinematic mechanism is developed, consisting of plastic zones where the shear strength is fully mobilized. The bearing capacity in classical soil mechanics is characterized by stress zones. There are three different stress zones in total; the passive and active Rankine zones and the Plandtl zone. The Rankine zones are characterized by constant principal stresses and mobilization. The Plandtl zone is characterized by rotated principal directions and a constant mobilization factor. (Emdal et al. 2004) By combining the stress zones and imposing boundary conditions, the bearing capacity will be obtained.

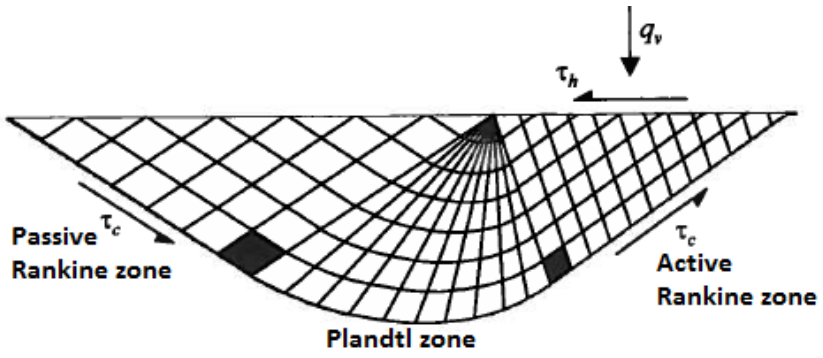

Figure 26 - Stress zones with Mohr-Coulomb (Emdal et al. 2004)

The stress zones and the bearing capacity are different for the Tresca criterion and the Mohr-Coulomb criterion. Since the scope of the thesis will be limited to undrained conditions, bearing capacity with Tresca will be the focus.

Exact solutions will rarely be found in soil mechanics. However, the exact solution for undrained conditions with constant shear strength in a plane strain condition with horizontal boundaries, is one of the exceptions (Emdal *et. al,* 2004):

$$\sigma_v = N_c \tau_c + p \tag{3.10}$$

where σ_v is the vertical stress acting on the loading surface
N_c is the bearing capacity factor for shallow plane strain problems, equal to $\pi+2$ for eccentric vertical loading
τ_c is the critical shear strength in the stress zones, equal to the shear strength at failure
p is the vertical stress acting on the surrounding surface

The capacity factor can also be solved exactly for inclined loading. The inclination degree is given by the roughness ratio r (Emdal *et. al*):

$$r = \frac{\tau_h}{\tau_c} \tag{3.11}$$

The non-dimensional factor; f_ω, can thus be obtained (Emdal *et. al,* 2004):

$$f_\omega = \frac{1}{r}(1 - \sqrt{1 - r^2}) \tag{3.12}$$

The rotation of the active principal direction on the active Rankine zone can then be calculated (Emdal *et. al,* 2004):

$$\tan(\omega) = f_\omega \tag{3.13}$$

Finally, the bearing capacity factor is observed (Emdal *et. al,* 2004):

$$N_c = (\pi - 2\omega) + \frac{2}{1 + {f_\omega}^2} \tag{3.14}$$

When the foundation is below ground level, the failure mechanism will involve a larger failure surface. The capacity will increase, and the depth correlation coefficient; f_D, is introduced. When the system is in three dimensions rather than plane conditions, the capacity will change, and the area correlation coefficient f_A is added. The capacity will then be (Emdal et al. 2004):

$$N_{c,DA} = (1 + f_D) * (1 + f_A) * N_c \tag{3.15}$$

The bearing capacity coefficient for rectangular deep foundations subjected to vertical loads without eccentricity, gives a value close to 9. The values of f_d and f_a are partly based on, which implies that the solution cannot be regarded as exact. (Emdal et al. 2004)

If there is an eccentricity between the resultant force from the subjected loads and the neutral axes, a moment will be present. Classical soil mechanics utilize the moment by reducing the dimensions of the foundation under the assumption that the soil has no tensile strength. However, most offshore

foundations in normally consolidated clay are likely to have a substantial tensile resistance due to short term loading, and the effective area approach would be conservative. (Randolph & Gourvenec, 2011)

3.2 Research on suction anchors

This section will introduce some important aspects of suction anchors. Suction anchors can roughly speaking be discussed from two perspectives; the installation phase, including the set-up characteristics, and the operational conditions, where capacity is the most important issue.

Andersen el al. (2005) presented a list of installed suction caissons with their corresponding properties. Since the first suction anchor was installed in 1981, about 500 suction caissons have been installed at 50 different locations, with the deepest installation being at 2,000 meters depth. Despite their widespread use, there is no report of failure during operation. In total, 19 experimental studies have been reported, addressing most aspects of suction anchors; the installation phase, pullout capacity, inclined loading, as well as cyclic loading with different strength profiles. Most of the studies are limited to undrained conditions.

3.2.1 Installation

The installation phase for a suction anchor involves two steps; firstly the anchor will penetrate by self-weight, then suction will bring the anchor further down, until the desired position is achieved. The penetration accounted for by self-weight is determined by the weight of the anchor, the shape of the anchor and the soil conditions. The suction in the second phase is achieved by pumping water out of the top of the anchor. This leads to a differential pore pressure between the exterior and the interior of the anchor, and will cause further penetration. The required suction is a key consideration at the installation stage. (Randolph & Gourvenec, 2011)

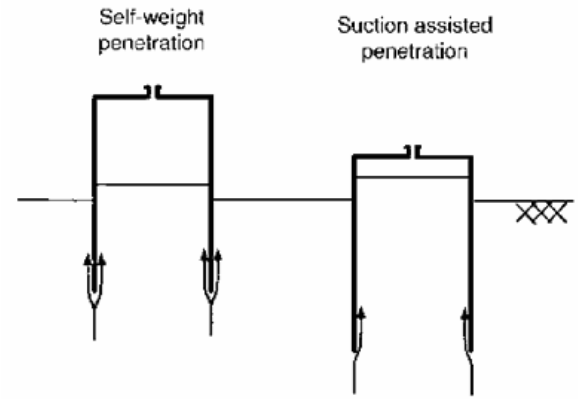

Figure 27 - Installation stages with suction anchor (Randolph & Gourvenec, 2011)

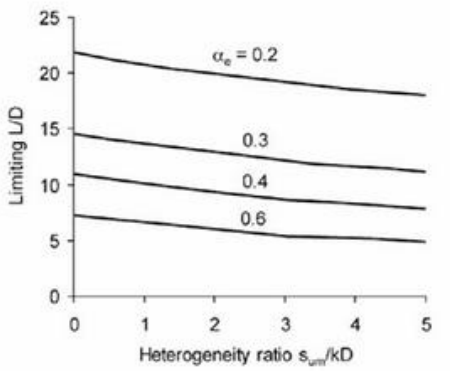

Figure 28 - Plug stability (Randolph & Gouvenec, 2011)

Buckling analysis is also of importance to study, since the anchor will be in compression. Another important consideration at the installation stage is the soil-plug stability that occurs when the resistance against internal soil-plug failure is less than the resistance against further penetration. In case of normally consolidated clay with a linearly increasing strength profile, figure 28 gives the critical length-to-width ratio, which will depend on the average shear strength, the width of the anchor, the internal wall roughness and the increasing coefficient of the strength profile. (Randolph & Gourvenec, 2011)

3.2.2 Operational conditions

After installation, the suction anchor has to resist the permanent and environmental forces from the mooring chain. Capacity will depend on anchor geometry, installation performance, soil conditions, load direction, time after installation, duration of applied loads, and cycles of loads. The stiffness of the system is also important, due to the dynamical response of the platform. It is also of interest to limit the deformations of the anchor due to position requirements. (Andersen *et. al*, 2005)

In general, suction anchors have a large horizontal capacity, and are thus commonly used in catenary mooring systems. The reasons why capacity is dependent on the time after installation, are thixotropic effects and consolidation. The effective stress state and the pore pressure will change over time. The shaft resistance will generally increase due to increased horizontal effective stresses. (Andersen & Jostad, 2002)

The operational considerations will in the following be dealt with in four sub-sections; vertical loading, horizontal loading, interaction between horizontal and vertical forces, as well as stiffness. Hand calculations of the torsional and the bending moment capacity can be performed by limit state equilibrium combined with the information given in the sections below. The results from hand calculations will be presented in the chapter on results.

3.2.2.1 Vertical loading

An important factor of the pull-out capacity of a suction anchor is the draining conditions. In case of undrained conditions, passive suction will be developed. The pull-out capacity will then be governed by the exterior skin friction, the reversed end bearing capacity and the weight of the anchor. Undrained conditions can be assumed when there is short term loading and the permeability of the soil is sufficiently low. This can usually be assumed for normally consolidated clay subjected to environmental loads. Drained conditions can be assumed when the anchor is subjected to permanent loads or when the soil has a high permeability, like sand. The pull-out capacity in drained conditions is determined by the interior and exterior shaft resistance, the weight of the anchor, minus the earth pressure acting on the skirt tip at base level. Partly drained conditions are conditions where neither drained, nor undrained, conditions can be assumed. The excess pore pressure has partly dissipated due to consolidation and there is a change in the effective stress state. The capacity is determined by the exterior shaft resistance, the weight of the anchor and a tension force at base level. (Thorel et al. 2005)

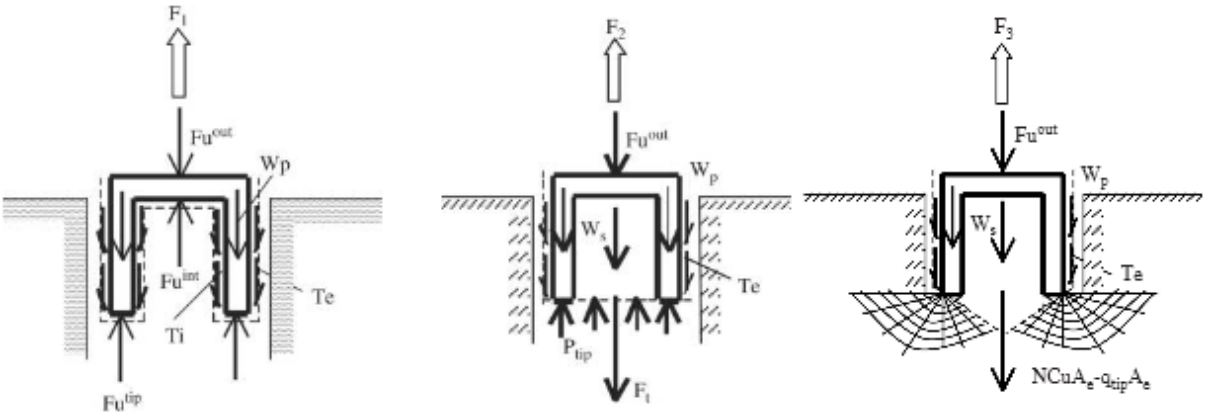

Figure 29 - Failure mechanisms: (a) drained, (b) partly drained, (c) undrained conditions (Thorel et al., 2005)

In order to estimate drainage type, Deng & Carter (2000) introduced a non-dimensional time coefficient T_k:

$$T_k = \frac{c_v}{v * B} \tag{3.16}$$

where c_v is the consolidation coefficient
v is the response velocity due to loading
B is the width of the anchor, representing the draining path

The non-dimensional time coefficient is then linked to the draining coefficient:

$$\begin{aligned} 0{,}6 < T_k &: \quad Drained\ conditions \\ 0{,}002 < T_k < 0{,}6 &: \quad Partially\ drained \\ T_k < 0{,}002 &: \quad Undrained\ conditions \end{aligned}$$

If no drainage takes place during loading, the end bearing capacity can be estimated:

$$V_{end} = N_c * s_u(z) * A \tag{3.17}$$

where V_{end} is the resistance constitution due to the reverse end bearing mechanism
N_c is the reverse end bearing factor
s_u is the shear strength
A is the area of the anchor base

The reverse end bearing factor is often taken as 9 (Randolph & Gourvenec, 2010). However, Jeanjean et al. (2006) noted values of N_c equal to 12 at large displacements.

An important contribution to capacity in all conditions is the shaft resistance. The shaft resistance can be calculated from effective stresses by Coulomb's law of friction or from total stresses, where the friction is taken as a portion of the shear strength (Andersen et al. 2005):

$$Drained: \quad \tau_s = \sigma_h' * \tan(\Phi_{interface}) \tag{3.18}$$
$$Undrained: \quad \tau_s = \alpha * s_u \tag{3.19}$$

where τ_s is the critical shear strength at the skirt at failure
σ_h' is the radial horizontal effective stress acting on the skirt
$\Phi_{interface}$ is the friction angle of the skirt
α is the reduction factor for skirt shear strength
s_u is the undrained shear strength of the soil

The total stress approach will be adopted in this project, with α accounting for the remolded soil during installation, the consolidation after installation and the skirt roughness.

There are several approaches for calculating the vertical pull-out capacity of the anchor (Lee et al. 2005). However, since the anchor has a length-to-depth ratio equal to 5, the vertical capacity can simply be calculated from the limit equilibrium in the same way as for piles. The drainage conditions

determine the mechanism, and also the force components of the equilibrium equation. For undrained conditions, capacity can be expressed as follows:

$$V_u = \pi LD\alpha\bar{s_u} + \frac{1}{4}\pi N_c LD^2 s_u(L) + W' \tag{3.20}$$

The average shear strength is used for the shaft resistance, while the shear strength at the base is chosen for the reverse end bearing capacity and W' denotes the effective weight of the anchor.

3.2.2.2 Horizontal loading

The horizontal capacities of suction anchors are mainly determined by anchor geometry and soil conditions. The horizontal capacity is also influenced by the accuracy of the installation with respect to torsion-induced rotations. There are two possible causes of induced rotations. Firstly, the padeye and internal ring stiffeners might be slightly inclined from the vertical, and cause an unbalanced torsional moment during penetration. The second possible cause relates to subsea current forces, which might result in a mooring chain out of position, and further impose an initial torsional angle on the suction anchor. Due to the misorientation, horizontal forces will also impose a torsional moment that will reduce capacity. A suction anchor is typically designed for a torsional angle of 7.5 degrees. (Lee *et al*., 2005)

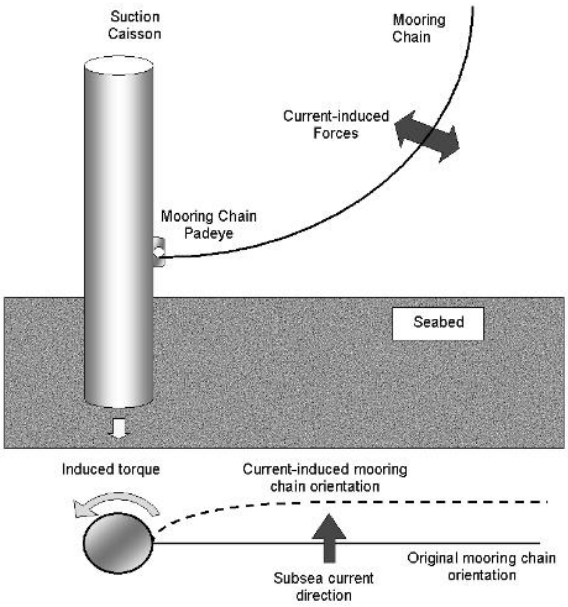

Figure 30 - Current-induced torsion (Lee et al., 2005)

The failure mechanism of horizontally loaded suction anchors is much like the failure mode of short horizontally loaded piles. The suction anchors can usually be considered as rigid (Randolph & Gourvenec, 2010), which means that the deformation pattern of the anchor can be described by six degrees of freedom; three translations and three rotations. This assumption simplifies the calculation of horizontal loading, because the soil-structure interaction can be disregarded. In the results, it will be shown how coarse this assumption is.

The failure capacity will also be influenced by the padeye position. If the load attachment point does not correspond with the optimum padeye position, the capacity will be reduced. Capacity can be further reduced by tension cracks on the active side. Jostad & Andersen (1999) propose a padeye position slightly below the optimum padeye position in order to reduce the effect of tension cracks. However, the tension crack envelope is generally not considered for normally consolidated clay subjected to short-term loads (Randolph & Gourvenec, 2011).

The failure mechanism will also change with the location of the point of attack. At the optimum position, the anchor will mainly translate without rotation, and the failure mechanism will consist of a conical wedge and a flow-around zone. If the load attachment point is above the optimum position, the center of rotation will be located within the anchor. The failure mechanism will then consist of a

conical wedge form and a rotational soil circle that rotates about the center of rotation, as seen in figure 31.

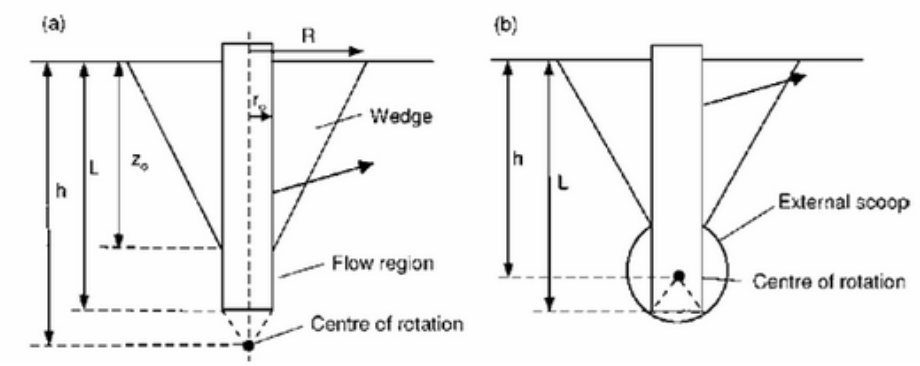

Figure 31 - Failure mechanisms for horizontally loaded suction anchors: (a) translational movement, (b) rotational movement, (Randolph & Gourvenec, 2011)

The reason why the translational failure mechanism has the flow-around region, is that resistance from the wedge mechanism increases with depth, which means that the flow-around mechanism will govern. As for laterally loaded piles, it might be convenient to examine resistance per unit length. The earth pressure acting on the anchor will then be treated as a strip load. Martin & Randolph (2006) give an analytical upper bound solution for the flow-around mechanism, where q varies between $9.14Ds_u(z)$ and $11.92Ds_u(z)$, depending on skirt roughness. The upper bound solution provides excellent results compared to the Randolph & Houlsby lower bound solution from 1984, see figure 32.

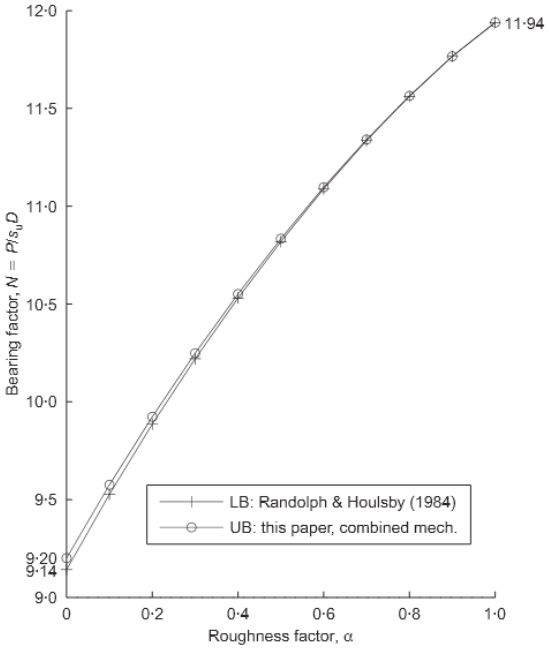

Figure 32 - Upper and lower bound solution flow-around mechanism (Martin & Randolph, 2006)

Randolph et al. (1998) presented a capacity diagram for suction anchors with different diameter ratios, load attachment points located at the optimum position and at the seabed, and with constant and linearly increasing shear strength, normalized by average shear strength, as well as the length and width of the anchor.

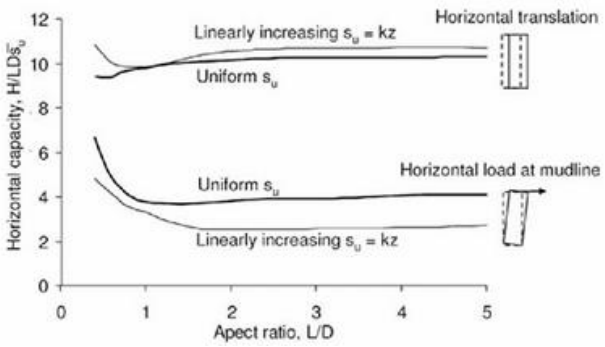

Figure 33 - Horizontal capacity (Randolph et al., 1998)

The capacity reduction due to the padeye position for suction anchors with different length-to-width ratios in normally consolidated clay was investigated by Supachawarote *et al*. (2004). The analysis was performed with a load inclination angle of 30 degrees, and showed that the largest capacity was obtained when the padeye depth was about 70 % of the total anchor length.

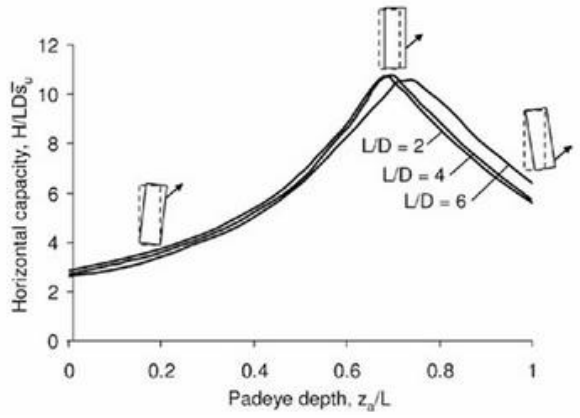

Figure 34 - Capacity with padeye positions (Supachawarote et al., 2004)

Aubeny & Murff (2005) presented a guideline for calculating the horizontal capacity of suction anchors:

$$\Delta H = P * D * \Delta z \quad (3.21)$$

$$P = N_{ps} * s_u(z) \quad (3.22)$$

$$H_u = \sum \Delta H \quad (3.23)$$

where ΔH is the lateral resistance of the length increment
D is the diameter of the cylinder
Δz is the depth of the length increment
N_{ps} is the lateral bearing capacity factor for the length increment
s_u is the shear strength of the length increment
H_u is the ultimate lateral capacity

N_{ps} is, due to the method, determined by formula 3.24-3.28 (Aubeny & Murff, 2005):

$$N_{ps} = N_1 - N_2 e^{-n(\frac{z}{1m})} \quad (3.24)$$

$$N_1 = 9.42 + 2.52 * r \quad (3.25)$$

$$N_2 = 7.42 + 1.7 * r \quad (3.26)$$

$$\rho = \frac{s_{u,0}}{s_{u,inc} * 1m} \quad (3.27)$$

$$n = 0.25 + 0.05 \quad (3.28)$$

where s_{u0} is the shear strength at the seabed

s_{uinc} is the incremental shear strength per unit depth

r is the roughness of the skirt

3.2.2.3 Inclined loading

The suction anchor will in general be subjected to inclined loading, which can be split into a horizontal and a vertical force component. Supachawarote *et al.* (2004) proposed the following interaction formula for suction anchors with different aspect ratios:

$$(\frac{H}{H_u})^a + (\frac{V}{V_u})^b = 1 \quad (2.29)$$

$$a = \frac{L}{D} + 0.5 \quad (2.30)$$

$$b = \frac{L}{3D} + 4.5 \quad (2.31)$$

The equation does not account for the bending moment that will be present due to eccentricity between the load attachment point and the neutral axes when the loads are applied at padeye.

Capacity diagrams in the horizontal and vertical loading space have been studied by several authors. El-Sherbiny *et al.* (2005) performed experimental small-scale analysis in normally consolidated clay, where the undrained strength profile was measured as $s_u(z) = 48 + 920 * z \ [Pa]$, with an anchor geometry of L*D=816mm*102mm. The results obtained are presented in figure 35.

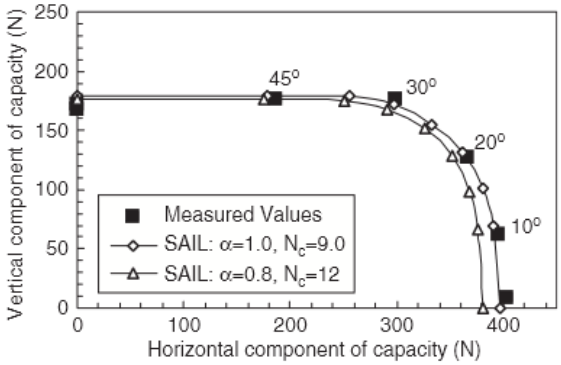

Figure 35 - HV-load space (El-Sherbiny et al. 2005)

The normalized horizontal capacity due to the average shear strength, the length and the width of the anchor gave a value equal to 11.6.

Capacity curves for combined loads, where the padeye position was also investigated, were prepared by Taiebat & Carter (2005), using the finite element method. Combinations of horizontal, vertical and torsional loads were interacted. The results were normalized due to shear strength, and the length and width of the anchor and had an aspect ratio of D/L=2.

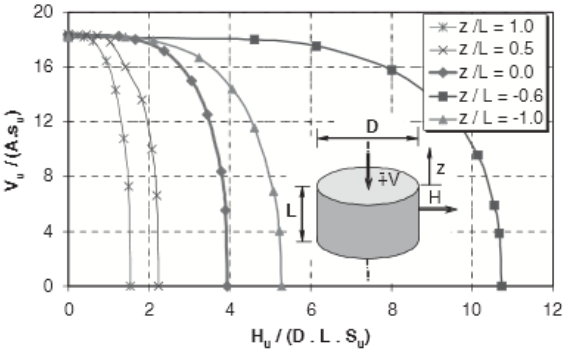

Figure 36 - HV-load space (Taiebat & Carter (2005)

The results were also normalized and presented in the horizontal, vertical and torsional load space.

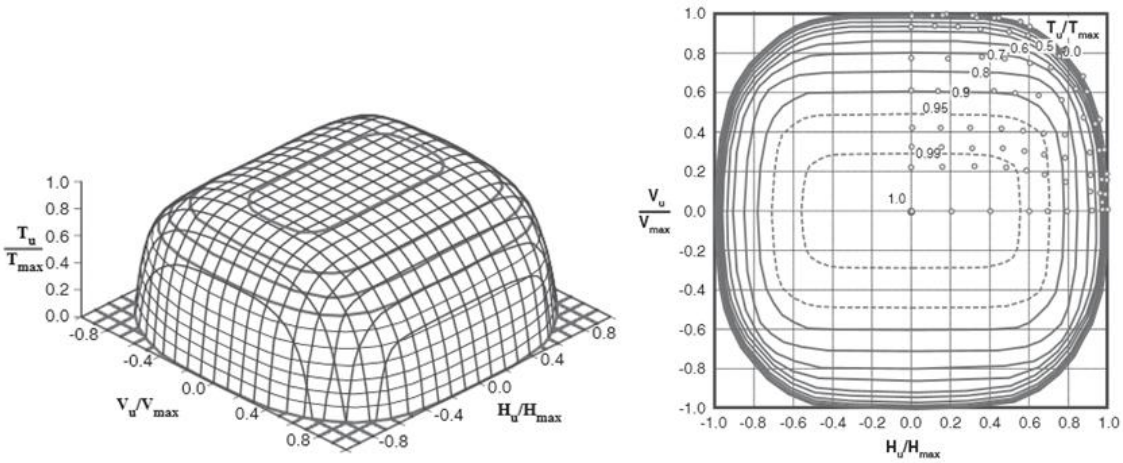

Figure 37 - Normalized HVT-space (Taiebat & Carter (2005)

3.2.2.4 Stiffness

The stiffness of the system will provide information of relevance to the elasto-plastic formulation and the reliability evaluation. Poulos & David (1974) gave the continuum elasticity solutions for geotechnical applications, like the laterally and vertically loaded pile. The vertical stiffness is obtained from figure 38. It is seen that the stiffness will be influenced by the ratio between pile length and model height through the influence factor Iρ.

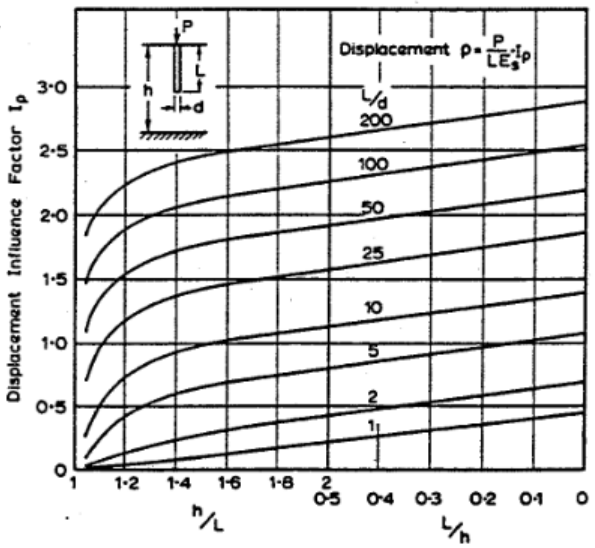

Figure 38 - Vertical loaded pile, Poisson's ratio of 0.5 (Poulos & David, 1974)

The stiffness of the laterally loaded pile is given in terms of displacements, and the horizontally applied load at a fixed pile head. The stiffness relation is the following:

$$\Delta = \frac{I_{pF}}{E_s L} H \tag{3.32}$$

where Δ is the lateral displacement at the pile head
I_{pF} is the influence factor, given in figure 39
E_s is the stiffness of the soil
L is the pile length
H is the horizontal load applied at the pile head

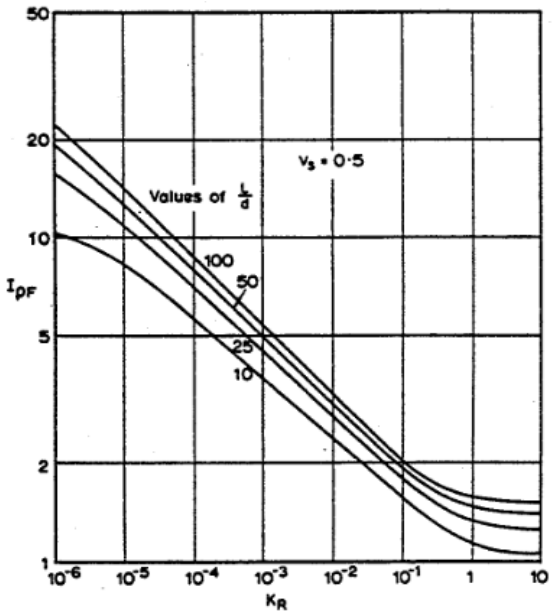

Figure 39 - Lateral fixed loaded pile (Poulos & David, 1974)

K_R in the diagram accounts for the soil-pile interaction. The diagram for laterally loaded piles is however, limited for aspect ratios of L/D in excess of 10.

The horizontal stiffness can be approximated as K_H=4LG for undrained conditions, where L is the pile length and G is the shear stiffness. This is under the assumption that the soil volume is sufficiently large. In order to calculate any solution close to being exact, the distance to fixed boundaries should be about 20 anchor diameters or more. (Randolph & Gourvenec, 2011)

3.3 Theory of elasto-plasticity

In the following section, the theory of elasto-plasticity will be presented. The theory of elasto-plasticity is in literature usually formulated in terms of stresses and strains, which will also be the focus of this section. The formulation can easily be adapted for forces and displacements, which will be done later in the exercise. The rate-insensitive elasto-plastic theory will be covered, under which the response is independent of time.

Elasto-plastic materials are characterized by permanent deformations in a loading-unloading sequence and energy dissipation when the loading is above the elastic limit. The strains are decomposed into elastic and plastic contributions. The elastic contribution will be governed by the elasticity matrix. This can be expressed as follows, with matrix notation (Cook *et. al*, 2001):

$$\{d\varepsilon\} = \{d\varepsilon_{el}\} + \{d\varepsilon_{pl}\} = [E]^{-1}\{d\sigma\} + \{d\varepsilon_{pl}\} \tag{3.33}$$

where $\{d\varepsilon\}$ is the incremental strain vector
$\{d\varepsilon_{el}\}$ is the incremental elastic strain vector

$\{d\varepsilon_{pl}\}$ is the incremental plastic strain vector
$[E]$ is the elasticity matrix
$\{d\sigma\}$ is the incremental stress vector
$[E_t]$ is the tangential constitutive matrix

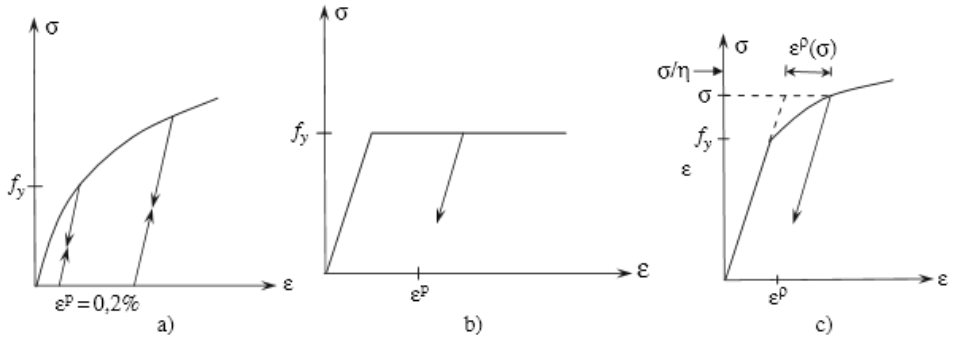

Figure 40 - Elasto-plastic response: (a) material without initial yielding plateau, (b) elastic-perfectly plastic response, (c) hardening material (Irgens, 2008)

Elasto-plasticity consists of three necessary components:

- Yield criterion
- Flow rule
- Hardening rule

The yield criterion defines the yielding of the material, the flow rule links the plastic strains to a potential surface, while the hardening rule relates the plastic strain increment with expansion of the yield surface. (Irgens, 2008)

3.3.1 Yield criterion

The yield criterion is a function that defines yielding in the material and consists of the stress components and state parameters. The yield function is less than zero prior to yielding and equals zero during yielding, and cannot have values above zero. (Cook *et. al*, 2001)

$$F < 0: \ Elastic\ responce$$
$$F = 0: \ Yielding$$
$$F > 0: Not\ possible$$

The yield function will form a yield surface in space. In the case of six stress components, the failure surface will have a rank of six dimensions. The failure criterion will be governed by the yield criterion and the corresponding state parameters. The mobilization degree is often a state parameter for soil mechanics and is the state parameter for isotropic hardening in this exercise. The chosen yield criteria will depend on the physical properties of the material. The following criteria are commonly used (Irgens, 2008):

$$von\ Mises: \ F(\boldsymbol{\sigma}, \boldsymbol{\kappa}) = \sqrt{3J_2} - f_y \quad (3.34)$$
$$Tresca: F(\boldsymbol{\sigma}, \boldsymbol{\kappa}) = (\sigma_1 - \sigma_3) - f_y \quad (3.35)$$

where $F(\boldsymbol{\sigma}, \boldsymbol{\kappa})$ is the yield function, depending on the stresses and the state parameters
J_2 is the negative second principal invariant $(= -II')$
f_y is the yield stress, which will increase with hardening/softening

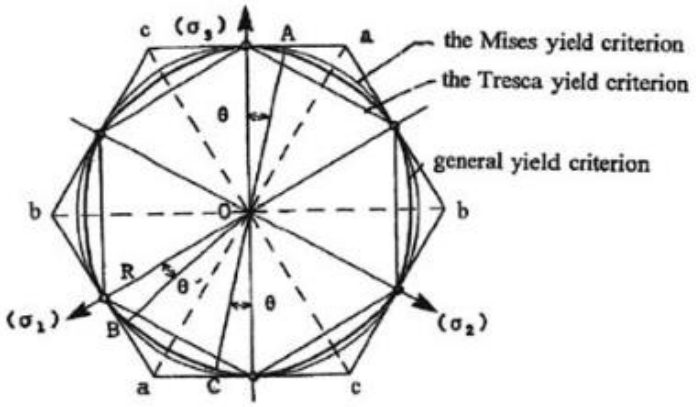

Figure 41 - Yield criteria in ∏-plane; von Mises, general yield criterion and Tresca (Irgens, 2008)

3.3.2 Flow rule

The flow rule relates to the plastic strains and stresses. The relationship can be formulated in the following way, in index form (Irgens, 2008):

$$dE_{ij}^{pl} = d\lambda \frac{\partial g}{\partial T_{ij}} \tag{3.36}$$

where dE_{ij}^{pl} is the incremental strain tensor
$d\lambda$ is a plastic multiplier
g is the potential function
T is the stress tensor

In the case of associated flow, the gradient of the potential function will equal the gradient of the yield criterion; g=f. In soil mechanics, the principle of associated flow will mean that the dilatational angle equals the friction angle.

3.3.3 Hardening rule

The hardening rule describes how the stiffness properties of the material change when the material approaches failure. The hardening of a material is measured by laboratory tests; the empirical curve fitting formulas will be constructed in order to implement the hardening properties in the model. (Nordal, 2010)

An isotropic hardening rule is often assumed, under which the yield surface will expand isotropically. However, it turns out that isotropic hardening often does not correspond to real material behavior, due to the Bauschinger effect. Kinematic hardening can then be implemented, where the yield surface translates rather than expands. It is also possible to combine the two approaches. (Irgens, 2008)

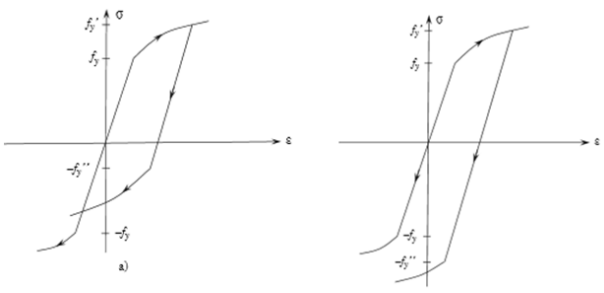

Figure 42 - Kinematic and isotropic hardening (Irgens, 2008)

3.4 The finite element method

The finite element method is a numerical calculation method that has changed the daily life of structural engineers due to its benefits. A continuum is discretized into a finite number of elements, with the kinematics being ensured by the nodes. The method can be applied to literally all fields of engineering. The method is most commonly used for (Zienkiewicz *et. al*, 2005):

- Static problems
- Dynamic problems
- Flow
- Electrical engineering
- Heat transfer

The calculations can be performed linearly or nonlinearly, and different fields can be combined in coupled analyses. The method as applied to soil mechanics has some of the following characteristics:

- The analysis is usually performed incrementally due to material non-linearity
- The calculation usually consists of several calculation stages
- The stresses are divided into effective stresses and pore pressure
- Soil parameters are included, such as frictional angle and cohesion

In the following, the method as applied to static problems is summarized, cf. Cook *et al.* (2001). The deformation in an element is discretized in the following way:

$$\{u(x,y,z)\} = [N(x,y,z)]\{d\} \tag{3.37}$$

where $\{u\}$ is the deformation vector for an element
$[N]$ is the interpolation function matrix
$\{d\}$ is the deformation at the nodes

The stiffness matrix for an element is constructed in the following way:

$$[k] = \int_V [B]^T [E][B] dV \tag{3.38}$$

where $[B]$ is the strain-displacement matrix, $[B] = [\partial][N]$
$[E]$ is the elasticity matric
$[k]$ is the element stiffness matrix

After assembling the element equations to global size and imposing boundary conditions, the global equilibrium equation is constructed:

$$\{R\} = [K]\{D\} \tag{3.39}$$

where $\{R\}$ is the load vector
$[K]$ is the global stiffness matrix
$\{D\}$ is the global displacement vector

The stresses in an element are obtained by the following relation:

$$\{\sigma\} = [E]\{\varepsilon\} = [E][B]\{d\} \quad (3.40)$$

The formulation constrains the system to deform according to the interpolation functions, which means that the deformation pattern of the system is restricted. The method gives an upper-bound solution, but usually converges towards an exact solution when the number of elements increases. Element types and the number of elements are, for that reason, important for purposes of any finite element application. (Zienkiewicz *et. al*, 2005)

In the case of nonlinearities, the global stiffness equation is solved incrementally. There are four main types of nonlinearities (Zienkiewicz & Taylor, 2005):

- Material nonlinearities due to non-linear relationship between stresses and strains
- Nonlinearity between displacements and strains due to large displacements
- Geometric nonlinearities in terms of displacement boundary conditions
- Geometric nonlinearities in terms of load boundary conditions

All types of nonlinearities might be relevant for soil mechanics problems. The relationship between stresses and strains is usually non-linear for soils that should be included. In soft soil, the large deformations might be developed that give rise to a nonlinear relationship between displacement and strains. Geometric nonlinearities might become prominent when contact surfaces change during loading. Examples include post-failure of a slope or vertical pull-out of a suction anchor; in both cases the geometry will change to a large degree.

4 Soil modeling

This chapter will cover the modeling process. Firstly, general modeling considerations will be emphasized, before discussing the soil parameters for the project. Thereafter, other parameters and properties of the system will be presented. Plaxis 3D will be briefly presented, before addressing the soil volume and the failure definition for the thesis. At the end of the chapter, results from mesh refinement will be given.

4.1 Modeling considerations

In order to solve the system, simplifications are needed. Firstly, the system is discretized by finite elements. Thereafter, it is necessary to specify how the equations will be solved. It is important for the model to maintain its physical properties and for the model to be efficient. Some of the important modeling considerations for this project are as follows:

- Material properties
- Soil volume
- Element properties
- Geometrical nonlinearities
- Simplifications of the geometry
- Number of elements
- Solution methods
- Failure definition

These aspects will be covered in the following paragraphs.

4.2 Soil parameters

The soil parameters determine the physical properties of the soil at the site. The results from a numerical study will be governed by the input parameters. For that reason, it is important to assign appropriate values to the different parameters, and to understand how these will influence the results. The soil properties need to be realistic for the given site and for the given loading. However, simplifications are always necessary in order to limit the complexity. The soil conditions implied are normally consolidated soft clay, typical of the deep water facilities in the Gulf of Mexico (Jeanjean, 2006).

4.2.1 Strength parameters

The study is limited to undrained conditions, which means that the pore pressure will not consolidate in any significant way. The strength will thus be governed by the Tresca criterion, which is accomplished by using a Mohr-Coulomb material model with a friction angle equal to zero and a cohesion equal to the shear strength. Due to the normally consolidated clay, the shear strength will increase with depth, and will be almost proportional to depth. The shear strength profile is formula 4.1 is used throughout the thesis:

$$s_u(z) = 2 + 1 * z \quad [kPa] \tag{4.1}$$

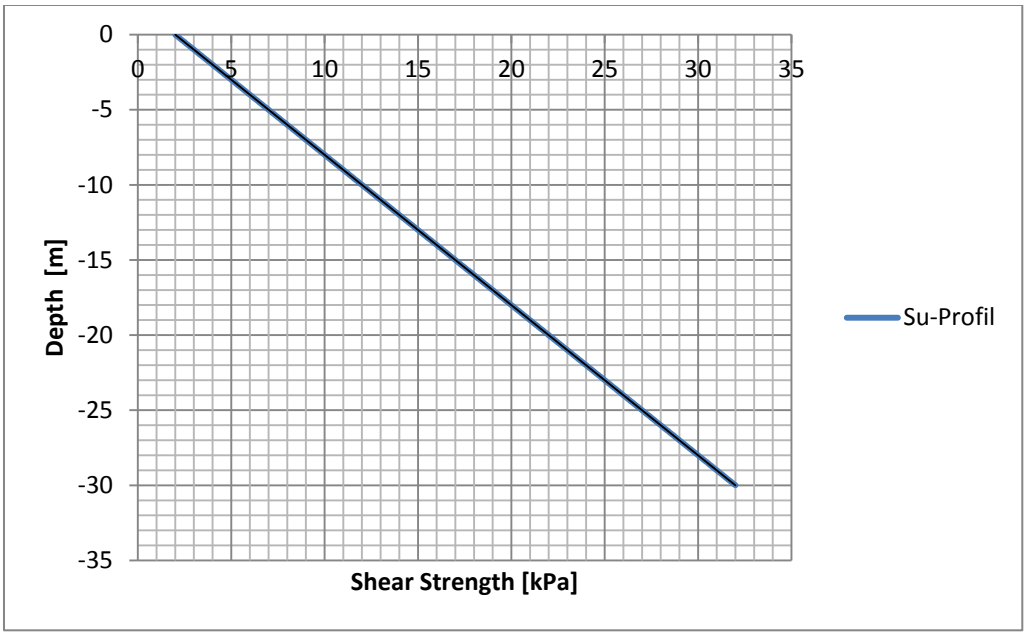

Figure 43 - Shear strength profile

The sensitivity of the soil is taken as S_t=3. This means that the remolded shear strength is a third of the original shear strength. The soil close to the structural elements is assumed to be remolded during installation. However, the strength at the interfaces will be regained over time. This is due to dissipation of excess pore pressure, an increase in horizontal stresses and thixotropy (Jostad & Andersen, 2002). A period of time will elapse between the anchor installation and the application of the mooring force, which is assumed to be in the range of 60-100 days. Jostad & Andersen (2002) give a relation between set-up time, the plasticity index and the thixotropy factor. A low plasticity index is assumed. The thixotropy factor is then taken as C_t=1.32, see figure 44. The external skin friction can then be modeled as $\alpha=C_t/S_t=1.32/3=0.44$. The interface shear strength is then taken as $s_{u,interface}(z)=0.44*s_u(z)$.

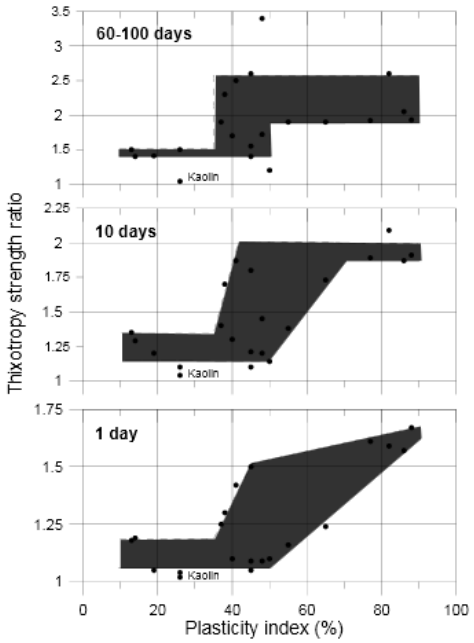

Figure 44 - Thixotropy strength ratio (Jostad & Andersen, 2002)

The soil is modeled with a dilatational angle equal to zero. This assumption leads to associated flow for this given project, since the friction angle also is zero. This means that plastic strain increments will be normal to the yield surface; the plastic strains will be associated with the yield surface. A dilatational angle equal to zero is appropriate when the initial soil is neither dense, nor loose. It is believed that associated flow on an element level will also impose associated flow between plastic deflections and the corresponding yield surface in terms of padeye location. This means that when the elements are integrated into a global scale, the associated flow remains valid.

The tension strength is modeled without cut-off, which means that the failure will only be governed by the shear strength. This choice is made to allow for suction during pull-out; the tip resistance during pull-out will then be due to reversed end-bearing capacity. This assumption implies that the soil has a low permeability, which is typical of soft clay, and that the loading rate is sufficiently large. According to equation 3.17 and the corresponding conditions, a reversed and bearing mechanism will be valid if $T_k < 0.002$.

If the consolidation coefficient is taken as 2 m^2/year, which is appropriate for soft clay, and the static response is taken as 0.1 meter, which equals a pull-out force of 8,000 kN (obtained from the results), the critical load duration will be about 5 hours. If the load acts for more than 5 hours, the situation will be partly drained, and a tension criterion might be imposed. It is important to remember that the system is limited to short term loads, since the vertical capacity will decrease over time. It should also be noted that when there is no tension cut-off, the effect of tension cracks on the active side during horizontal loading will be ignored.

4.2.2 Stiffness parameters

The stiffness of the soil will usually be related to the strength of the soil. Due to the normally consolidated clay, the relationship between strength and stiffness is assumed to be proportional. Due to the undrained condition, the bulk modulus will in theory be infinity. However, in order to avoid singularity in the stiffness matrix, a finite value of the bulk modulus is used. The stiffness parameters are taken to be the following:

$$G(z) = 100 * s_u(z) \quad (4.2)$$

$$K(z) = 100 * G(z) \quad (4.3)$$

The stiffness parameters are implemented implicitly through the Young's modulus and the Poisson's ratio:

$$G = \frac{E}{2(1+\upsilon)} \quad (4.4)$$

$$K = \frac{E}{3(1-2\upsilon)} \quad (4.5)$$

By combining formula 4.2-45, following input parameters for E and υ will then obtained:

$$E(z) = 300 * s_u(z) \quad (4.6)$$

$$\upsilon = 0.495 \quad (4.7)$$

A perfectly elasto-plastic Mohr-Coulomb material model is chosen, which means that when the critical shear stress at a soil element is below the maximum allowable shear stress, the response remains linearly elastic, while if the critical shear strength equals the shear strength, the tangential

stiffness of the soil element due to loading will be zero. In reality, the shear stiffness is likely to gradually decrease with the mobilization factor, f. The chosen stiffness can be regarded as a mean stiffness for the total elastic range.

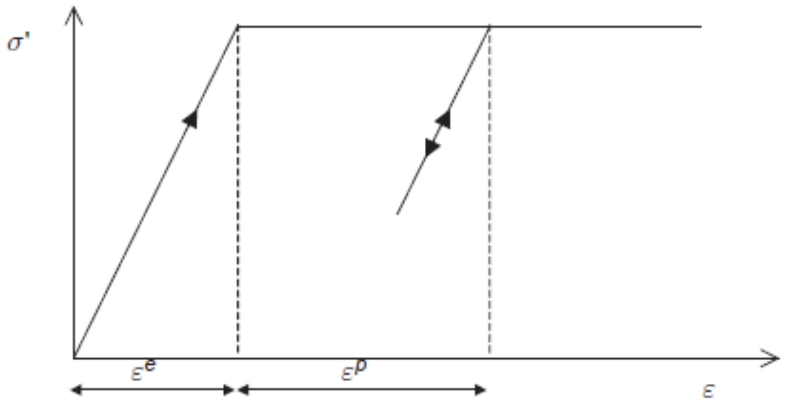

Figure 45 - Linearly elastic-perfectly plastic material model (Plaxis, 2010)

4.2.3 Initial conditions

In reality, the ground water head starts hundreds of meters above the seabed, due to the site being at deep water. However, the ground water head in the model starts at the seabed, since it will not have any impact on the response in this case due to the input parameters, and it is slightly more practical. The density of the soil is taken as 15 kN/m^3, which means that the effective vertical stress increases by 5kPa per meter. The initial horizontal stresses are calculated as:

$$\sigma'_{h0} = K_0 * \sigma'_{v0} \tag{4.8}$$

where σ'_{h0} is the initially horizontal effective stresses
σ'_{v0} is the initially vertical effective stresses
K_0 is the coefficient of earth pressure at rest

The coefficient of earth pressure at rest is taken as 1. The theory of elasticity and Jacy's empirical formula would provide the same answer (υ=0.5, ϕ=0). This means that the initial horizontal stresses equal the initial vertical stresses, which imposes an initial state without shear stresses (equation 3.5).

4.3 Properties of the system

The properties of the system, apart from the soil parameters, include the anchor geometries, the material properties of the anchor and how the mooring force is applied to the system. It also includes constraint properties that will be used later in the project. Other properties of the model will be covered later in the chapter.

The anchor geometry is governed by the capacity requirements. The supporting earth pressure causes structural forces that the anchor has to be designed for. This is accomplished by the desired thickness of the plates. The forces from the mooring chain are applied to the anchor through a connection called padeye. Due to the concentrated mooring force, there are additional supporting plates in the padeye area. In addition, the anchor consists of ring stiffeners, due to stability issues arising during the installation, and a sealed cap in order to allow for suction. The anchor is modeled without the stiffeners, and the sealed cap is modeled as a circular plate at the seabed. Neither simplification will change the response in a significant way for the given purpose.

The suction anchor has a total length of 30 meters and a diameter of 6 meters. The padeye is a triangular plate located 17.5 to 20.5 meters below the seabed, and is 1 meter wide. The additional reinforcing plates are located in the same 3 meter-range as the padeye, see figure 46.

The plates consist of four different thicknesses in total; 32, 40, 70 and 300 mm. The thickness of the cylinder is 32 mm, but is amplified by 70 mm close to the padeye. The padeye plate has a thickness of 300 mm, while the additional plates close to the padeye are 40 mm. The sealed cap is also 40 mm.

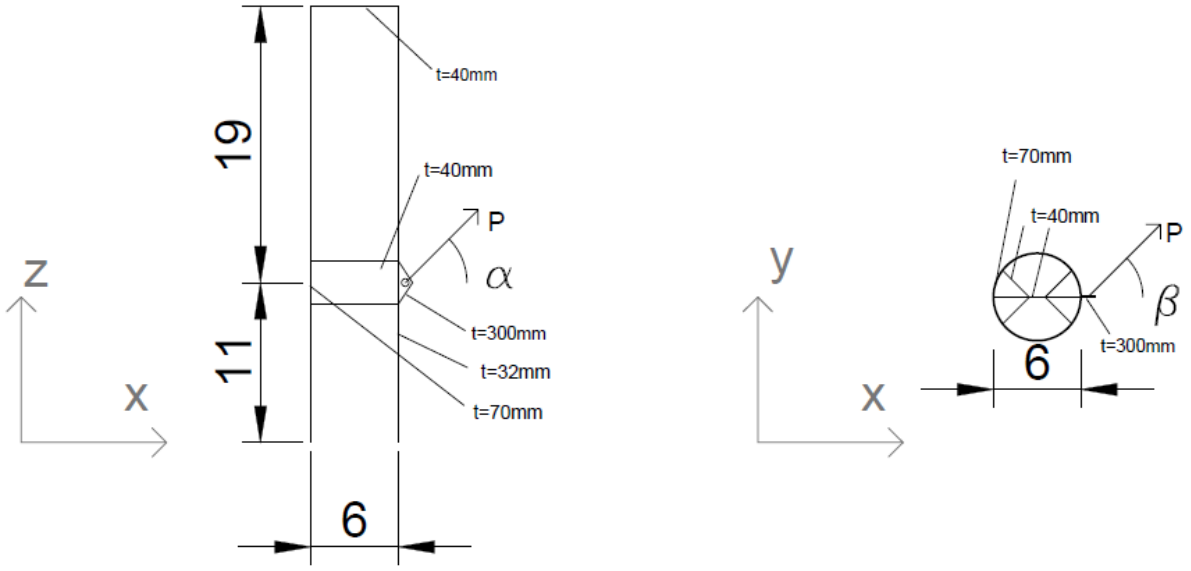

Figure 46 - Geometry suction anchor. Dimensions in meters when not specified

The forces are applied to the system through the padeye as a load vector, consisting of force components in the x-, y- and z-direction. The load attachment point is located 19 meters below the seabed level, and has an eccentricity of 3.75 meters from the neutral axis, or simply 0.75 meter from the anchor wall. The loads applied to the system are then applied in a realistic way, which will result in 6 load components; 2 horizontal loads, 1 vertical load, 2 bending moments and a torsional moment. The force components will be constrained, due to the fact that the loads applied to the system consist of 3 unconstrained forces at the load attachment point. The relation between the forces can be expressed in the following way:

$$H_x = P * \cos(\alpha) * \cos(\beta) \quad (4.8)$$
$$H_y = P * \cos(\alpha) * \sin(\beta) \quad (4.9)$$
$$V = P * \sin(\alpha) \quad (4.10)$$
$$M_x = H_y * e_z = P * e_z * \cos(\alpha) * \sin(\beta) \quad (4.11)$$
$$M_y = H_x * e_z - V * e_x = P * (e_z * \cos(\alpha) * \cos(\beta) - e_x * \sin(\alpha)) \quad (4.12)$$
$$T = M_z = H_y * e_x = P * e_x * \cos(\alpha) * \sin(\beta) \quad (4.13)$$

where
P is the magnitude of the force padeye force
H_x is the horizontal force in the x-direction
H_y is the horizontal force in the y-direction
V is the vertical force
M_x is the bending moment about the x-axis
M_y is the bending moment about the y-axis
T is the torsional moment

α is the inclination angle, the angle between horizontal plane and the load vector
β is the torsional angle, the angle between the padeye plane and the mooring chain
e_x is the eccentricity in the x-direction, 3.75 m
e_z is the eccentricity in the z-direction

The magnitude of the total horizontal force has the following expression:

$$H = \sqrt{{H_x}^2 + {H_y}^2} = P * \cos(\alpha)\sqrt{cos^2(\beta) + sin^2(\beta)} = P * \cos(\alpha) \quad (4.14)$$

Pythagorean equation can also be applied with respect to the bending moments:

$$M = \sqrt{M_x^2 + M_y^2} \quad (4.15)$$

The relationship between the mooring force and the translational forces are illustrated by figure 47.

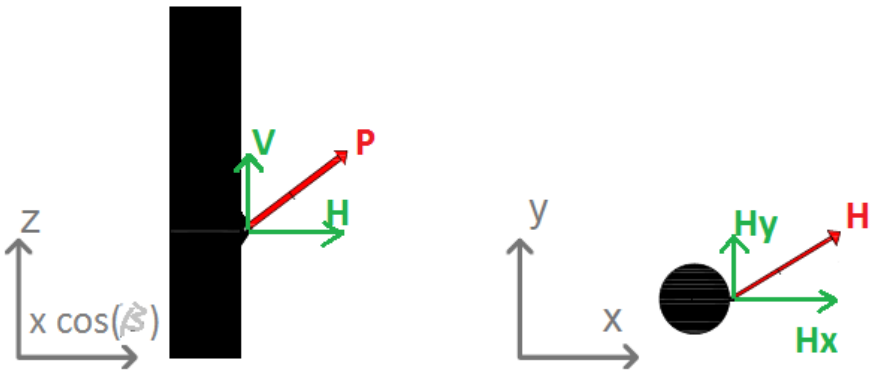

Figure 47 - Relation between the translational forces

The constraint equations and the eccentricity e_z require some discussion. The translational forces are simply decomposed due to the load inclination angle and the torsional angle. The torsional moment equals the horizontal distance from the neutral axis to the load attachment point, multiplied by the force component in the y-direction. The definition of the bending moments is however less obvious, and relates to the eccentricity e_z, which is the vertical distance between the load attachment point and the neutral plane. The neutral plane is the plane where horizontal loads do not causes bending moments. e_z can be regarded as an elastic property, a plastic property, or be disregarded. Following definitions yields; the plastic plane is the plane that gives the largest horizontal capacity and the elastic plane is the plane that gives no rotation of the anchor, see figure 48. The argument for excluding e_z is that the eccentricity is not a known property. It will be shown in section 5.7 that the plastic eccentricity is important in order to construct a realistic empirical yield surface. The elastic eccentricity is not explicitly needed for this given anchor, but it will be showed in section 7.3 that it will be useful to describe the stiffness of arbitrary suction anchors. The suction anchor needs to be considered as rigid in the area around the padeye, in order for the constraint equations to be valid. It will be shown by analysis that this assumption is appropriate.

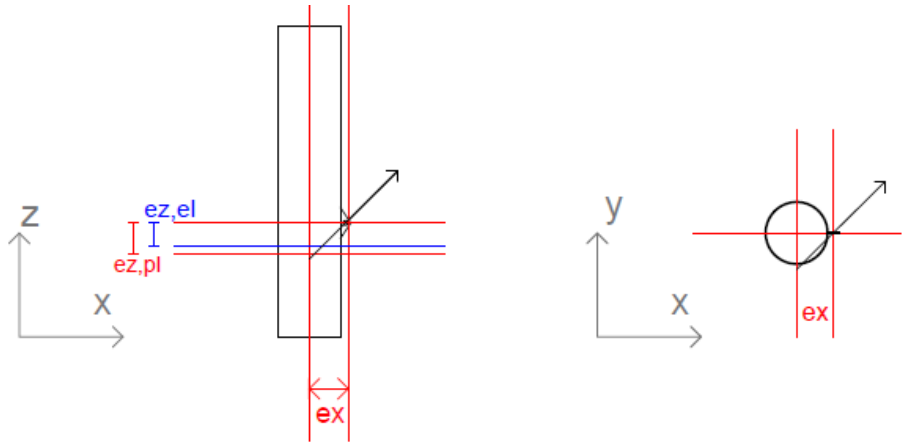

Figure 48 – Elastic and plastic planes and eccentricities

Note that the difference between the elastic and plastic eccentricities will only be an issue in z-direction, and that where are no eccentricities in y-direction.

4.4 Plaxis 3D

Plaxis is a finite element software applied to geotechnical problems, which was developed at TU Delft in the Netherlands back in the 1980s. Plaxis was launched as commercial software in 1993, and the code for three-dimensional problems became available a few years after the turn of the millennium. The modeling in Plaxis 3D is similar to the modeling in Plaxis 2D, although the 3D modeling is in space. The modeling is efficiently performed by commands. Unlike Plaxis 2D, it is not possible to select between different elements. (Plaxis, unknown) The element types will now be presented.

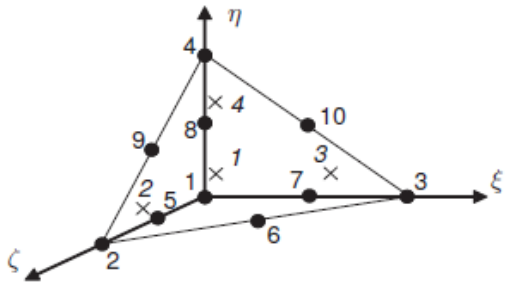

Figure 49 - Soil elements with Plaxis 3D (Plaxis, 2010)

Plaxis 3D uses a 10-node tetrahedron for the soil elements. Each node in the soil elements consists of 3 degrees of freedom (DOFs). The elements are numerically integrated from the 4 Gauss points. (Plaxis, 2010)

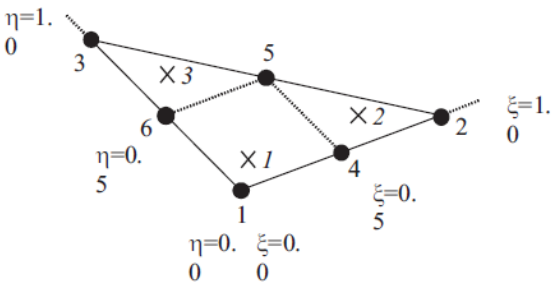

Figure 50 - Area elements with Plaxis 3D (Plaxis, 2010)

Plaxis 3D uses a 6-node triangular element for the plate elements. Each node in the plate element consists of 6 DOFs, which includes 3 translations and 3 rotations. The plate elements will then be capable of calculating moments, as well as shear forces and normal forces. The plate elements are numerically integrated from the 3 Gauss points. (Plaxis, 2010)

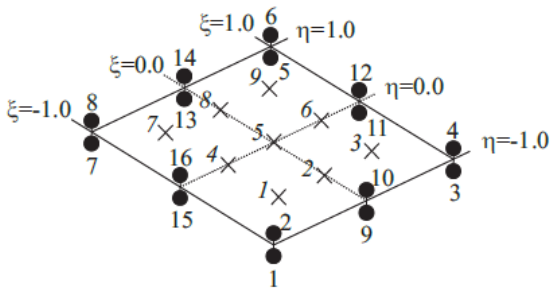

Figure 51 - Illustration of interface elements with Plaxis 3D (Plaxis, 2010)

Plaxis 3D uses a 12-node triangular element for the interface elements. The element consists of 6 coupled nodes that are located in the same place, which makes differential displacements between the soil element and the structural element possible. The interface elements are also integrated numerically from 3 Gauss points. (Plaxis, 2010) Note that figure 51 indicates that the interface elements are not triangular, which means that is can only be considered as an illustration.

The three different types of element all have 3 nodes at each edge, and are thus comparable. Also note that the different elements have an isoperimetric formulation. The elements in Plaxis 3D have a lower order than in Plaxis 2D, meaning that substantially more elements are needed to obtain the same degree of accuracy (Cook *et. al*, 2001).

The boundary conditions for soil volumes in Plaxis 3D is, by default, the following: Boundaries whose surface is normally in the x-direction will be fixed in the x-direction and free in the y- and z-directions; boundaries whose surface is normally in the y-direction will be fixed in the y-direction and free in the x- and z-directions; the bottom is fixed in all directions; while the ground surface is free in all directions. (Plaxis, 2010)

After all the elements are assembled, the equilibrium equations need to be solved. Due to material nonlinearity, the equations need to be solved in an incremental fashion. Plaxis 3D solves the system equations in the same way as Plaxis 2D. The default settings will in most cases be appropriate, and are also used for this project. (Plaxis, 2010)

Geometrical nonlinearity and large deformation theory can be introduced by the updated mesh option. After each load increment, a new mesh of the model will be generated from the deformed mesh. Additional terms will also be present in the stiffness matrix, and a co-rotational rate of Kirchhoff stress is adopted. Updated mesh is much more time-consuming than the standard analysis, and should only be considered when the geometrical non-linear effects are significant. The geometrical nonlinearities are disregarded for purposes of the analysis, which means that the initial configuration will be the reference configuration throughout the calculations. (Plaxis, 2010)

4.5 Soil volume

The soil volume size applied in the model is an important factor in the modeling. If the chosen soil volume is too small, it will reduce the kinematic freedom of the system. This will limit the deformations and might also change the failure mechanisms. However, if an excessive soil volume is chosen, the analysis will be more time consuming. How the failure mechanisms will be developed can roughly be predicted prior to the analysis. For instance, if average undrained strength, plane conditions and smooth wall are assumed, the slip-plane would have an inclination angle of 45 degrees. The failure mechanisms for suction anchors were presented in section 3.2, and will give insight into the necessary soil volume in the model due to failure.

In the preliminary modeling stage, several soil volumes were tested; initially a soil volume with dimensions of Depth*Width*Height=120 m*120 m*60 m was tested, and then reduced. A reduction of the initial volume with the same number of elements gave more accurate results in terms of capacity, which indicated that the benefits from denser elements outweighed those from smaller distances to the boundaries. The geometry finally chosen had the dimensions 80 m*80 m*50 m, which still have a sufficient kinematic freedom of the system with respect to the mechanisms that will be developed.

4.6 Failure definition

The failure definition is also an important factor of the modeling. In theory, the failure state is characterized by an additional infinitesimal load increment which results in infinite deformation; the system is then said to be singular. However, a singular response in Plaxis 3D does not occur at physically realistic displacements. Also, when the system displaces hundreds of meters, the analysis becomes time-consuming and is not efficient. An adoptive failure criterion is thus desired.

The alternative failure criterion can for instance be governed by a deformation criterion. It is important that the capacity of the criterion is close to the largest possible load. It is also important that a well-defined plastic zone is developed, where the plastic response dominates the overall response. The load cases in the project are calculated to about 10 meters padeye deflection. From the load-deflection curves, it was observed that the plastic response started at about 0.1 meter, and that the yield plateau was well-defined after 1 meter, slightly depending on the load case. The definition throughout the thesis is one meter absolute padeye deflection. It should be noted that the displacement due to installation of the anchor is reset to zero, in order to isolate the response caused by the load cases.

4.7 Mesh refinements

The results from a finite element analysis will in most cases contain a degree of discretization error. When the number of elements approaches infinity, the responses will converge towards exact results. However, when the number of elements increases, the analysis will be more time consuming. A certain degree of discretization error must therefore be tolerated. One effective way to measure the discretization error is by mesh refinements. The response from the mesh refinements can then be compared; if there are large differences between the meshes, further refinements will be needed in order to obtain convergence. 5 different mesh refinements have been applied in this project. A horizontal and a vertical load case are applied for each mesh refinement. The mesh refinements had the following properties and results:

Mesh no.	Soil elements	Nodes	Av. el. size [m]	H [kN]	V [kN]	Rel. H. err. [%]	Rel. V. err. [%]	Estimated Time [hours]
1	4,900	9,600	8.08	36,100	16,200	20.3	5.2	0.2
2	11,900	19,600	5.18	32,600	16,400	8.7	6.5	0.5
3	20,500	31,800	3.95	31,400	15,400	4.7	0.0	1
4	53,700	76,500	2.44	31,800	15,100	6.0	-2.0	4
5	182,000	255,000	1.22	30,000	15,400	-	-	15

Table 1 - Mesh refinements

The columns with relative error in table 1 show the response relative to mesh refinement number 5. The last mesh will also have a certain degree of discretization error. The last column gives a rough time estimate for one load case based on experience from this thesis. This calculation time will of course be dependent of several factors, although the ratio between the load cases might be of interest. The mesh refinements gave the following models in Plaxis 3D:

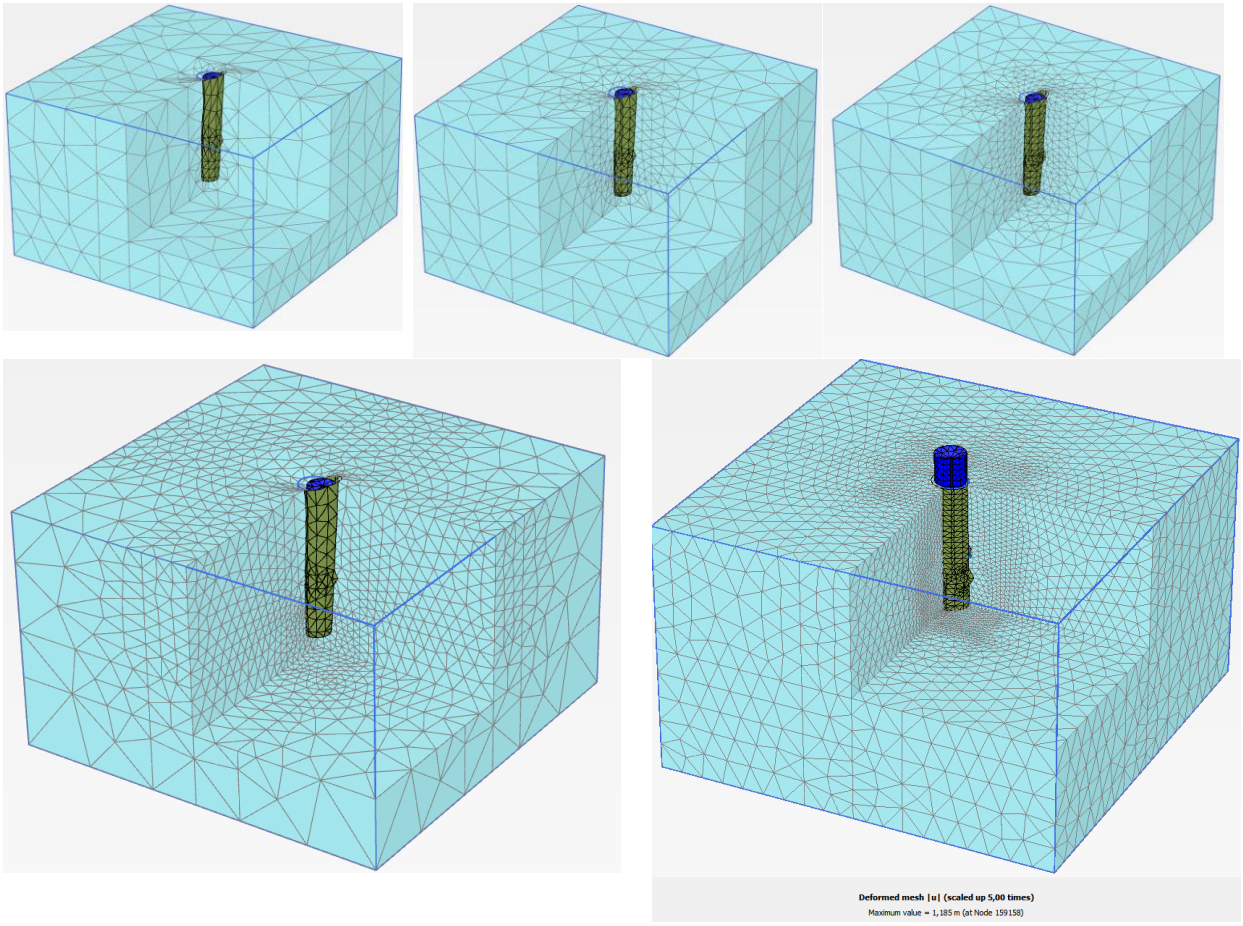

Figure 52 - Mesh refinements; (a) 4,900 el. (b) 11,900 el. (c) 20,500 el. (d) 53,700 el. (e) 182,000 el.

One way to compare the meshes is by plotting the number of elements against the response. The response in this setting is one meter padeye deflection, which is used as the definition of failure. The diagram shows the horizontal and the vertical response for the first four meshes.

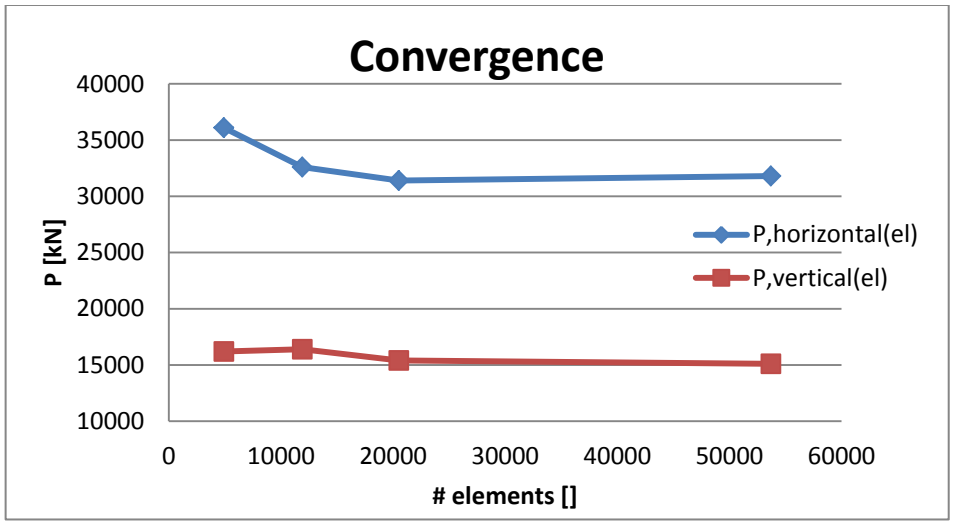

Figure 53 - Convergence - failure load against number of soil elements

It is observed from table 1 and figure 53 that an increase in the number of elements does not change the response in more than 6% when the number of elements has exceeded 20,000 elements. The discretization error is however likely to increase with further mesh refinements. During the mesh refinements, it has been focused on the density of the mesh where the failure mechanisms are likely to be developed, however in a somewhat smooth sense. This will increase the convergence rate when it is used in a proper way (Zienkiewicz *et. al*, 2005). The failure mechanisms will be different from the horizontal and the vertical load case. For the vertical load case, it is essential to have a large number of elements close to the base due to the reversed end bearing mechanism. The shaft resistance will be calculated accurately due to the interface elements. For the horizontal load case however, it will be important that there are a large number of elements close to the wall. The meshing options in Plaxis limits the user to control the density regions of the mesh, which means that some of the refinements favor the horizontal load case more than the vertical, and the other way around. This is mainly the reason that an increase in elements can increase the discretization error for a load case. However each mesh refinement will give an overall increased accuracy, which can be illustrated by averaging the error from the horizontal and the vertical load case. Figure 55 shows the important locations for a dense mesh due to the specific load case.

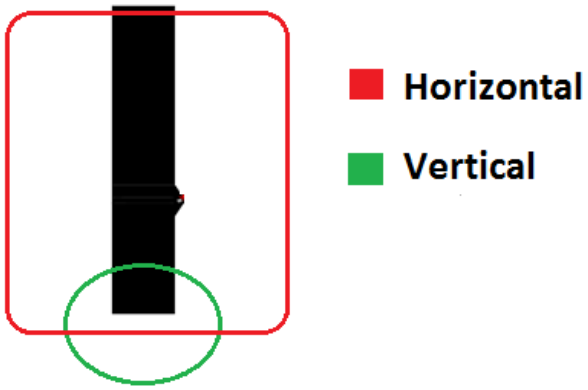

Figure 54 - Locations were a dense mesh is required

5 Results

In this chapter, the results will be presented. Based on the results from the mesh refinements, the model will be based on a mesh consisting of 20,500 soil elements. The results from the combined loading will be presented first. The combined loading includes 37 load cases, where the direction of the load vector was changed; both the inclination angle and the torsional angle were varied. Thereafter, the results from the hand calculation will be presented, followed by the load cases that correspond to the hand calculations. These analyses will also gain important information to form a realistic curve-fitting yield surface. Analyses addressing the effect on anchor stiffness will then be presented; it will be shown that the anchor can be considered rigid. Thereafter, the empirical elastic stiffness will be determined, and this will be used to form the elastic stiffness matrix of the system. Load sequences will then be executed, which will determine the plastic behavior due to cyclic two-way loads. Finally, empirical capacity curves for combined loading will be presented. The objective of each analysis can be summarized as follows:

Type of analysis	**Objective**	**Load cases**
Failure load at padeye	Yield surfaces and deflections	37
Hand calculations	Compare against numerical results	6
Failure loads for single-force components	Gain information for curve fitting	9
Elastic soil	Determine elastic force-displacement relationship	6
Parametric stiffness anchor	Obtain soil-structure interaction	4
Load cycles	Gain information regarding elasto-plasticity	3

Figure 55 - Analyses overview

5.1 Combined loading

The Plaxis results are based on the model that consists of 20,500 soil elements. Failure was defined as one meter padeye deflection. 37 load cases were applied, where the difference between the load cases was the direction of the load vector at the padeye. The following angles were combined:

$$\alpha = 0, 10, 20, 30, 45, 60, 90 \ \ [degrees]$$
$$\beta = 0, 5, 10, 20, 45, 90 \ \ [degrees]$$

Seven different load inclination angles and six different torsional angles were thus used. This results in 37 load cases, since the vertical load case is independent of the torsional moment; see chapter 4.2. The following failure loads were obtained for the different load cases:

P [kN]	β=0	β=5	β=10	β=20	β=45	β=90
α=0	31,400	30,100	27,800	18,300	9,000	6,300
α=10	34,000	33,000	29,700	18,700	9,100	6,400
α=20	36,100	34,600	30,400	19,400	9,500	6,800
α=30	29,700	29,100	26,700	19,700	10,300	7,300
α=45	21,600	21,500	21,000	18,700	12,200	8,900
α=60	17,700	17,700	17,700	17,100	14,400	11,700
α=90	15,400	15,400	15,400	15,400	15,400	15,400

Table 2 - Failure loads from padeye loads

5.1.1 Load-deflection curves

It is important to understand how the system behaves until failure. The load-deflection curves will therefore be presented. The load-deflection curves are separated in terms of the rotational angle; β.

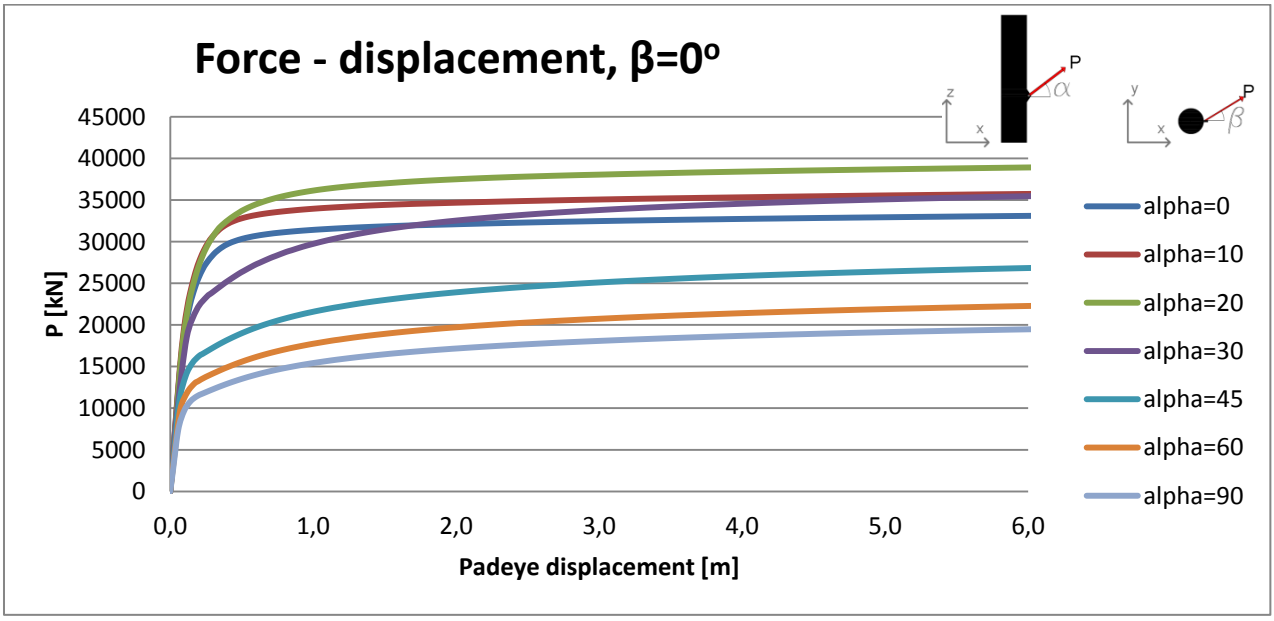

Figure 56 - Load-deflection curve, β=0 degrees

Figure 56 shows that the highest capacity is obtained when the load inclination angle α is 20 degrees. The horizontal loads have a well-defined yield plateau, while capacity increases more gradually when α is more than 30 degrees. It should be noted that Plaxis does not reduce the soil-structure contact area as the anchor deflects, which implies that the vertical load combinations will be slightly overestimated.

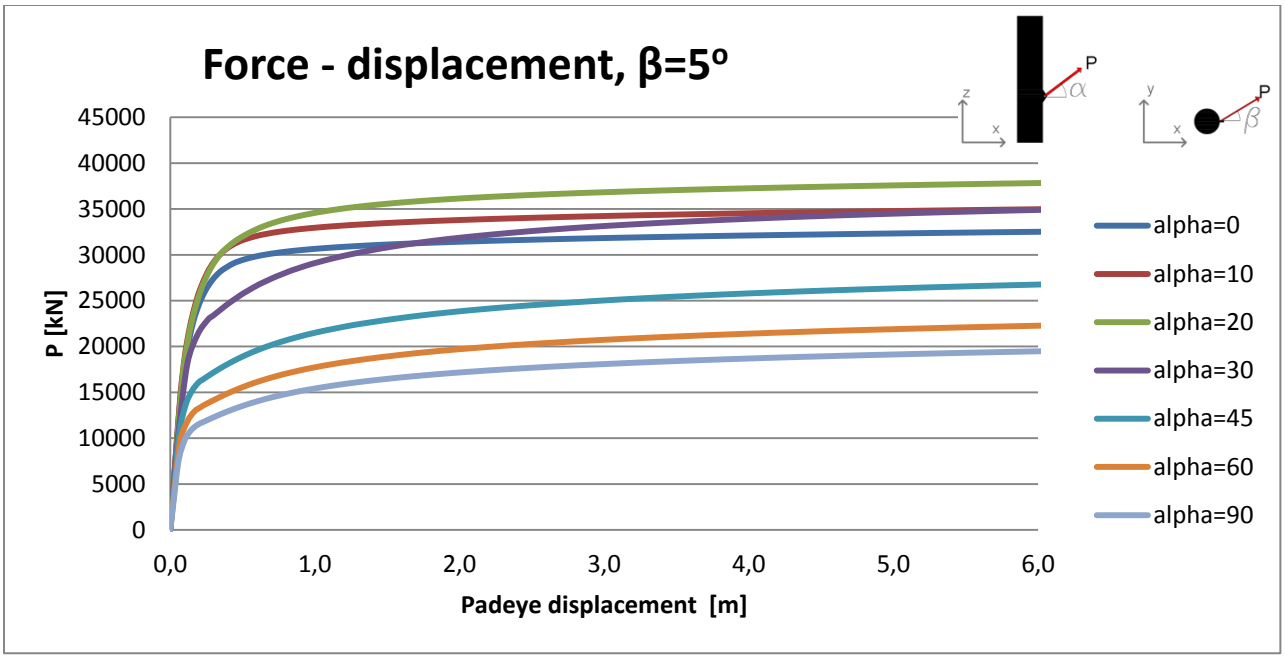

Figure 57 - Load-deflection curve, beta=5 degrees

Figure 57 shows the load combinations with β equals 5 degrees. The load-deformation pattern is much the same as for β equals 0. The capacity due to torsion is barely reduced.

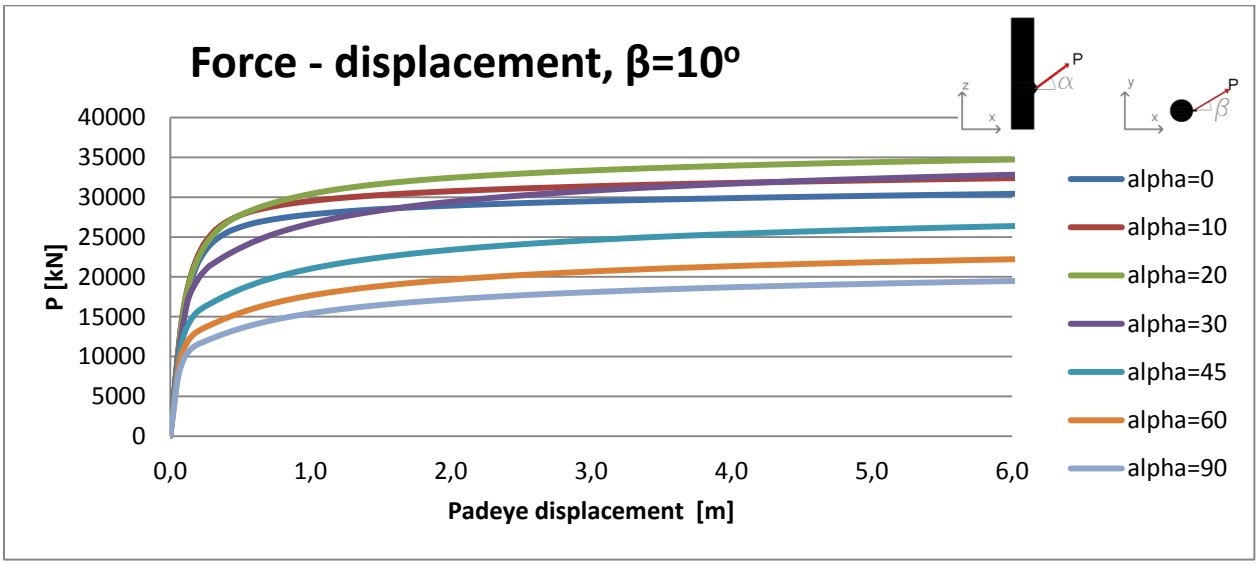

Figure 58 - Load-deflection, β=10 degrees

Figure 58 shows that the load-deformation pattern is still the same when β is 10 degrees, although the capacity for horizontal loads has been noticeably reduced due to the induced torsional moment. Also, the yielding plateau is less prominent.

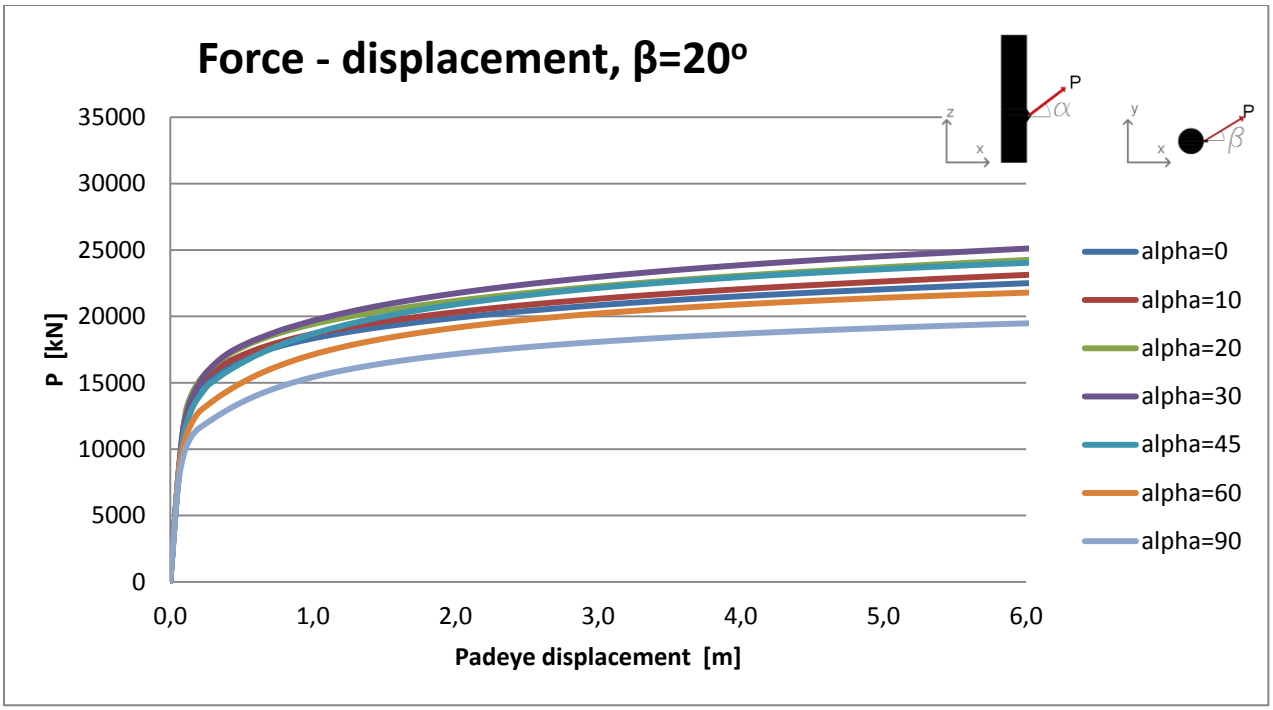

Figure 59 - Load-deflection curve, β=20 degrees

Figure 59 shows that the load-deflection curves were changed, and that the yielding plateau is also less defined for horizontal loads. The vertical loads are hardly reduced; this is explained by the fact that when the direction of the force is close to vertical, there is virtually no horizontal component left to induce a torsional moment.

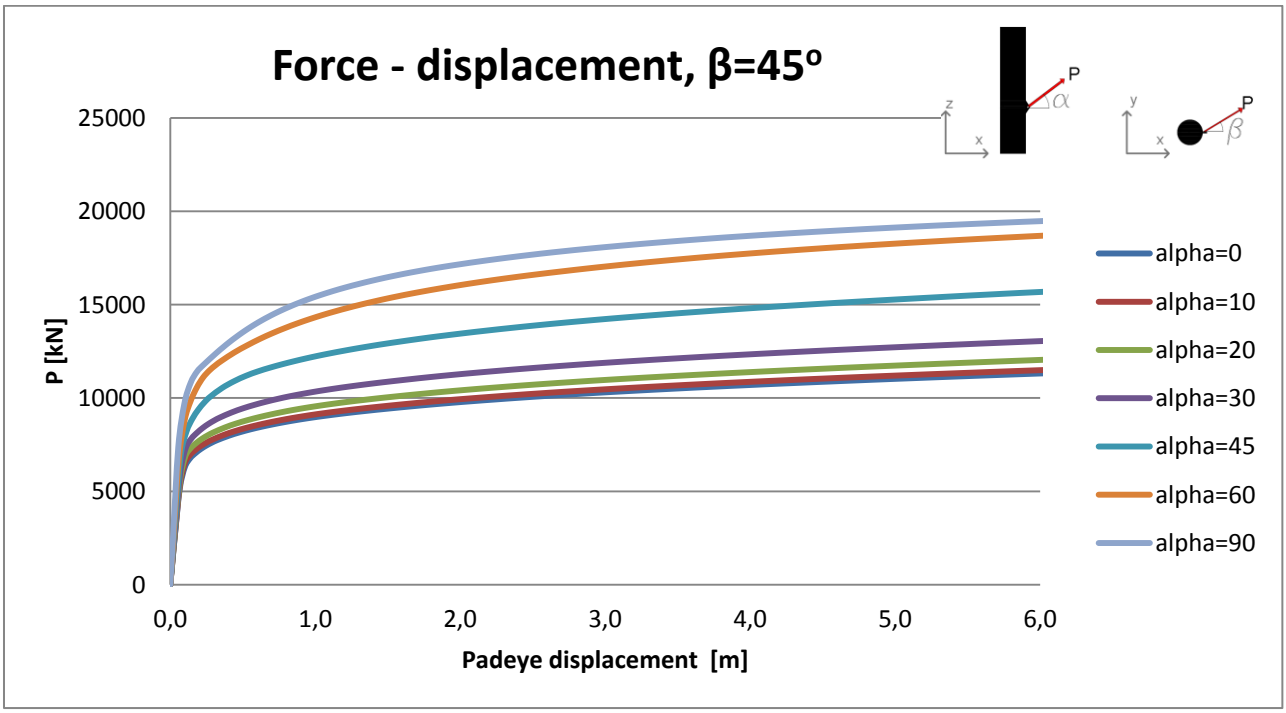

Figure 60 - Load-deflection curve, beta=45 deg

Figure 60 shows that the horizontal capacity is reduced significantly, clearly governed by the torsional moment capacity.

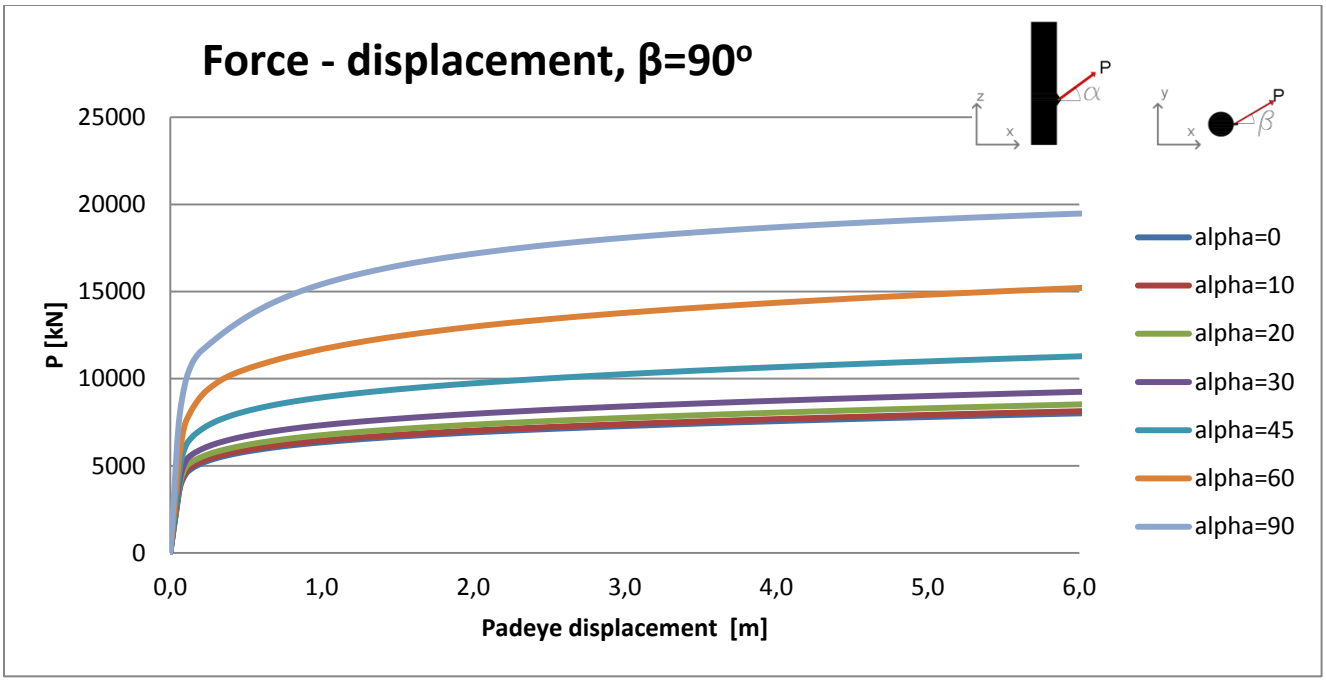

Figure 61 - Load-deflection curve, β=90 degrees

Figure 61 shows that horizontal loads are further reduced. These results are as expected.

All the load-deflection curves have one common property; the response is first approximately linearly-elastic prior to yielding. The curves start to yield after about 0.1 m deflection, when the loads are mobilized at about half of the total capacity. The stiffness in the elastic range seems to be related to the strength of the load case.

5.1.2 Failure mechanisms

It is necessary to study the failure mode of the system in order to evaluate whether the results are reasonable. The failure mechanisms from the analyses where the torsional angle is 0 will be presented. Failure mechanisms will be visualized by incremental strains and incremental displacements for chosen load cases.

Incremental strains

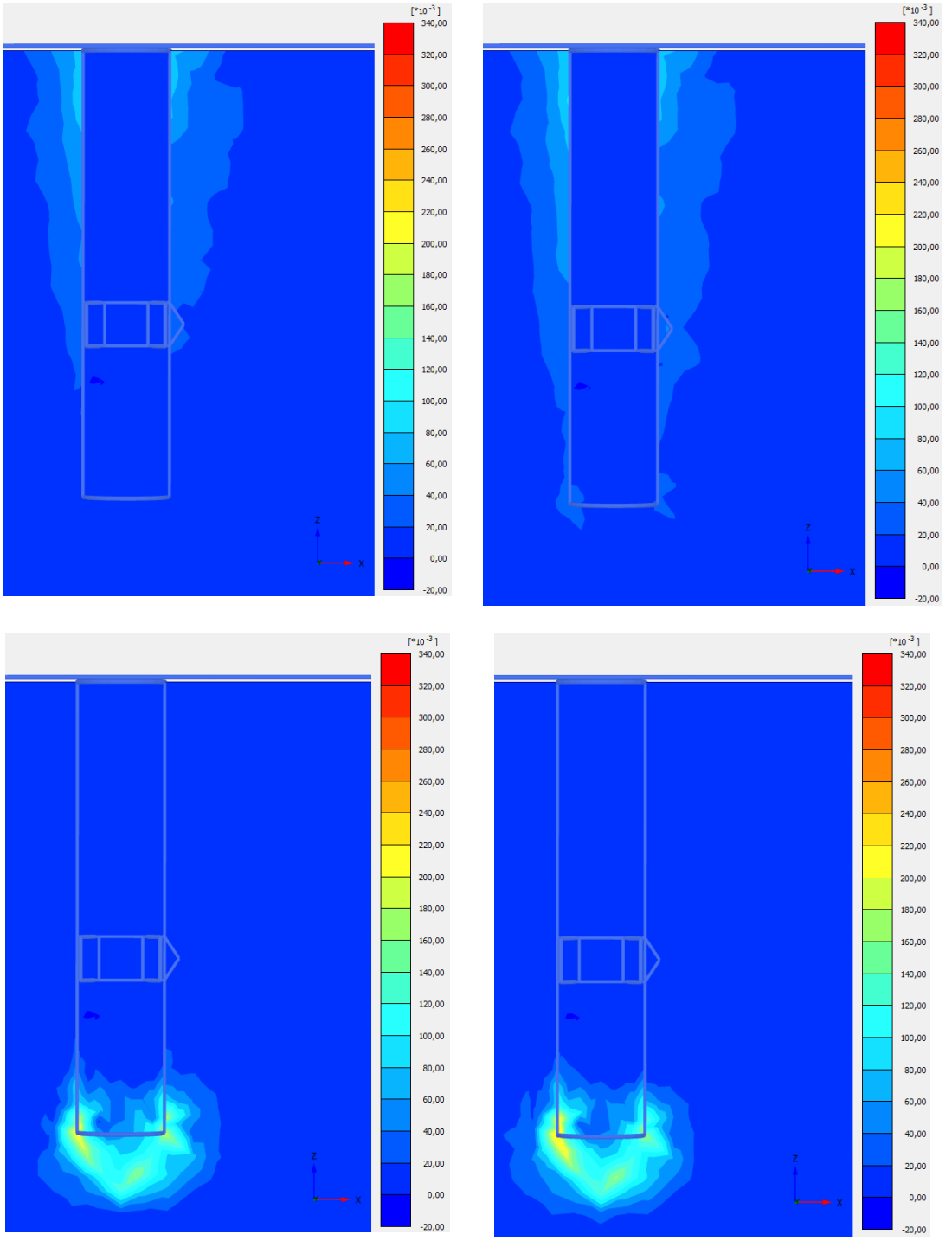

Figure 62 - Incremental strains, β=0 degrees: (a) α=0 degrees, (b) α=20 degrees, (c) α=45 degrees, (d) α=90 degrees

When the inclination angle is increased from 0 to 20 degrees, the soil at the base mobilizes, and a larger capacity is obtained. When the inclination angle is 45 degrees, the failure mechanism is vertical, with a reversed end-bearing capacity being obtained. The mechanisms at inclination angles of 45 and 90 degrees are identical.

Incremental displacements

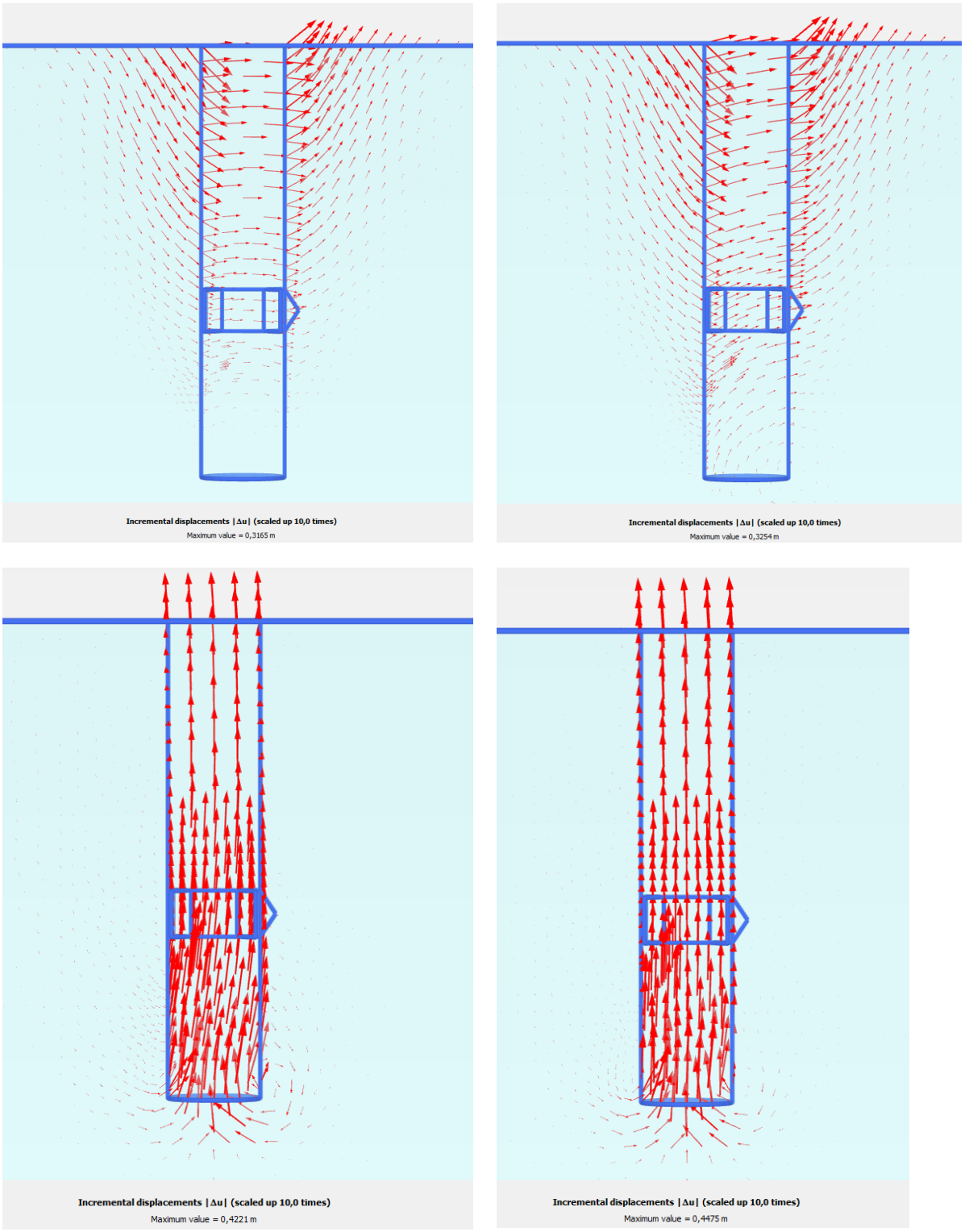

Figure 63 - Incremental disp., β=0 degrees: (a) α=0 degrees, (b) α=20 degrees, (c) α=45 degrees, (d) α=90 degrees

The same conclusions hold true for the incremental displacements as for the incremental shear strains.

Incremental displacements anchor, β=0 degrees

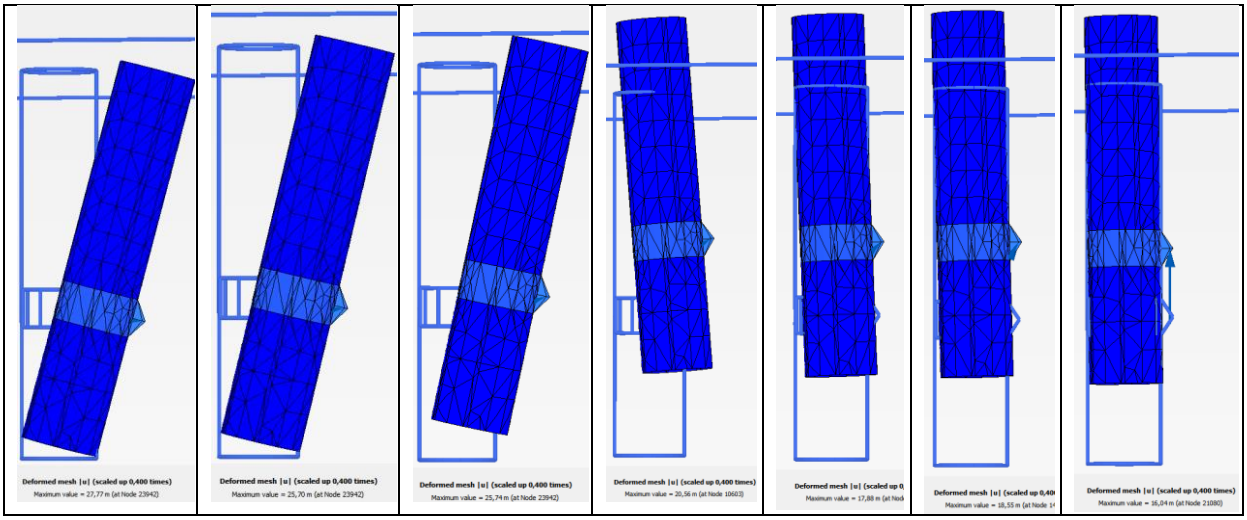

Figure 64 - Incremental displacements anchor,β=0: (a) α=0, (b) α=10, (c) α=20, (d) α=30, (e) α=45, (f) α=60, (g) α=90

Another way of visualizing the failure modes is to isolate the anchor from the soil in the output. The failure modes in terms of incremental displacements of the anchor for the inclination angles between 0 and 90 degrees when β=0 is shown is figure 64. It shows the same characteristics observed previously.

5.1.3 Failure surfaces in two dimensions

The results from the load cases can be plotted in several ways, with the horizontal-vertical load space being commonly used. The horizontal component of the force vector is plotted against the vertical force component. In the following ,a HV space with different torsional angles will be shown, which means that it is actually a HVβ-space, see figure 65.

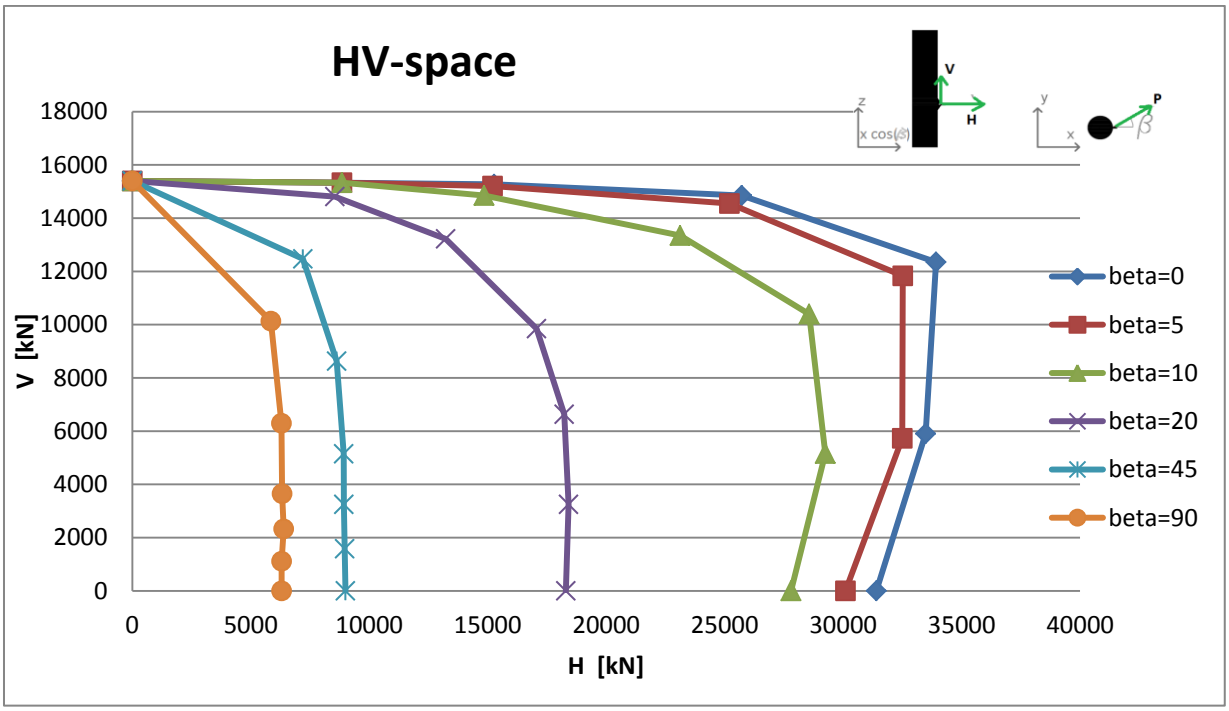

Figure 65 - HV space

Each point of the curves represent a failure state, given in table 2. The HV space shows several interesting tendencies. Firstly, it shows how a torsional angle will reduce the capacity of the system. When the angle β is 5 degrees, the capacity is almost unchanged, but when β increases, the capacity suddenly drops. Secondly, it can be seen that when the inclination angle α increases from 0, the horizontal capacity also increases. This can be explained as follows: Even though the results are presented in the HV space, there are other force components as well; namely the bending moments and the torsional moment. It turns out that when you load the system with an incremental vertical load, you will also unload the system of bending moments, if the horizontal component dominates. This will be further explored in section 5.5. Finally, we see that all the β curves intersect when α is 90 degrees. Again, this is because the horizontal component of the force vector dissipates, and there is no horizontal force left to cause torsion.

In order to see how much the torsional angle β reduces the capacity, it may be convenient to plot the inclination angle α against the failure load. Figure 66 shows how the failure load depends on the inclination angle α, and the torsional angle β. The failure load tendencies in the figure correspond to those of the other figures.

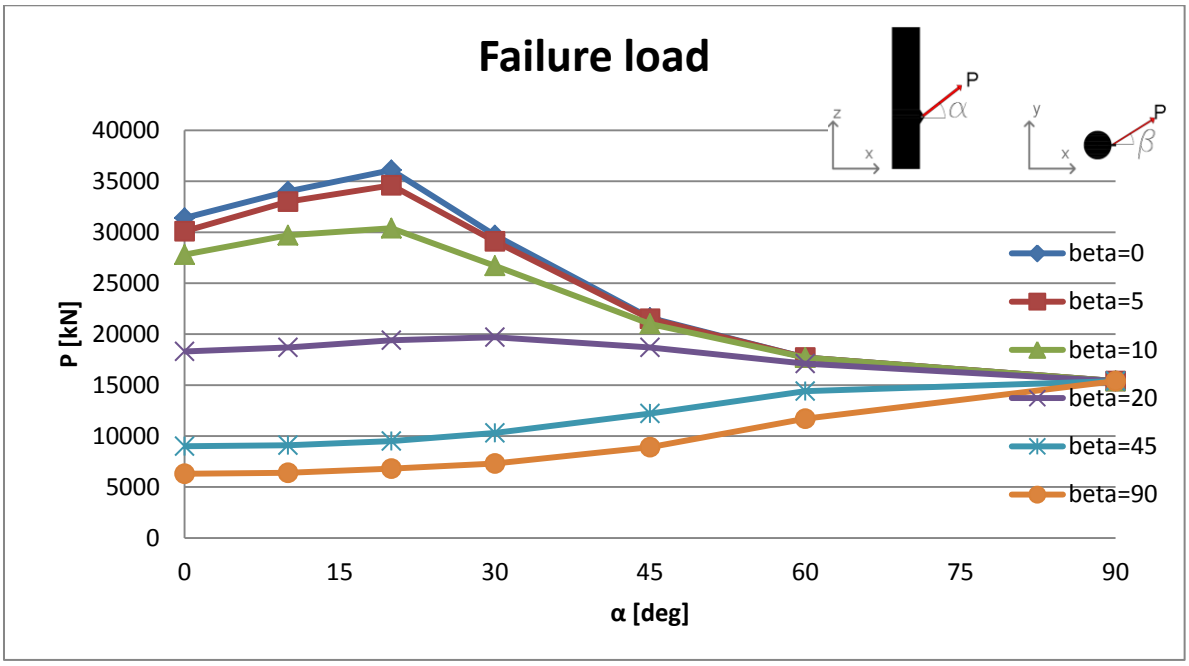

Figure 66 - Failure load P with the angles alpha and beta

If the chosen definition of failure is a 5-meter padeye deflection, the following HV space would be obtained:

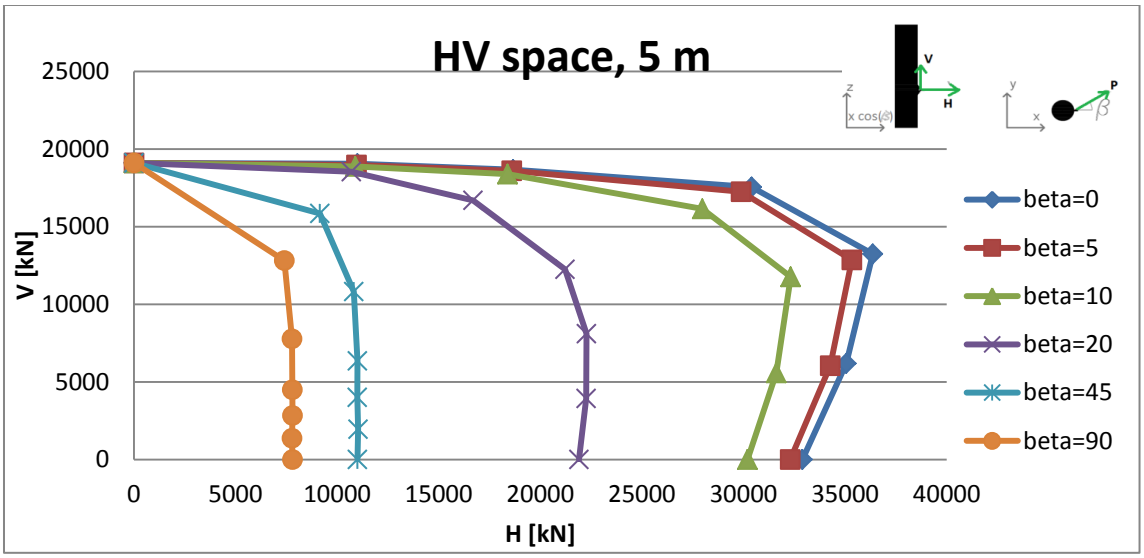

Figure 67 - HV space, failure defined as 5 m deflection

Figure 67 shows the HV space where failure is defined as a 5-meter deflection at the padeye. The vertical forces increased significantly from the HV space where failure was defined as 1-meter padeye deflection, while the change in horizontal capacity is less marked. The shapes of the different HV spaces are much the same.

Capacity curves with other deformation criteria with no torsion are also shown.

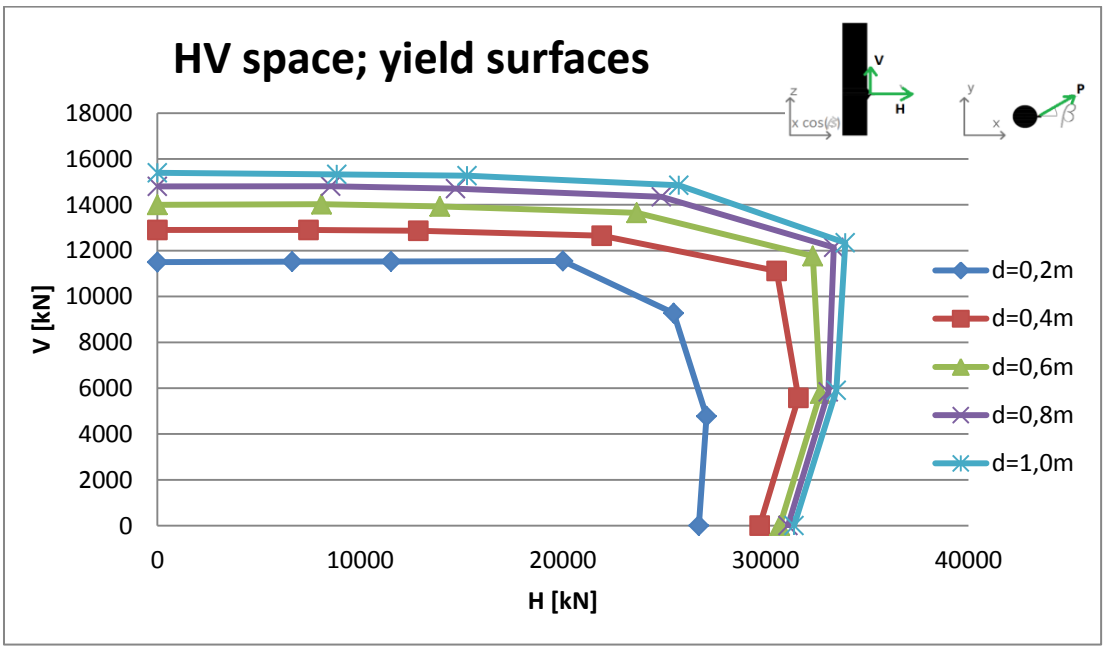

Figure 68 - Yield surface in HV space; deflection criteria: 0.2 m, 0.4 m, 0.6 m, 0.8 m and 1 m

5.1.4 Three-dimensional plots

Since the force vector applied at padeye consists of three independent components, see equations 4.8-4.15, the response can be visualized in the space with three components as well. One option might be to transform components into the HVT-space, which consist the total horizontal, vertical and torsional load components. H and V are already given, while T is simply H multiplied by sin(β) times e_x, where e_x is the eccentricity between the neutral axis and the load attachment point. The results can also be plotted directly in the H_xH_yV-space, where H_x is the decomposed horizontal load in the x-direction and H_y is the decomposed horizontal load in the y-direction.

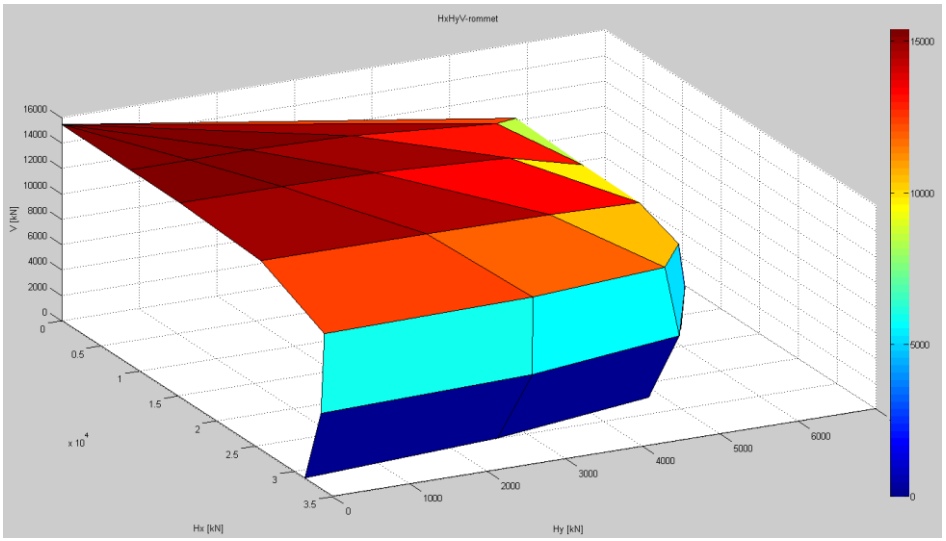

Figure 69 - HxHyV space

Another option is to plot the failure load P as a function of the angles α and β, see figure 69.

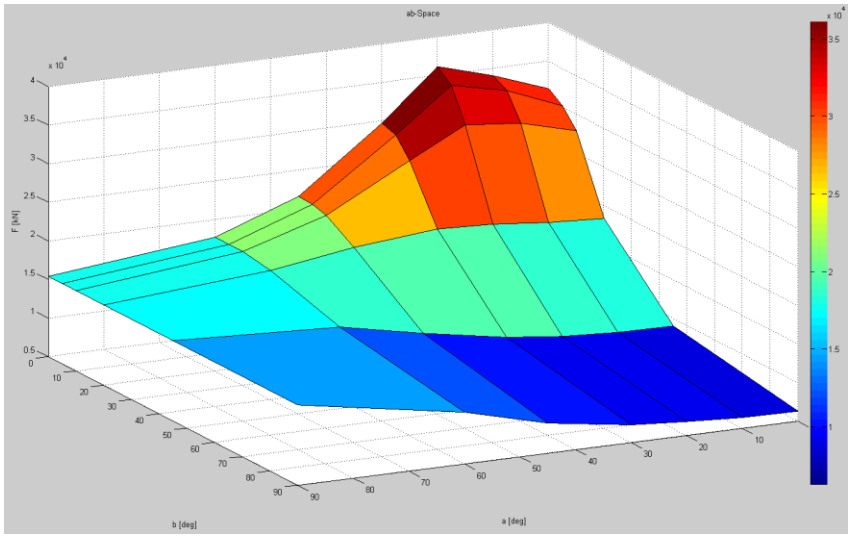

Figure 70 - P-αβ-space

Figure 69 and 70 has showed that the response can be visualized in by three-dimensional plots, but that it may be more difficult to interpret the tendencies.

5.2 Hand calculations

It is important to estimate the results from a numerical study by hand calculation in order to ensure that the numerical analyses are reasonable. The predictions should ideally be made prior to the analyses, in order to avoid adjustments in the hand calculations to get a good match. It is also important that the hand calculations use the same parameters as the numerical model. The hand calculations in this section include the ultimate force components of the anchor and the horizontal and vertical stiffness. Due to symmetry, neglecting the effects from the padeye, there are a total of four force components that need to be determined; the horizontal, the vertical, the bending moment and the torsional moment capacity.

5.2.1 Horizontal capacity

According to Randolph et al. (1998), the horizontal capacity can be estimated by figure 71:

$$H = NLD * \bar{s}_u = (11 * 30 * 6 * 17)kN = 33{,}700kN \tag{5.1}$$

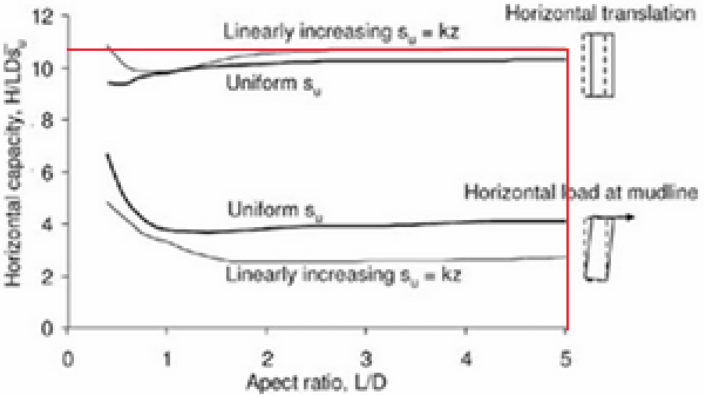

Figure 71 - Horizontal capacity (Randolph, 1998)

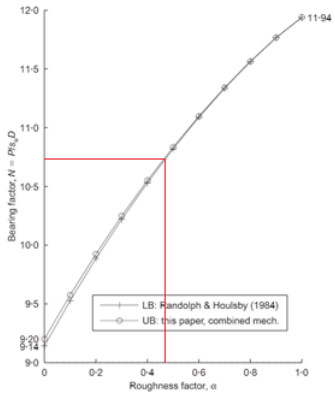

Figure 72 - Factor flow-around mechanism (Martin & Randolph, 2006)

Randolph & Gourvenec (2011) state that the flow-around mechanism will be developed close to the surface for soil with linearly increasing strength, and that the mechanism can be assumed to apply for the whole pile, since the soft soil at the seabed contributes little support. Figure 72 gives a value of 10.8 with a roughness factor α = 0.44. In this approach, the base shear also has to be included. The following capacity is then obtained:

$$H = NLD\bar{s}_u + H_{base} = \left(10.8 * 30 * 6 * 17 + \frac{1}{4}\pi * 6^2 * 32\right)kN = 34{,}000kN \tag{5.2}$$

Finally, the method of Aubeny & Murff (2005) will be presented. The base shear also had to be included in this case. The calculations are spreadsheet friendly, and are prepared in Excel with small depth increments (Δz=0.1 m, 300 increments). A spreadsheet with larger increments is attached for illustration. The method gave a capacity of H=32,300 kN. The following diagrams were obtained:

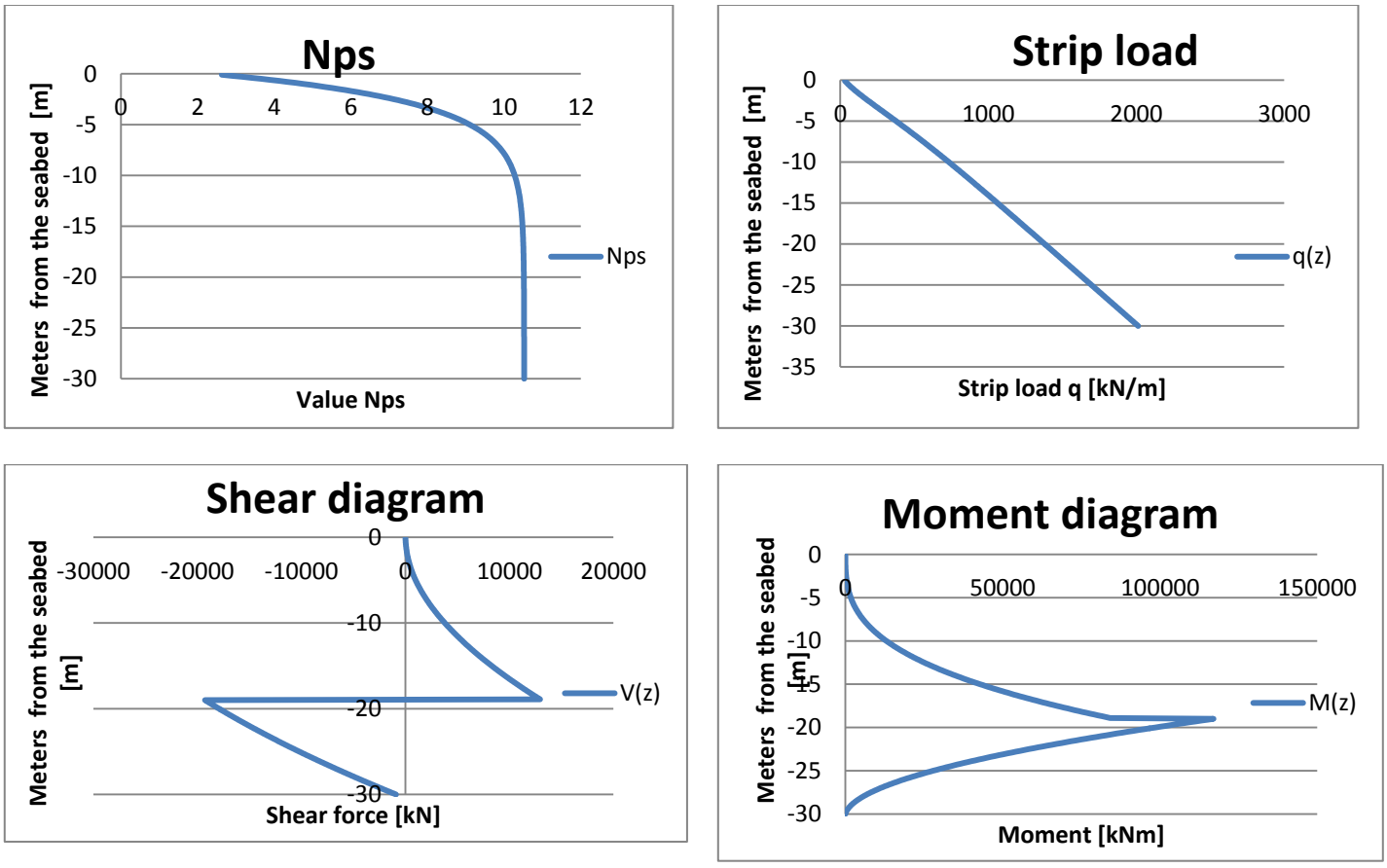

Figure 73 - Diagrams for the suction anchor

Three different ways of calculating the horizontal capacity have now been executed. The results were almost the same; between 32,300 kN and 34,000 kN.

5.2.2 Vertical capacity

The maximum vertical pull-out capacity can be calculated by many methods. However, most methods will not capture the coefficients that are used for this project. The limit equilibrium where the anchor is treated as a pile is a good way to estimate the capacity. The equilibrium in the undrained condition gives:

$$V_u = \pi L D \alpha \bar{s_u} + \frac{1}{4}\pi N_c D^2 s_u(L) + W' \tag{5.3}$$

The weight of the anchor is the following:

$$\begin{aligned} W = \sum \gamma A t = & \frac{78kN}{m^3} \\ & * \left(0.032m * 27m * 6m * \pi + 0.07m * 3m * 6m * \pi + 0.04m * \pi \right. \\ & \left. * (3m)^2 + 0.04m * (3m * 6m + 4 * 3m * 3m) + 0.3m * \frac{3m * 1m}{2}\right) \\ & = 1{,}870kN \end{aligned} \tag{5.4}$$

The effective weight of the anchor is taken as:

$$W' = \frac{\gamma'}{\gamma} W = \frac{68}{78} * 1{,}870kN = 1{,}630kN \tag{5.5}$$

The reverse end-bearing capacity factor N_C is taken as 9, which should be a conservative value for the given input parameters. See chapter 3.2.2 for more details. The undrained shear strength is taken at base level. The following capacity is obtained:

$$V_u = \pi * 30m * 6m * 0.44 * 17kPa + \frac{1}{4}\pi * 9 * (6m)^2 * 32kPa + 1{,}630kN = 14{,}000kN \tag{5.6}$$

If the chosen value of N_c was taken as 12, the capacity would be 16,700 kN. The calculated vertical capacity is thus 14,000 kN, but a higher capacity is expected in the model. The reverse end-bearing capacity for this anchor represents about half of the total capacity.

5.2.3 Bending moment capacity

The bending moment capacity is calculated from the limit equilibrium where the lateral forces acting on the suction anchor are treated as a linearly increasing strip load. This leads to the following bending moment capacity:

$$\sum H = 0 \tag{5.7}$$

$$\sum M = 0 \tag{5.8}$$

$$\xrightarrow{leads\ to} M_u = \frac{1}{2}H_u * \frac{2}{3} * \frac{1}{3}L + \frac{1}{3}H_u * \frac{1}{3} * \frac{1}{2}L + \left(\frac{1}{2} - \frac{1}{3}\right) H_u * \frac{1}{3} * \frac{2}{3}L = \frac{11}{54}H_u L \simeq 0.2H_u L \tag{5.9}$$

If the horizontal capacity is taken as 34,000 kN, the ultimate bending moment will be 204,000 kNm. Since the bending moment capacity is only dependent on the horizontal capacity, the discretization error is likely to be approximately the same. However, it is unlikely that the limiting earth pressure will be fully mobilized close to the rotation center. On the other hand, the shear forces at the interfaces might also add a small portion to the bending moment capacity.

5.2.4 Torsional capacity

The torsional capacity will also be estimated from the limit equilibrium. Three factors contribute to the capacity; the shaft resistance, the base resistance and the resistance due to the padeye. This leads to the following expression:

$$T_u = \frac{1}{2}\alpha * \bar{s}_u * L * \pi * D^2 + \frac{1}{12} * s_u(L) * D^3 + e_x * N_c * s_u(padeye) * A_{padeye} \tag{5.10}$$

The last term relates to the padeye modeled as a plate. The bearing capacity factor for a plate due to the flow-around mechanism can be taken as 12.5, which is typical for drag anchors (Randolph & Gourvenec, 2011). The eccentricity; ex, is the distance between the neutral axis and the resultant force from the plate, taken as 3.5 meters. Inserting these values gives:

$$T_u = \frac{1}{2}0.44 * 17kPa * 30m * \pi 6^2 + \frac{1}{12} * 32kPa * \pi 6^3 + 3.5m * 12.5 * 21kPa * 1.5m^2$$

$$T_u = 12{,}790kNm + 1{,}810kNm + 1{,}380kNm = 16{,}000kNm \tag{5.11}$$

The estimated torsional capacity is thus 16,000 kNm.

5.2.5 Stiffness

The vertical stiffness is first calculated in accordance with Paulos and David (1974). The height of the model is 50 meters, while the length of the pile is 30 meters, which gives a height-to-length ratio equal to 1.67. This gives an influence factor; I_ρ, equal to 0.7, while the influence factor would be 1.1 if the model had an infinite depth. It should be noted that the method assumes constant stiffness, while the stiffness in the model is almost proportional to depth. An average stiffness over the pile length is applied. The following stiffness is obtained with this method:

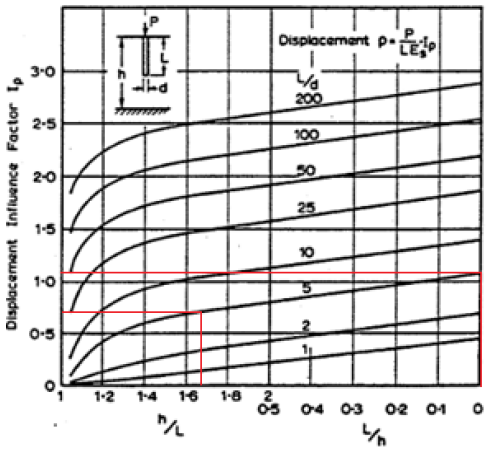

Figure 74 - Influence factor axially loaded pile (Poulos & David, 1974)

$$k = \frac{L * \bar{E}_s}{I_\rho} = \frac{30m * 3 * 100 * \left(2 + \frac{30}{2}\right) kPa}{0.7} = 219{,}000 kN/m \qquad (5.12)$$

The fact that the method is based on a constant stiffness makes the method less comparable to the model. The method of Randolph & Gourvenec (2011) takes stiffness changes into account, and is thus better suited. The stiffness of the pile is divided into the shaft stiffness and the base stiffness, which behave like additive springs. The following stiffness is obtained:

$$k_v = k_{shaft} + k_{base} = \frac{2\pi}{\zeta} L\bar{G} + \frac{4}{(1-v)} R_{base} G_{base} \qquad (5.13)$$

where ζ is an influence parameter for the size of the soil volume, often taken as 4
R_{base} is the radius of the pile at the pile base
G_{base} is the shear stiffness at the pile base

Insertion gives a value k_v=157,000 kN/m.

The horizontal stiffness is calculated by using the formula presented in chapter 3.2.2:

$$k_h = 4L\bar{G} = 4 * 30m * 100 * 17kPa = 204{,}000 kN/m \qquad (5.14)$$

The horizontal stiffness is thus 204,000 kN/m.

5.2.6 Summary of the hand calculations

Hand calculations on both strength and stiffness have now been performed. The results will be used to evaluate the reliability of the numerical results. The hand calculations showed the following results:

Horizontal capacity	32,300 kN – 34,000 kN
Vertical capacity	14,000 kN
Bending moment capacity	194,000-204,000 kNm
Torsional moment capacity	16,000 kNm
Horizontal stiffness	204,000 kN/m
Vertical stiffness	157,000 kN/m

Table 3 - Results from hand calculations

5.3 Single-force components with Plaxis 3D

In order to calculate the ultimate force components of the anchor, separate analyses were executed, where each load component was loaded separately. Due to the constraint relations of the loads, the single-force components were represented with a set of load vectors, where the resultant force intersected with the three neutral planes in space; load vectors applied at the padeye will result in six force components, and it is not possible to isolate the individual components. Two of the neutral planes are known prior to analyses, due to symmetry, while the eccentricity between the padeye and the neutral plane in the z-direction; e_z, needs to be obtained. Failure was defined as one meter padeye deflection. The results from these analyses will provide important information, which will be used to construct a realistic failure surface, and will also be used for comparison with the hand calculations.

The first step required is to determine the neutral axis of the anchor. Due to symmetry, the neutral axis in the xz-plane and the yz-plane will intersect in the middle of the cylinder. This gives an eccentricity to the load attachment point in the x-direction of 3.75 meters, while there is no eccentricity in the y-direction; e_x=3.75 m, e_y=0. The definition of the neutral axis in the xy-plane in this context is the plane that induces no bending moment due to horizontal loads. Since horizontal loads in this plane will not produce any bending moment, the largest horizontal capacity will be obtained in this plane. This property can be exploited; the loading plane can be changed until the largest capacity is obtained. The loading plane has been lowered by combining a horizontal load at the padeye with a bending moment, represented by coupled forces. The eccentricity from the padeye will then be e_z=M/H. Firstly, four load cases where applied; namely e_z=M/H=2.25 m, 3.0 m, 3.75 m and 4.5 m. The following load-deflection curves were obtained:

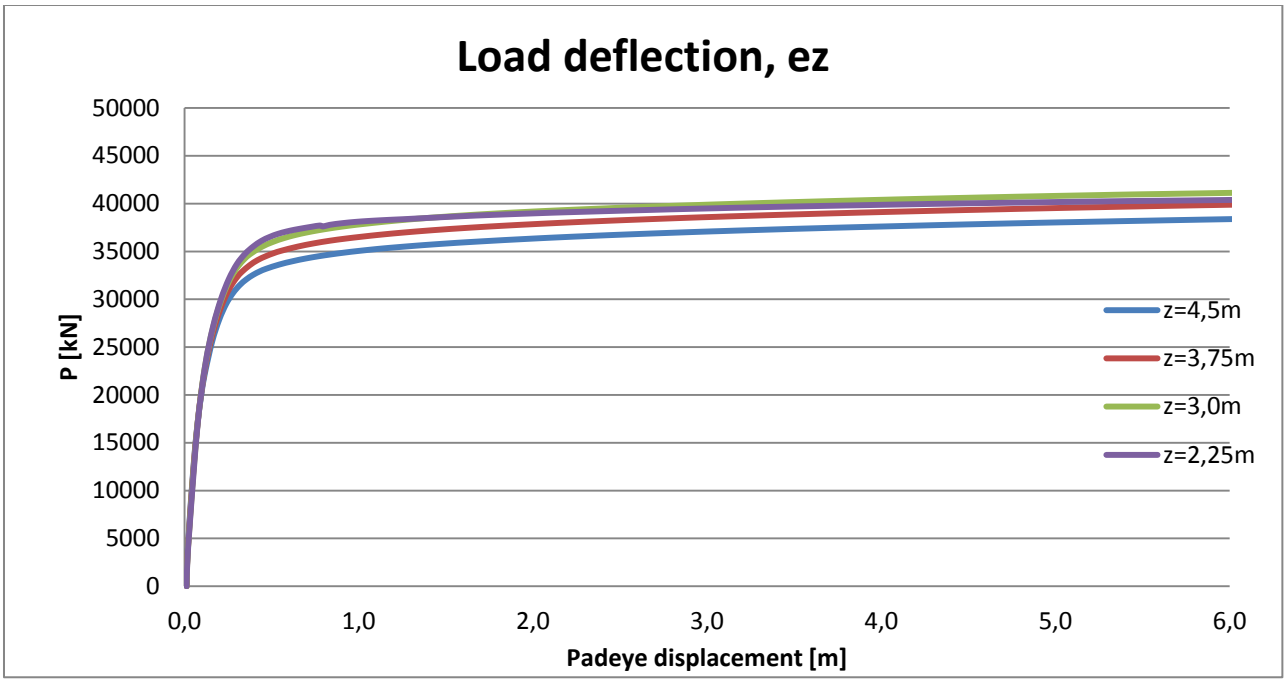

Figure 75 - Parametric study of ez

It is seen that 3 meter eccentricity will result in the largest capacity. The second largest was the load case where the eccentricity was 2.25 meters. Further analyses with eccentricities of 2.50 meters and 2.75 meters were then executed, in order to determine the eccentricity in greater detail. However, an eccentricity of 3 meters was still the load case that gave the largest capacity. Selected failure mechanisms from the analyses will be shown:

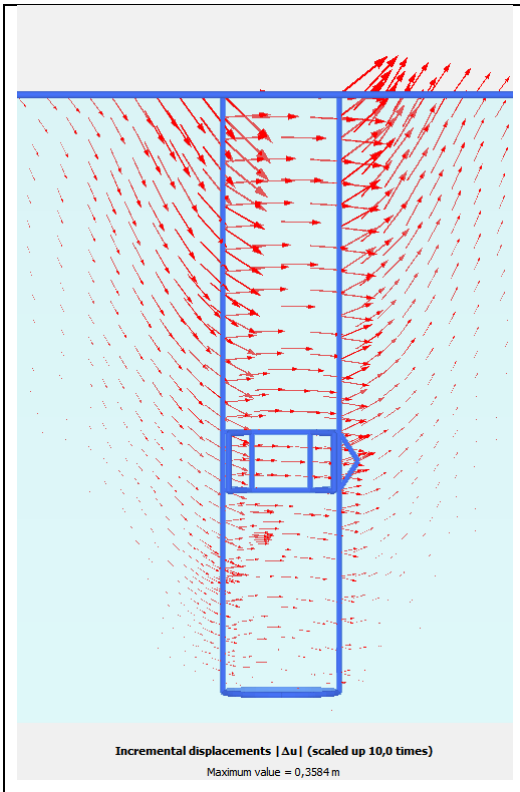	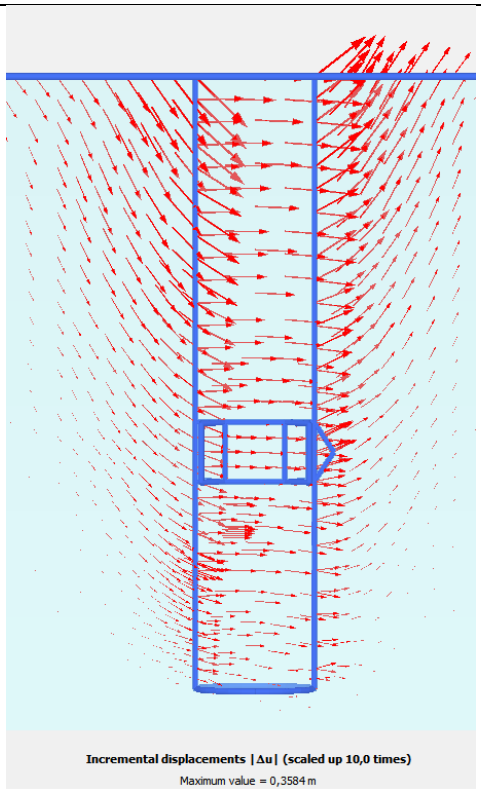
Horizontal load, z=2.25 meters	Horizontal load, z=2.5 meters

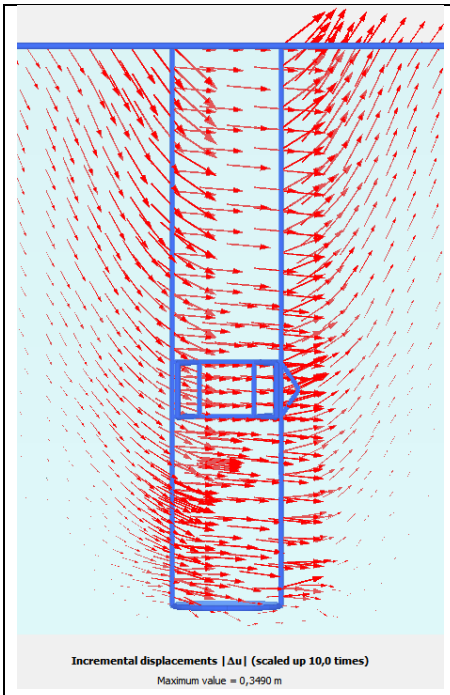

Horizontal load, z=2.75 meters

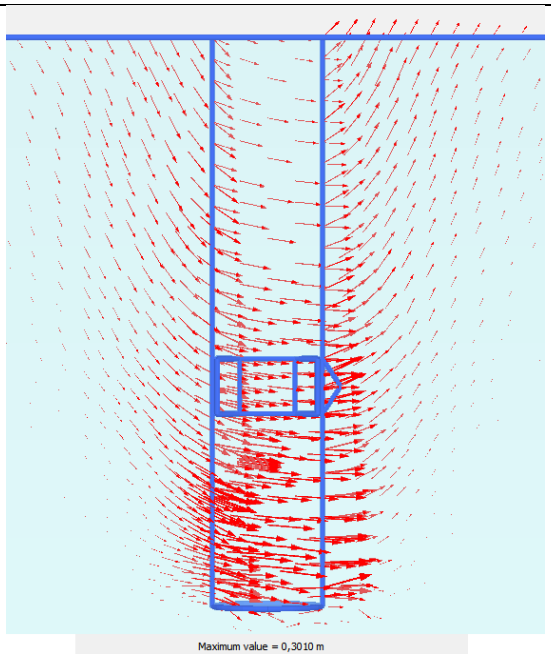

Horizontal load, z=3 meters

Figure 76 - Incremental displacements; parametric study of ez

Figure 76 shows that the anchor mainly translates without rotation at eccentricities of 2.75 and 3 meters. The capacity can then be fully mobilized. It is seen that the anchor translates more at the base than at the top with an eccentricity of 3 meters (insignificant in practice). The reason for this is that the unit resistance earth pressure is considerably larger at the bottom.

The eccentricity; $e_{z,}$ is taken as 3 meters. This means that when the anchor is loaded horizontally, it will cause a bending moment of $M_y=H_x*e_z= M_y=3m*H_x$ The analyses also give an ultimate horizontal capacity of 38,000 kN when failure is defined as 1 meter padeye deflection.

It should be noted that e_z, the vertical distance between the padeye and the plane that gives the largest horizontal capacity, is a plastic property. It does not contain any information about the elastic properties. An elastic xy-plane will be introduced in the generalization chapter, with the following definition: When a horizontal load is applied in the elastic xy-plane, the anchor will translate without rotation. It will be shown that these planes will not coincide.

The other single-force components can then be analyzed. The load cases were performed with coupled forces that were applied close to the padeye, which resulted in only the desired force component. The following results were obtained:

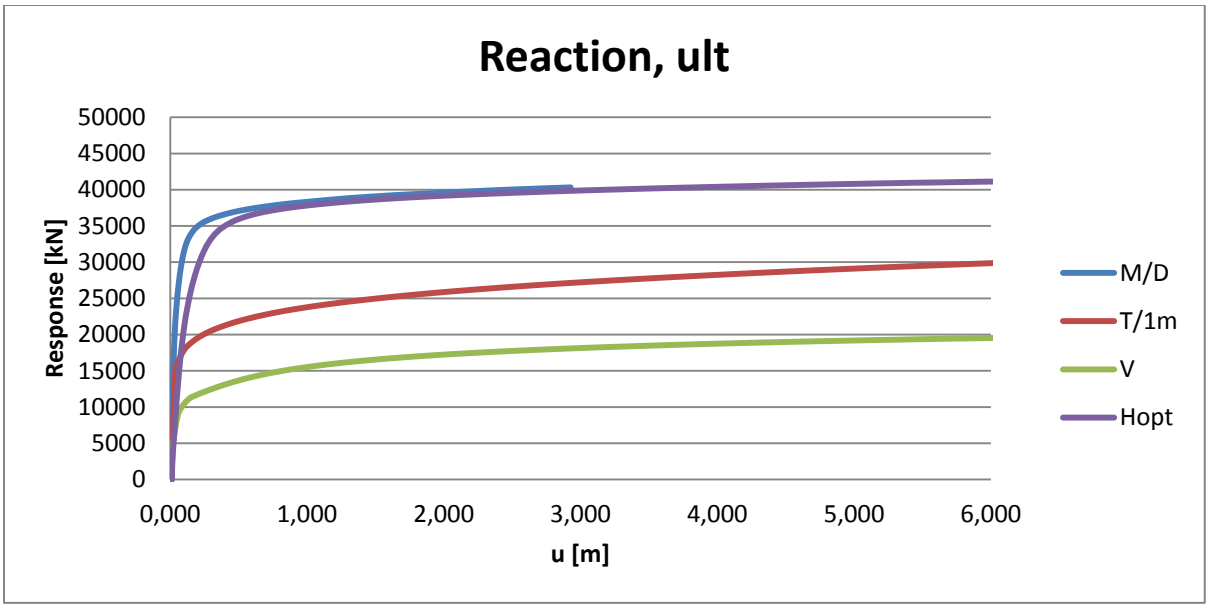

Figure 77 - Load-deflection curves

Figure 77 shows the load-deflection curves from the load cases that have only one force component. The deflections are still measured at the padeye. Note that the bending moment in the figure is divided by the diameter D=6 m and that the torsional moment is divided by 1 meter. This is done to achieve the same dimensions and values in the same range. The bending moment was about the y-axis. It is assumed that the moments and the horizontal forces had the same capacity in the x- and the y-direction, due to the minor impact of the padeye geometry. The ultimate capacity is defined as the load that causes 1-meter padeye deflection.

The results from the force component analyses can be summarized as follows:

Description	Symbol	label	value
Distance in the x-direction from the padeye to the neutral axis	e_x	[m]	3.75
Distance in the y-direction from the padeye to the neutral axis	e_y	[m]	0
Distance in the z-direction from the padeye to the plastic neutral axis	e_z	[m]	3
Ultimate horizontal force	$H_u = H_{x,u} = H_{y,u}$	[kN]	38,000
Ultimate vertical force	V_u	[kN]	15,500
Ultimate bending moment	$M_u = M_{x,u} = M_{y,u}$	[kNm]	230,000
Ultimate torsional moment	T_u	[kNm]	23,800

Table 4 - Eccentricities and ultimate forces

The ultimate capacities can be compared to the combined loading analyses. An inclination angle; α, and a torsional angle; β, of 0 gave a capacity of 314,00 kN, while the ultimate horizontal capacity is 38,000 kN. Because of the plastic eccentricity of 3 meters, the capacity will be reduced by about 17%. For that load case, the mobilization factor of the bending moment was f=31,400kN*3m/230,000kNm=41%. The vertical load case gave a capacity of 15,400 kN, while the ultimate vertical capacity was 15,500 kN. This means that the influence of the 3.75 meter eccentricity due to vertical loads can in practice be neglected. The mobilization factor for the bending moment of the vertical load case was f=15,400kN*3.75m/230,000kNm=25%. An angle α of 0 and an angle β of 90 degrees give a capacity of 6,300 kN. This gives a torsional moment of T=6,300kN*3.75m=23,600kNm, while the ultimate torsional moment is 23,800 kNm. This means that the capacity for this load case is totally governed by the torsional capacity.

5.4 Stiffness of the anchor

One assumption that is often made during suction anchor calculations is that the anchor is rigid. The soil-structure interaction will then be quite simple, and forces can then be transposed to force components without any simplification. Analyses that study the relation between the stiffness of the anchor and the load-deflection curve have been carried out, in order to check if the assumption is reasonable. Four load cases have been performed, with the difference between each load case being the E-modulus to the anchor. The force vector is horizontal, and is applied at the padeye.

The E-modulus is the following for the different load cases:

Load Case 1	E1 [MPa]	$E_{steel}*10^{-4}$	21
Load Case 2	E2 [MPa]	$E_{steel}*10^{-2}$	2,100
Load Case 2	E3 [MPa]	E_{steel}	210,000
Load Case 4	E4 [MPa]	$E_{steel}*10^{2}$	21,000,000

Table 5 - E-modulus load cases

This resulted in the following force-displacement curves:

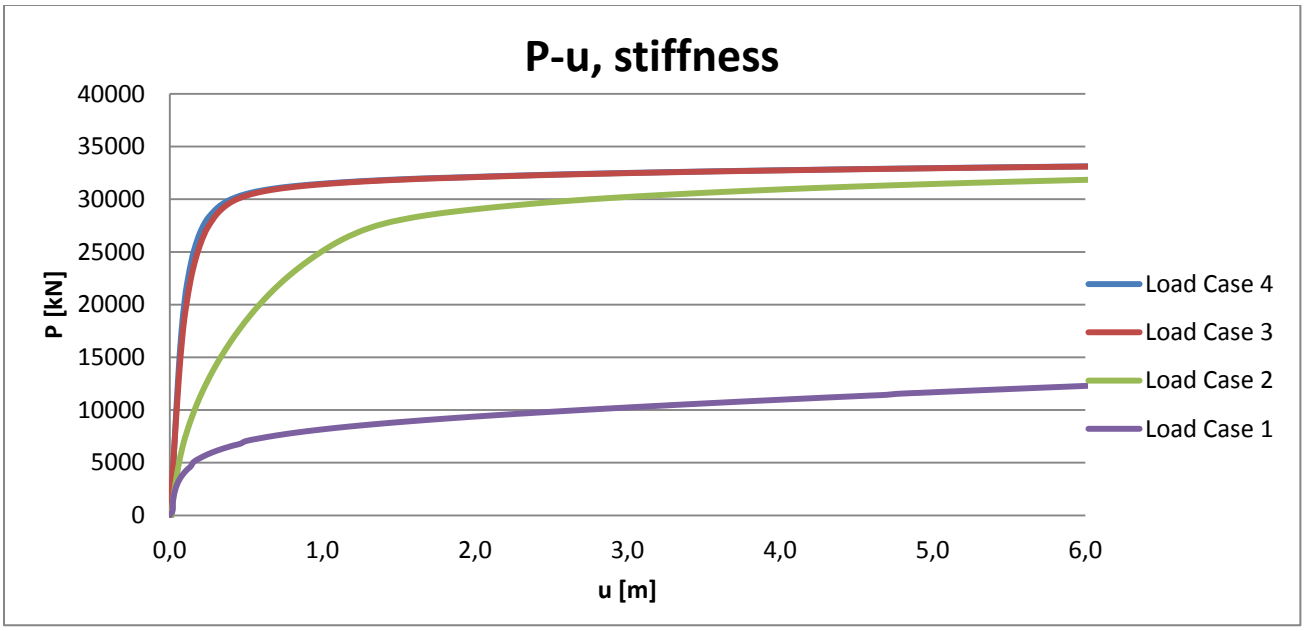

Figure 78 - Load-displacement curve parametric stiffness

Figure 78 shows how the soil response depends on the stiffness of the structure. Load Case 3 has the original stiffness. If the Young's modulus is increased 100 times, the response is more or less exactly the same. This implies that the system can be assumed to be rigid. The figure shows that if the Young's modulus was decreased 100 times, the soil-structure interaction would become important. It is interesting to note that when the padeye deflection increases, the capacity is almost the same as for the original load case. When E is reduced 10,000 times, most of the capacity at practical displacements has dissipated.

5.5 Elastic soil response

The elastic soil response is needed for the elasto-plastic formulation, and will in addition give information about expected deflections due to small loads. It will be shown that a linearly-elastic response can be assumed for loads until the mobilization degree f=0.6 is reached. Further loading will cause plastic deflection and a hardening law is needed. Plastic deformations will be covered in the next chapter; elasto-plasticity.

The stiffness matrix in the exercise is obtained by force-displacement relations at the padeye. Three separate orthogonal forces are applied at the padeye, and the corresponding padeye displacements are measured. The set of orthogonal forces comprises H_x, H_y and V; the two horizontal forces and the vertical force, respectively. The relations will give the flexibility matrix, and the stiffness matrix can easily be obtained by inversing the flexibility matrix. The flexibility coefficients are determined by empirical curve fitting to the associated load-deflection curves; the elastic part is predicted as the part of the load-deflection curves with a linear behavior, and intersects the load-deflection curves when the mobilization factor are 0.6. The stiffness can then be regarded as an secant modulus.

Deflection in the x-direction due to the orthogonal load cases:

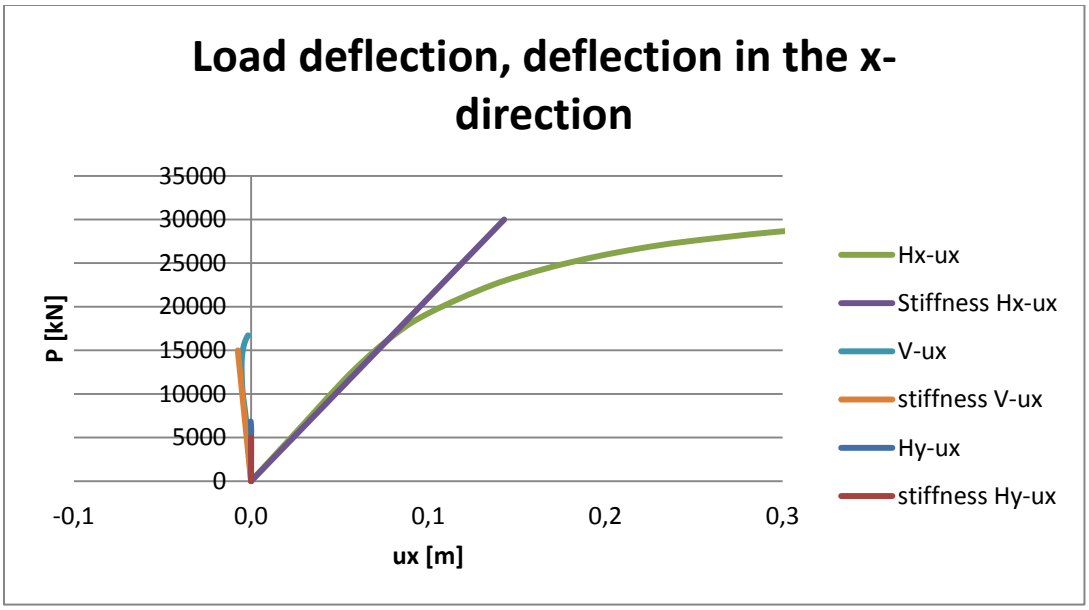

Figure 79 - Load deflection; deflections measured in the x-direction

Deflection in the y-direction due to the orthogonal load cases:

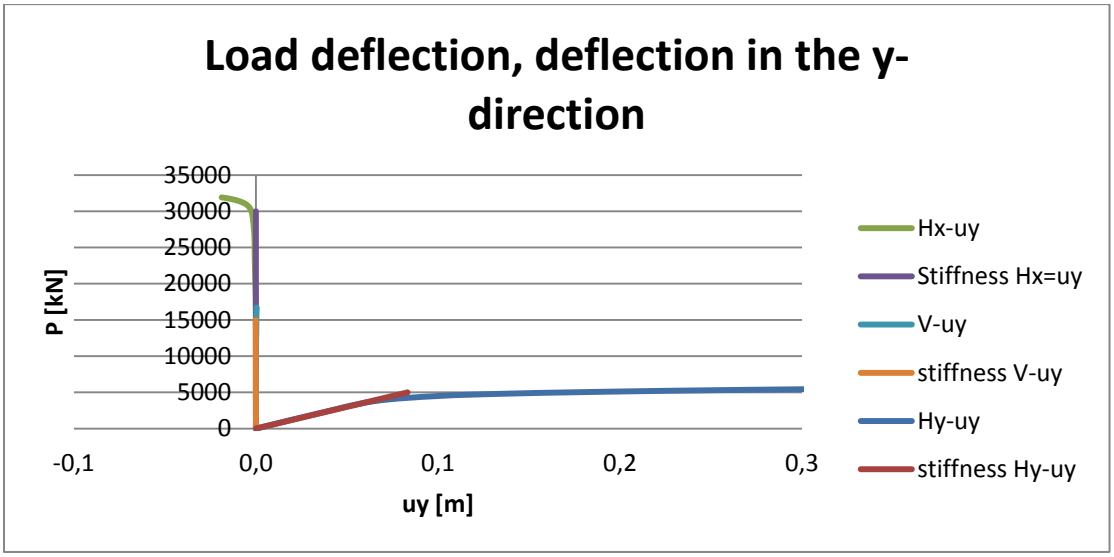

Figure 80 - Load deflection; deflection measured in the y-direction

Deflection in the z-direction due to the orthogonal load cases:

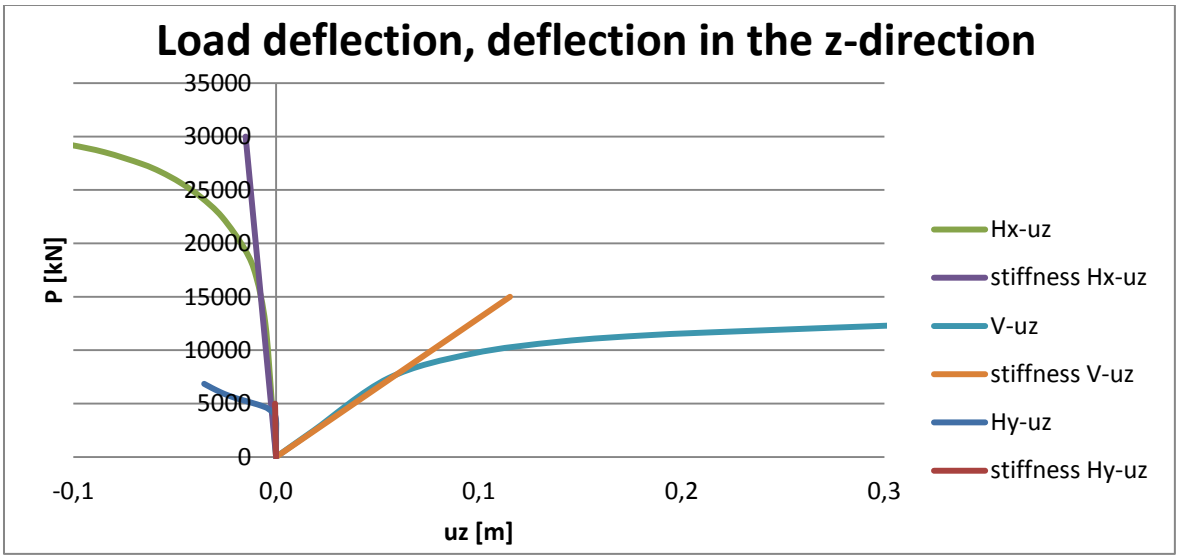

Figure 81 - Load deflection; deflection measured in the z-direction

The empirical elastic curves correspond to the load-deflection curves in a proper way for small loads; the assumption of an initial elastic behavior is thus appropriate. The yielding starts to affect the load-deflection curves when the mobilization factor; f, is approximately 0.6 for all the orthogonal load cases. The yielding plateau in the load-deflection curves is prominent for all directions. The following flexibility matrix is obtained by curve fitting:

$$[K]^{-1} = \begin{bmatrix} \frac{1}{21} & \frac{1}{\infty} & \frac{1}{-200} \\ \frac{1}{\infty} & \frac{1}{6} & \frac{1}{\infty} \\ \frac{1}{-200} & \frac{1}{\infty} & \frac{1}{13} \end{bmatrix} * \frac{10^{-4}m}{kN} \qquad (5.15)$$

The stiffness matrix of the system is found by inverting the flexibility matrix:

$$[K] = \begin{bmatrix} 211 & 0 & 14 \\ 0 & 60 & 0 \\ 14 & 0 & 131 \end{bmatrix} * 10^3 kN/m \qquad (5.16)$$

The stiffness matrix is important for the elasto-plastic formulation and for the dynamical response of the system. The stiffness of the foundation will have an impact on the eigenfrequencies of the platform. For simplicity, assume that the suction anchor is the foundation for a tension leg platform in 500-meter deep waters. The stiffness of the cable can be approximated as k_{cable}=EA/L. Appropriate dimensions give a vertical cable stiffness of about 40,000kN/m. The stiffness of the system due to the stiffness of the foundation will then be $k = (131{,}000^{-1} + 40{,}000^{-1})^{-1} kN/m = 30{,}600\text{kN/m}$ and a change in the vertical eigenfrequency of 14 percent. In other words, the stiffness of the foundation does have a significant impact on the dynamical response and should be accounted for.

5.6 Load cycles

Cycles of elasto-plastic loads have been executed in order to gain information about realistic elasto-plastic behavior. Three different load-case histories have been performed; one in each of the x-, y-

and z-directions. Firstly, the anchor was loaded to a mobilization factor f=0.9, then unloaded again until f=0.9, and finally reloaded to f=0.9. The following results were obtained:

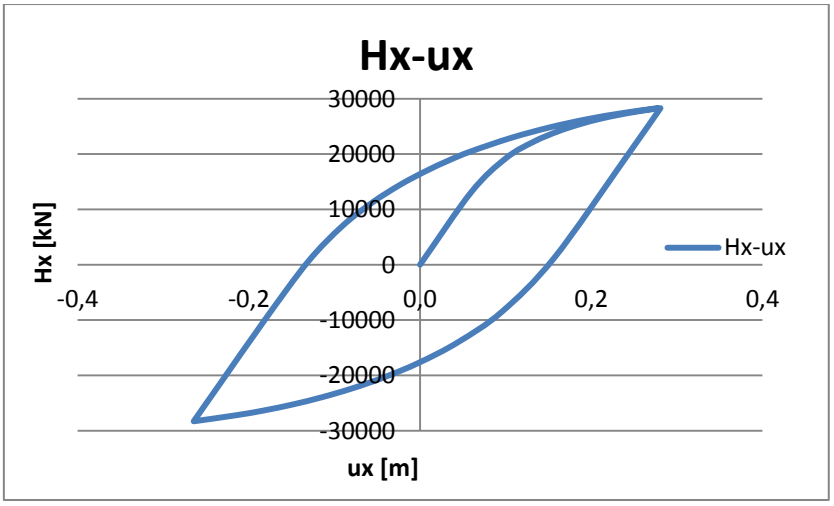

Figure 82 - Loads and deflections in the x-direction

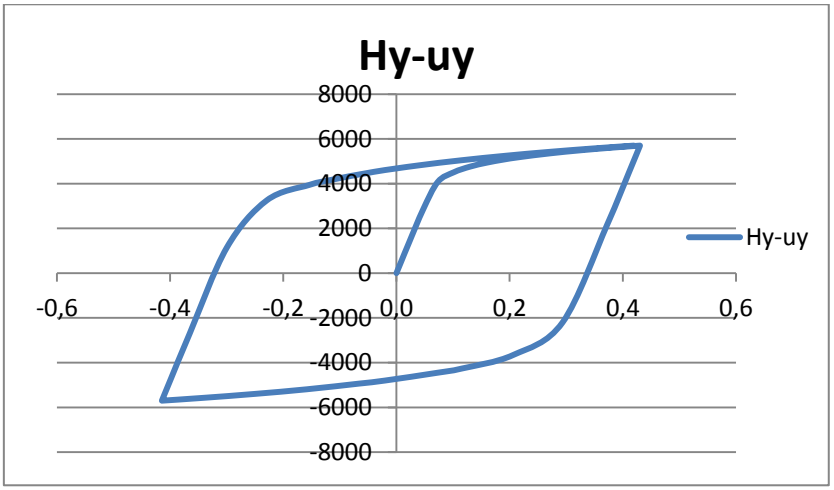

Figure 83 - Loads and deflections in the y-direction

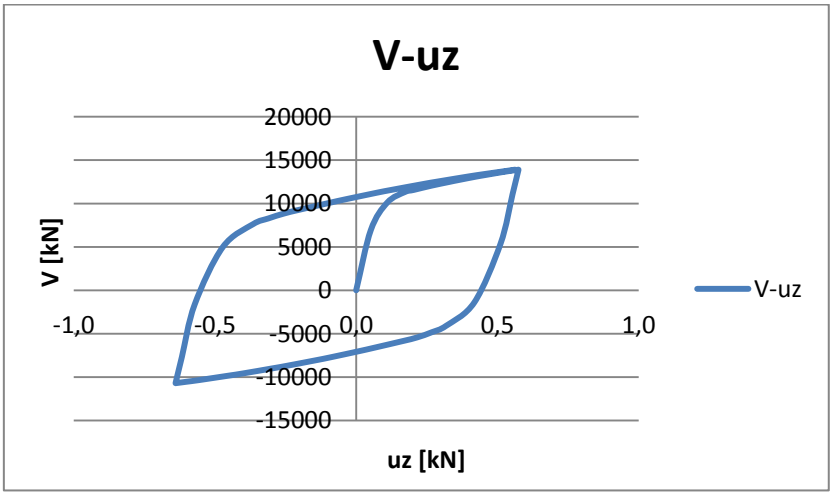

Figure 84 - Loads and deflections in the z-direction

The loading cycles in all directions show the same tendency; namely that the loading cycles form a closed loop and that the Bauschinger effect is present. This imposes kinematic hardening rather than isotropic hardening. The material properties at element level is modeled as elastic-perfectly plastic, which means that the yield surface will not expand during loading. It is thus reasonable that the yield surface neither will expand at a global level, only translate. However, the system cannot be subjected to a compression force in reality, since the mooring chain is not capable of transferring tensile loads. Isotropic hardening is also more commonly applied.

Also note that the compression force in the vertical load cycle is less than the tensile force. This is because the weight of the anchor reduces the compression capacity, while it will increase the tensile capacity.

5.7 Curve-fitting yield surfaces

Two different curve-fitting yield surfaces will be presented in this section. The difference between them is how the bending moment is included. The second formula has a better physical foundation, and also provides the most accurate results. For this specific problem it is required that the curve-fitting formula cooperates with all 6 force components that will be presented during a general load at the padeye. However, since the force components are constant to each other, it will still be possible to plot the curve-fitting formula in 3 dimensions. The yield surfaces will then be determined in terms of loads applied at the padeye.

5.7.1 The first curve-fitting yield surface

The first curve is based on the following formula:

$$\left(\frac{H_x}{H_u}\right)^a + \left(\frac{H_y}{H_u}\right)^a + \left(\frac{V}{V_u}\right)^b + \left(\frac{M_x}{M_u}\right)^c + \left(\frac{M_y}{M_u}\right)^c + \left(\frac{T}{T_u}\right)^d = 1 \tag{5.17}$$

where
H_x is the horizontal force in the x-direction
H_y is the horizontal force in the y-direction
V is the vertical force
M_x is the bending moment about the x-axis
M_y is the bending moment about the y-axis
T is the torsional moment
H_u is the ultimate horizontal force in the y-direction, equal to 38,000 kN
V_u is the ultimate vertical force, equal to 15,500 kN
M_u is the ultimate bending moment about the y-axis, equal to 230,000 kNm
T_u is the ultimate torsional moment capacity
a, b, c, d are curve-fitting constants

The coefficient a relates to both horizontal components and the coefficient d relates to both bending moments components, due to symmetry. It is thus only four coefficients that determine the surface. The moments can then be eliminated due to the constraints by using equations 4.11-4.13:

$$\left(\frac{H_x}{H_u}\right)^a + \left(\frac{H_y}{H_u}\right)^a + \left(\frac{V}{V_u}\right)^b + \left(\frac{H_y * e_z}{M_u}\right)^c + \left(\frac{|H_x * e_z - V * e_x|}{M_u}\right)^c + \left(\frac{H_y * e_x}{T_u}\right)^d = 1 \tag{5.18}$$

The equation can also be presented in terms of P, α and β by applying equations 4.10-4.13:

$$\left(\frac{P*\cos(\alpha)*\cos(\beta)}{H_u}\right)^a+\left(\frac{P*\cos(\alpha)*\sin(\beta)}{H_u}\right)^a+\left(\frac{P*\sin(\alpha)}{V_u}\right)^b+\left(\frac{P*e_z*\cos(\alpha)*\sin(\beta)}{M_u}\right)^c+\left(\frac{P*|e_z*\cos(\alpha)*\cos(\beta)-e_x*\sin(\alpha)|}{M_u}\right)^c+\left(\frac{P*e_x*\cos(\alpha)*\sin(\beta)}{T_u}\right)^d=1$$

(5.19)

The latter expression is useful in order to determine the magnitude of the force vector for given angles. This can for instance be done by Newton's iterations (Kreyszig, 2006):

$$P_{n+1}=P_n-\frac{F(P)_n}{F'(P)_n} \tag{5.20}$$

where:

$$F(P)=\left(\frac{P*\cos(\alpha)*\cos(\beta)}{H_u}\right)^a+\left(\frac{P*\cos(\alpha)*\sin(\beta)}{H_u}\right)^a+\left(\frac{P*\sin(\alpha)}{V_u}\right)^b+\left(\frac{P*e_z*\cos(\alpha)*\sin(\beta)}{M_u}\right)^c+\left(\frac{P*|e_z*\cos(\alpha)*\cos(\beta)-e_x*\sin(\alpha)|}{M_u}\right)^c+\left(\frac{P*e_x*\cos(\alpha)*\sin(\beta)}{T_u}\right)^d-1=0$$

(5.21)

It is important to have sufficient iterations to ensure convergence of the empirical surface. The following error tolerance has been applied:

$$error=\left|1-\frac{P_{n+1}}{P_n}\right|<10^{-5} \tag{5.21}$$

Optimization of the empirical coefficients can be achieved by the method of least squares (Kreyszig, 2006). Conservative adjustments can then be made manually. The following values for the coefficients were obtained at the end:

Coefficient	Value
a	3
b	5
c	1
d	4

Table 6 - Empirical coefficients

The empirical yield surface will be plotted against the Plaxis results after the second empirical yield surface is presented.

5.7.2 The second curve-fitting yield surface

The second curve-fitting formula uses the following formula:

$$\left(\frac{H_x}{H_u\left(1-\left(\frac{M_y}{M_u}\right)^d\right)}\right)^a + \left(\frac{H_y}{H_u\left(1-\left(\frac{M_x}{M_u}\right)^d\right)}\right)^a + \left(\frac{V}{V_u}\right)^b + \left(\frac{T}{T_u}\right)^c = 1 \qquad (5.22)$$

where H_x is the horizontal force in the x-direction
H_y is the horizontal force in the y-direction
V is the vertical force
M_x is the bending moment about the x-axis
M_y is the bending moment about the y-axis
T is the torsional moment
H_u is the ultimate horizontal force in the y-direction, equal to 38,000 kN
V_u is the ultimate vertical padeye force, equal to 15,400 kN
M_u is the ultimate bending moment about the y-axis, equal to 230,000 kNm
T_u is the ultimate torsional moment capacity
a, b, c, d are curve-fitting constants

The difference between the empirical yield surfaces is how the formulas interact with the bending moments. Since the pile can be considered rigid, a constraint relation between bending moments and translational forces can be expressed analytically if the earth pressure resistance can be expressed as a function. Due to the strength profile, the earth pressure per unit length can be approximated as linearly increasing; see chapter 5.2. The limit strip load can be simplified as follows:

$$q(z) = k * z = \frac{2 * H_u}{L^2} * z, \quad k = \frac{2 * H_u}{L^2} \qquad (5.23)$$

The simplified strip load and the calculated strip load can be compared (the base shear is distributed to the last pile meter):

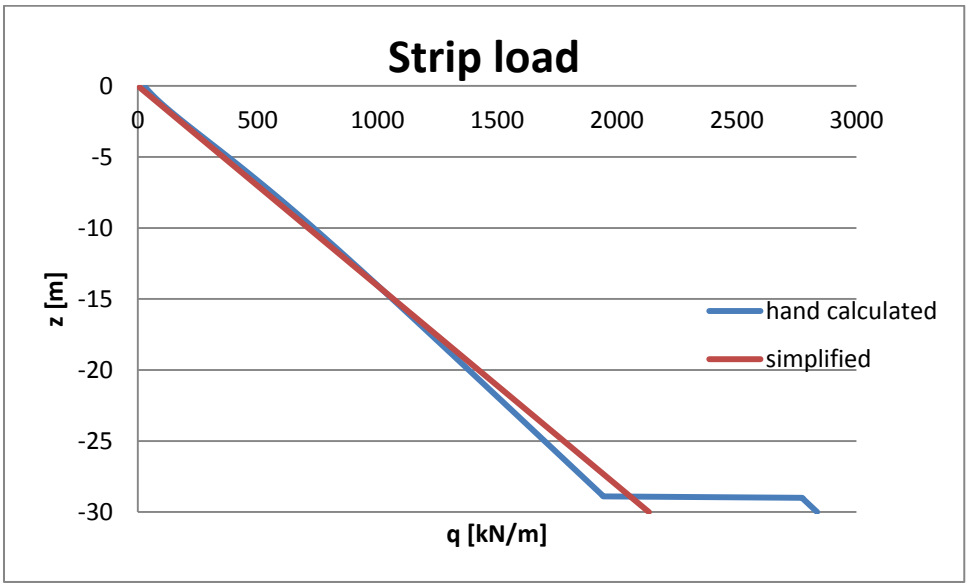

Figure 85 - Strip load; hand calculated and simplified

The analytical expression is obtained by solving the three equations below. The equations are based on the limit equilibrium, and exploit the property that the external moment can be expressed as the resultant force multiplied by the projected distance from the neutral point (where the three plastic planes intersect):

$$\sum H = 0 \tag{5.24}$$

$$\sum M = 0 \tag{5.25}$$

$$M = H * e \tag{5.26}$$

The eccentricity e, in the third equation denotes the distance between the horizontal neutral plane and the resultant force.

Equilibrium of the horizontal forces gives the following expression:

$$H = \frac{1}{2}k(L-h)^2 - k*(L-h)h - \frac{1}{2}kh^2 \tag{5.27}$$

A non-dimensional earth pressure-to-length ratio is introduced:

$$l = \frac{h}{L} \tag{5.28}$$

The expression can then be simplified as:

$$H = kL^2(l^2 - 2l + \frac{1}{2}) \tag{5.29}$$

Equilibrium of the bending moment gives the following expression:

$$M = 2(k(L-h)h\left(\frac{L}{3} - \frac{h}{2}\right) + \frac{1}{2}kh^2\frac{1}{3}(L-h)) \tag{5.30}$$

The expression can be rewritten as:

$$M = \frac{2kL^3}{3}(l^3 - 2l^2 + l) \tag{5.31}$$

Applying the third equation and introducing the non-dimensional eccentricity factor; n=e/L, gives:

$$4l^3 - (8+6n)l^2 + (4+12n)l - 3n = 0 \tag{5.32}$$

This third-degree equation can be solved when the eccentricity; z, is known. There are three solutions, where only one of the roots is of interest. The reduced horizontal capacity, due to the moment, is given by equation 5.29, where l is given of equation 5.32. This rather complicated expression is difficult to implement, and a simplified empirical formula would be beneficial. It turns out, after several trial functions, that the equation is very similar to the following expression:

$$H_{res} = H_u * (1 - \left(\frac{M}{M_u}\right)^d \tag{5.33}$$

The analytical expression can be plotted against equation 5.33, with different values of d being chosen; 1, 1.5 and 2.

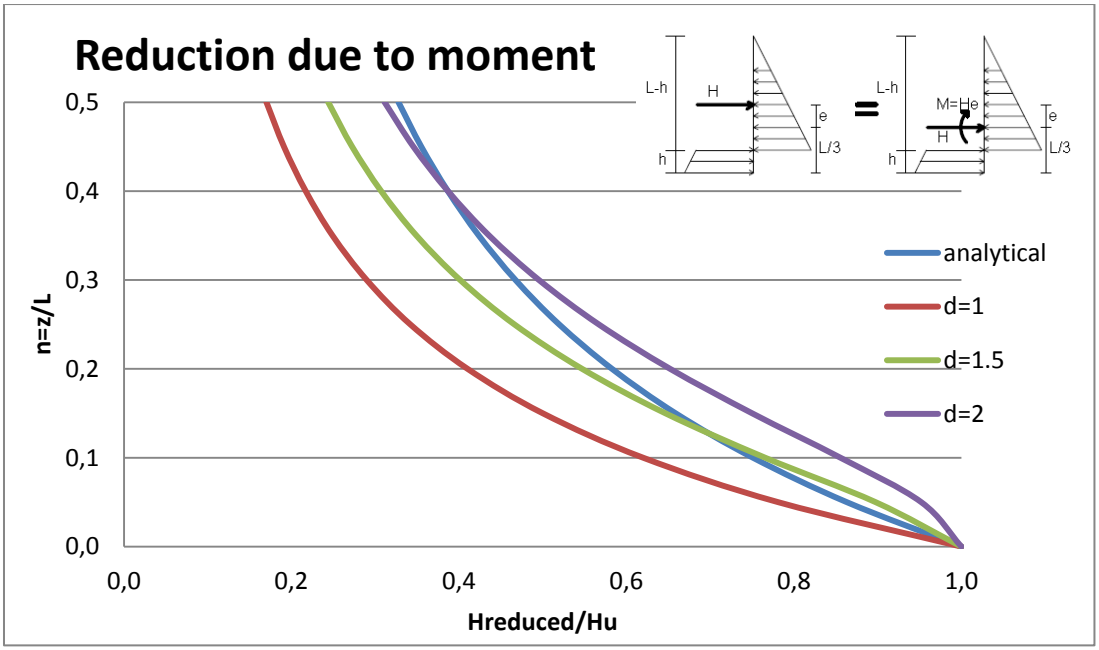

Figure 86 - Reduction due to padeye position

This relation will make the interaction between the force components more physical, and will increase the accuracy.

The moments in the yield surface can be eliminated through equations 4.11-4.13:

$$\left(\frac{H_x}{H_u\left(1-\left(\frac{|H_x * ez - V * ex|}{M_u}\right)^d\right)}\right)^a + \left(\frac{H_y}{H_u\left(1-\left(\frac{H_y * ez}{M_u}\right)^d\right)}\right)^a + \left(\frac{V}{V_u}\right)^b + \left(\frac{H_y * e_z}{T_u}\right)^c = 0$$

(5.34)

The equation can further be presented in terms of P, α and β by applying equations 4.10-4.13:

$$\left(\frac{P * \cos(\alpha) * \cos(\beta)}{H_u\left(1-\left(\frac{P * |e_z * \cos(\alpha) * \cos(\beta) - e_x * \sin(\alpha)|}{M_u}\right)^d\right)}\right)^a + \left(\frac{P * \cos(\alpha) * \sin(\beta)}{H_u\left(1-\left(\frac{P * e_z * \cos(\alpha) * \sin(\beta)}{M_u}\right)^d\right)}\right)^a + \left(\frac{P * \sin}{V_u}\right)^b + \left(\frac{P * e_x * \cos(\alpha) * \sin(\beta)}{T_u}\right)^b = 0$$

(5.35)

This expression will be used in order to determine the magnitude of the force vector for given angles. This can for instance be done by Newton's iterations, see equation 5.20. The yield surface 2 has the following expression:

$$F = \left(\frac{P * \cos(\alpha) * \cos(\beta)}{H_u\left(1 - \left(\frac{P * |e_z * \cos(\alpha) * \cos(\beta) - e_x * \sin(\alpha)|}{M_u}\right)^d\right)}\right)^a + \left(\frac{P * \cos(\alpha) * \sin(\beta)}{H_u\left(1 - \left(\frac{Pe_z \cos(\alpha)\sin(\beta)}{M_u}\right)^d\right)}\right)^a + \left(\frac{P * \sin}{V_u}\right)^b + \left(\frac{Pe_x \cos(\alpha)\sin(\beta)}{T_u}\right)^b - 1 = 0 \quad (5.36)$$

The same error tolerance has been applied for the second yield surface, see equation 5.21. The denominator in the horizontal load part decreases when the moment increases; this will effectively reduce the horizontal capacity. It is seen from Plaxis results that the moment does not significantly reduce the vertical capacity, and it is therefore not included in the equation due to its complexity. However, the vertical capacity in the equation is replaced by the vertical capacity with respect to padeye loading; 15,500kN is replaced by 15,400kN. This means that the vertical loading term indirectly includes the interaction with the bending moment.

The method of least squares is applied in order to obtain the best curve fitting for the empirical coefficients (Kreyszig, 2006). Adjustments are then applied to make the surface slightly more conservative. The following values were obtained:

Coefficient	Value, optimized: accuracy=99.35%	Value, modified: accuracy=99.30%
a	5.5	5
b	4.8	5
c	2.1	2
d	2.0	2

Table 7 - Empirical coefficients

Yield surfaces against Plaxis results

The two different yield surfaces will be compared to the Plaxis results. The yield surfaces will then be discussed briefly.

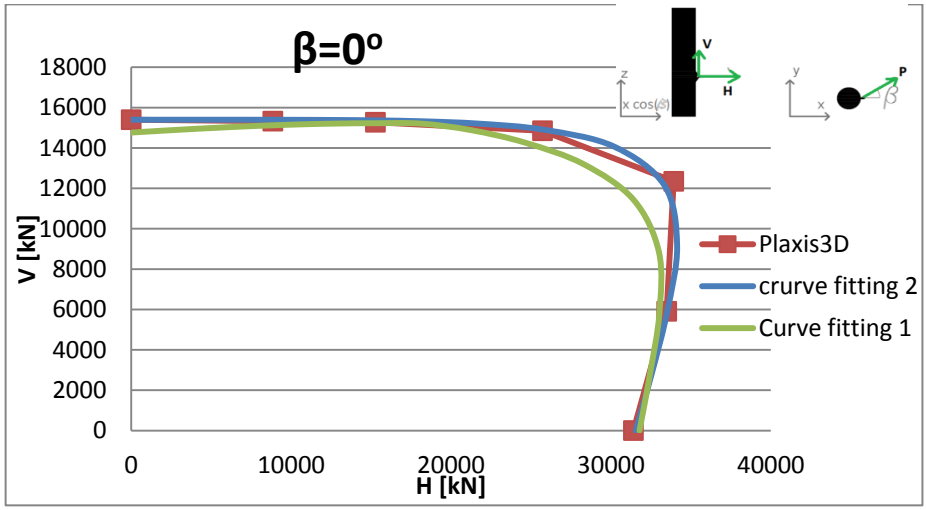

Figure 87 - Yield surfaces, β=0 degrees

Figure 87 shows the results from Plaxis against both empirical formulas when β is 0 degrees. Both empirical yield surfaces intersect most load cases quite well, although the first curve-fitting formula underestimates, in particular, the load case when the inclination angle; α, is 20 degrees. It also has one limitation; when α increases from 60 to 90 degrees, the curve suggests that the vertical capacity will be reduced due to an increasing moment. However, the results from Plaxis suggest that this additional moment has a negligible impact on the vertical capacity.

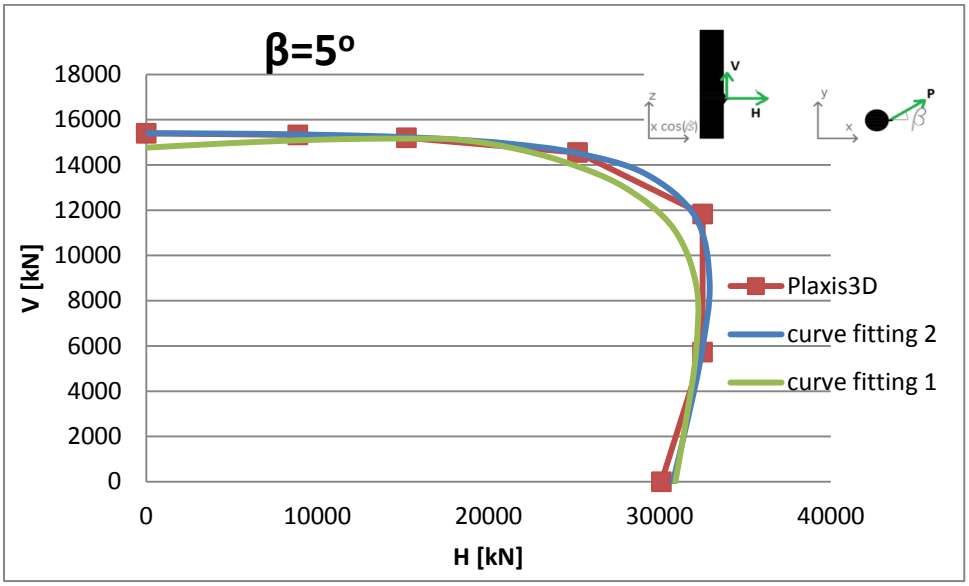

Figure 88 - Yield surfaces, β=5 degrees

Figure 88 shows the yield surfaces when the torsional angle is 5 degrees. Both empirical curves fit well with the Plaxis results, although the second empirical curve fits better. Both curves overestimate the horizontal load case by about 2%.

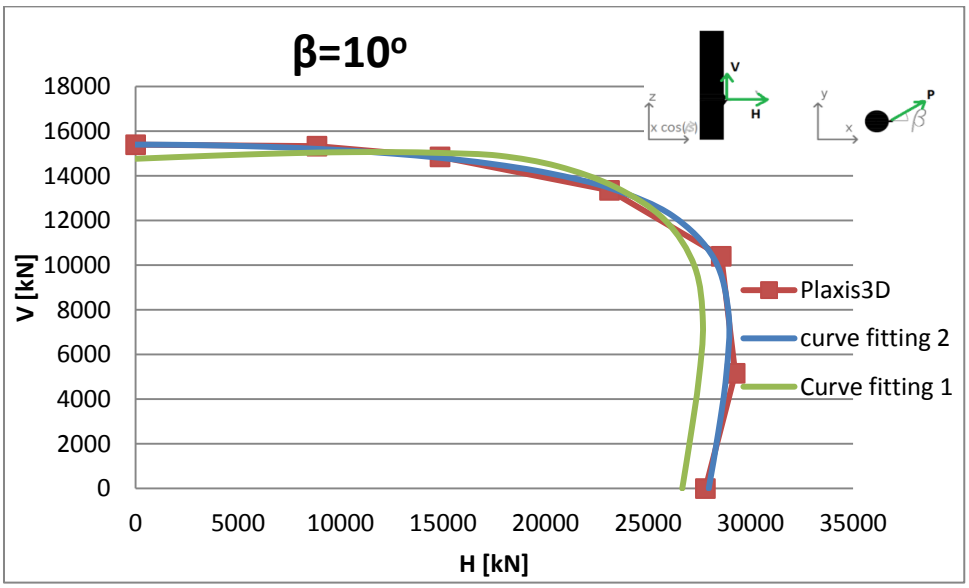

Figure 89 - Yield surfaces, β=10 degrees

Figure 89 shows the yield surfaces when the torsional angle β is 10 degrees. The first empirical curve underestimates the horizontal load cases by a few percent. The second curve has a good curve fit.

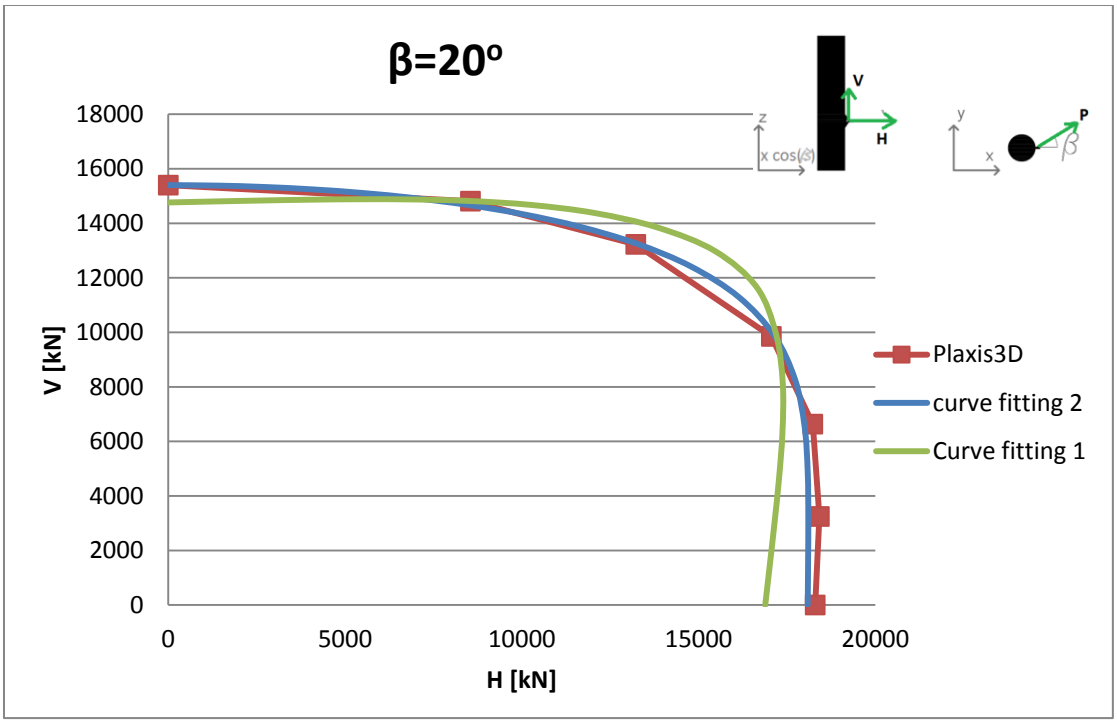

Figure 90 - Yield surfaces, β=20 degrees

Figure 90 shows that the first empirical yield surface does not have the same shape as the Plaxis results, although the second empirical yield surface fits well.

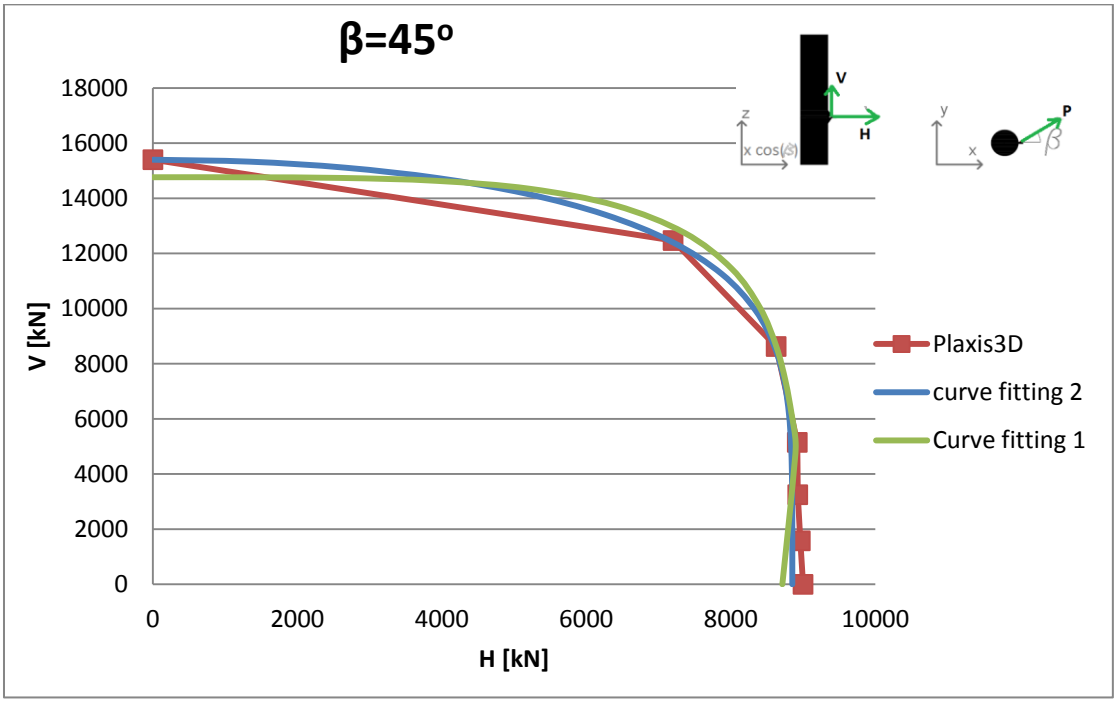

Figure 91 - Yield surfaces, β=45 degrees

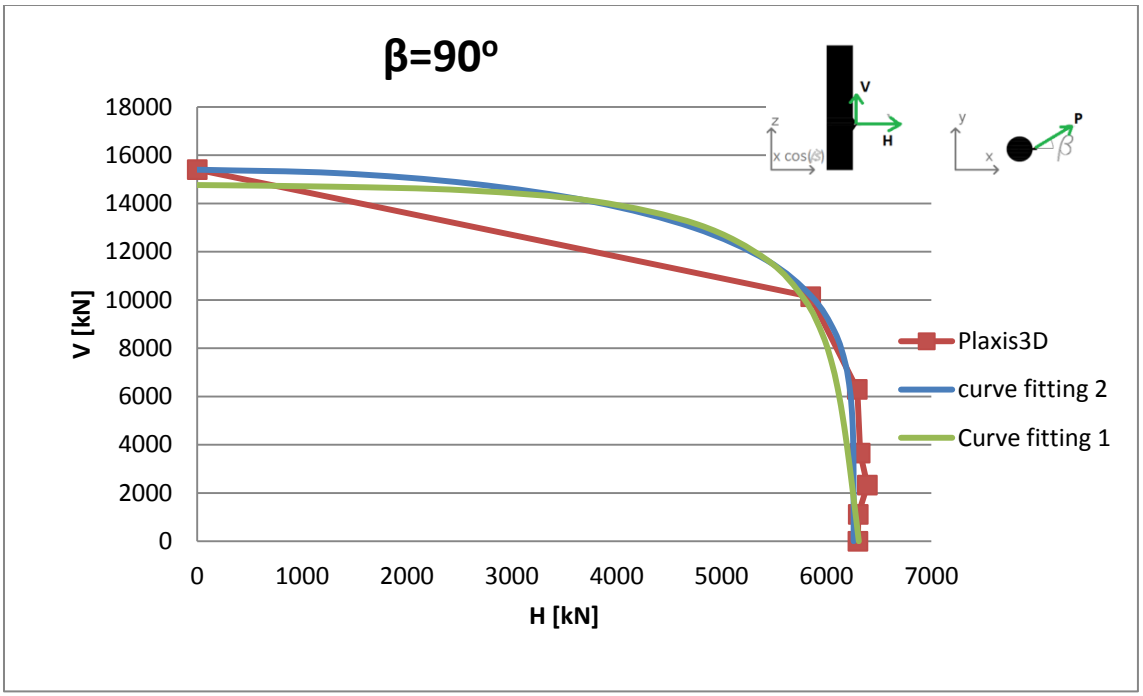

Figure 92 - Yield surfaces, β=90 degrees

Figure 91 and figure 92 show that both curve-fitting surfaces correspond well with the Plaxis results.

It can be concluded that the second curve-fitting yield surface corresponds better with the Plaxis results. This applies to both the shape of the curve and the accuracy for all values of the angle β. From the method of least squares, the average error of the curve fitting caused by the load cases was 0.70%. This means that for an arbitrary load case, the difference between the failure load from Plaxis and the corresponding point from the empirical surface is expected to be 0.70%. In other words, the second curve-fitting formula interpolates the results almost perfectly.

Both empirical formulas consist of four empirical coefficients, although the latter formula is more comprehensive. This is especially prominent due to differentiation, which is required because of Newton's iterations and the implementation of the elasto-plastic formulation due to the flow rule. However, the second curve-fitting formula is definitely not too complicated to implement.

The results from the second yield surface are plotted against the Plaxis results in isolation, to show the accuracy:

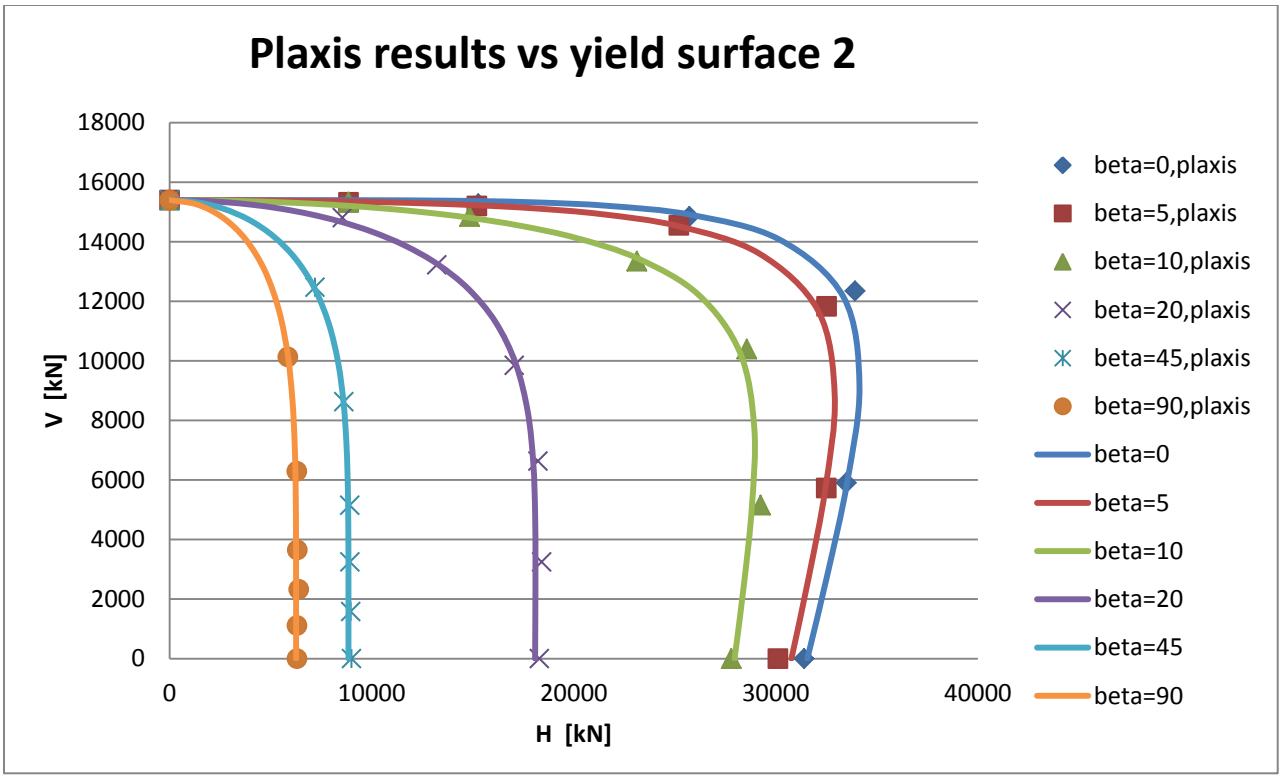

Figure 93 - Plaxis results versus yield surface 2

6 Elasto-plastic formulation

The elasto-plastic formulation will be presented in this chapter. The first section will be devoted to the formulation due to padeye loads and deflections, while the implementation and how to use the formulation will be the focus towards the end of the chapter. The theory applied uses a formulation with respect to stresses and strains. The formulation given in this chapter will be adopted in terms of displacements and loads at the padeye.

6.1 Formulation

Elastic and plastic deformation might take place during a load step. How much the elastic and plastic deformation contribute, and how the mobilization and stiffness change, are described by an elasto-plastic formulation. An elasto-plastic formulation requires several elements (Cook *et. al*, 2001):

- Compatibility
- Stiffness matrix
- Yield criterion
- Flow rule
- Hardening rule

These elements are used to trace the displacements, control yielding and the tangential stiffness of the system. Each element will be dealt with separately. How to put the elements together, is also discussed.

6.1.1 Compatibility

Compatibility simply states that the total displacements are equal to the sum of the elastic and the plastic displacements (Cook *et. al*, 2001):

$$\{du_{tot}\} = \{du_{el}\} + \{du_{pl}\} \tag{6.1}$$

After a load step, the displacement vectors will be updated:

$$\{du_{el}\}_{n+1} = \{u_{el}\}_n + \{du_{el}\}_n \tag{6.2}$$
$$\{du_{pl}\}_{n+1} = \{u_{pl}\}_n + \{du_{pl}\}_n \tag{6.3}$$
$$\{du_{tot}\}_{n+1} = \{u_{tot}\}_n + \{du_{tot}\}_n \tag{6.4}$$

6.1.2 Stiffness and flexibility matrixes

The stiffness and flexibility matrixes are already obtained, see equations 5.15 and 5.16. The flexibility matrix controls the elastic deflections, while the stiffness matrix shows the stiffness behavior of the system. Elastic deflections are governed by the following equation:

$$\{u_{el}\} = \begin{Bmatrix} u_{el,x} \\ u_{el,y} \\ u_{el,z} \end{Bmatrix} = [K]^{-1}\{Q\} = \begin{bmatrix} \frac{1}{21} & 0 & \frac{1}{-200} \\ 0 & \frac{1}{6} & 0 \\ \frac{1}{-200} & 0 & \frac{1}{13} \end{bmatrix} * \begin{Bmatrix} H_x \\ H_y \\ V \end{Bmatrix} * \frac{10^{-4}m}{kN} \tag{6.5}$$

6.1.3 Yield criterion

The yield criterion defines how the system yields. Two different yield formulas have already been presented in section 5.7. When the state parameter f is inserted, the yield criterion is complete. The state parameter has an initial value. If the expression is less than 0 it implies that the plastic criterion is not fulfilled, and only elastic response takes place. Two yield criterions will be presented. The first one has the following expression:

$$F = (\frac{H_x}{f * H_{x,u}})^a + (\frac{H_y}{f * H_{y,u}})^a + (\frac{V}{f * V_u})^b + (\frac{M_x}{f * M_{x,u}})^c + (\frac{M_y}{f * M_{y,u}})^c + (\frac{T}{f * T_u})^d - 1 = 0$$

(6.6)

And the second one is given of:

$$F = (\frac{H_x}{f * H_u\left(1 - \left(\frac{M_y}{f * M_u}\right)^d\right)})^a + (\frac{H_y}{f * H_u\left(1 - \left(\frac{M_x}{f * M_u}\right)^d\right)})^a + (\frac{V}{f * V_u})^b + (\frac{T}{f * T_u})^c - 1 = 0$$

(6.7)

If compression force applied to the padeye also will be present, absolute signs will be needed for each force component, and is thus implemented in the spreadsheet. Eliminating the moments achieved by applying equation 4.11-4.13, which results equation 6.8 and 6.9 for yield surface 1 and 2.

$$F = (\frac{H_x}{fH_u})^a + (\frac{H_y}{fH_u})^a + (\frac{V}{fV_u})^b + (\frac{H_y * e_z}{fM_u})^c + (\frac{|H_x * e_z - V * e_x|}{fM_u})^c + (\frac{H_y * e_x}{fT_u})^d - 1 = 0$$

(6.8)

$$F = (\frac{H_x}{fH_u\left(1 - \left(\frac{|H_x * ez - V * ex|}{fM_u}\right)^d\right)})^a + (\frac{H_y}{fH_u\left(1 - \left(\frac{H_y * ez}{fM_u}\right)^d\right)})^a + (\frac{V}{fV_u})^b + (\frac{H_y * e_z}{fT_u})^c - 1 = 0$$

(6.9)

6.1.4 Flow rule

An associated flow rule is used:

$$d\bar{u}_p = d\lambda\left\{\frac{\partial F}{\partial Q}\right\} = d\lambda\begin{Bmatrix}\frac{\partial F}{\partial H_x}\\ \frac{\partial F}{\partial H_y}\\ \frac{\partial F}{\partial V}\end{Bmatrix} \quad (6.10)$$

where du_P is the incremental plastic displacement vector
$d\lambda$ is a plastic multiplier
the latter term is the gradient to the yield surface, and is normal to the yield surface

The flow rule implies that the plastic displacement vector will be normal to the yield surface. The gradient of yield criterion number is given of equation 6.11, while the gradient for yield surface 2 is given of equation 6.12.

$$\begin{Bmatrix} \frac{\partial F}{\partial H_x} \\ \frac{\partial F}{\partial H_y} \\ \frac{\partial F}{\partial V} \end{Bmatrix} = \begin{Bmatrix} \frac{a}{f*H_u}\left(\frac{H_x}{f*H_u}\right)^{a-1} + \frac{c*ez}{f*M_u}\left(\frac{|H_x*ez - V*ex|}{f*M_u}\right)^{e-1} \\ \frac{a}{f*H_u}\left(\frac{H_y}{f*H_u}\right)^{a-1} + \frac{c*ez}{f*M_u}\left(\frac{H_y*ez}{f*M_u}\right)^{c-1} + \frac{d*ex}{f*T_u}\left(\frac{H_y*ex}{f*T_u}\right)^{d-1} \\ \frac{b}{f*V_u}\left(\frac{V}{f*V_u}\right)^{b-1} - \frac{c*ex}{f*M_u}\left(\frac{|H_x*ez - V*ex|}{f*M_u}\right)^{e-1} \end{Bmatrix} \quad (6.11)$$

$$\frac{\partial F}{\partial H_x} = \frac{a}{fH_u}\left(\frac{H_x}{fH_u\left(\frac{|H_x*ez - V*ex|}{f*M_u}\right)^d}\right)^{a-1}\left[\frac{1}{\left(1-\left(\frac{|H_x*ez - V*ex|}{fM_u}\right)^d\right)} + \frac{d*ez}{fM_u}\frac{\left(\frac{|H_xez - Vex|}{f*M_u}\right)^{d-1}}{\left(1-\left(\frac{|H_xez - Vex|}{fM_u}\right)^d\right)^2}\right]$$

$$\frac{\partial F}{\partial H_y} = \frac{a}{fH_u}\left(\frac{H_y}{f*H_u\left(\frac{H_y*ez}{f*M_u}\right)^d}\right)^{a-1}\left[\frac{1}{\left(1-\left(\frac{H_y*ez}{f*M_u}\right)^d\right)} + \frac{d*ez}{f*M_u}\frac{\left(\frac{|H_x*ez - V*ex|}{f*M_u}\right)^{d-1}}{\left(1-\left(\frac{H_y*ez}{f*M_u}\right)^d\right)^2}\right] + \frac{c*ex}{f*T_u}$$

$$\frac{\partial F}{\partial V} = \frac{b}{fV_u}\left(\frac{V}{f*V_u}\right)^{b-1} - \frac{a*d*H_xex}{f^2H_uM_u}\left(\frac{H_x}{fH_u\left(\frac{|H_x*ez - V*ex|}{f*M_u}\right)^d}\right)^{a-1} * \frac{\left(\frac{|H_x*ez - V*ex|}{f*M_u}\right)^{d-1}}{\left(1-\left(\frac{|H_xez - Vex|}{f*M_u}\right)^d\right)^2}$$

(6.12)

6.1.5 Hardening rule

The hardening rule describes how the system plasticizes. The hardening rule is obtained by curve fitting to the test data. The curve-fitting formula can, for instance, result from a power law or a hyperbola. The power law is obtained from equation 6.13 while the hyperbola is obtained from equation 6.14 (Nordal, 2010).

$$f(\bar{u}_p) = f_0 + k_1 * \bar{u}_p{}^{1/k_2} \quad (6.13)$$

$$f(\bar{u}_p) = f_0 + \frac{\bar{u}_p}{b + a*u_p} \quad (6.14)$$

where f_0 is the initial value of the state parameter, taken as 0.6
a, b, k_1, k_2 are empirical hardening coefficients
$\bar{u}_p$ is the plastic displacement measure

Displacement hardening is assumed for the thesis (strain hardening applied on displacements). The hardening laws are used in combination with a hardening criterion, which can, for instance, be an isotropic, a kinematic or a mixed hardening criterion. Although isotropic hardening might not be the best suited criterion for this particular system, it is still chosen, due to its simplicity and the fact that a compression force will not be expected, since the forces are applied to the padeye through a mooring chain that cannot carry significant tension.

In order to isolate the plastic displacements from a load case, the relation of equation 6.15 is applied

$$\bar{u}_p = \sqrt{\{u_{pl}\}^T\{u_{pl}\}} = \sqrt{\{u_{tot} - u_{el}\}^T\{u_{tot} - u_{el}\}}$$

$$= \sqrt{(u_{tot,x} - u_{el,x})^2 + (u_{tot,y} - u_{el,y})^2 + (u_{tot,z} - u_{el,z})^2} \qquad (6.15)$$

The elastic displacements are measured from equation 6.5. Plastic curve fitting has been applied for three load cases; loading in the x-, y- and z-directions. Both hyperbola and power law have been applied. The optimization has been achieved by the method of least squares. Firstly, the optimization has been done with respect to the specific load case. Then, a common optimization for all three load cases was applied. Voce rule was also tested, but did not give appropriate results. Results from the three different load cases were as follows:

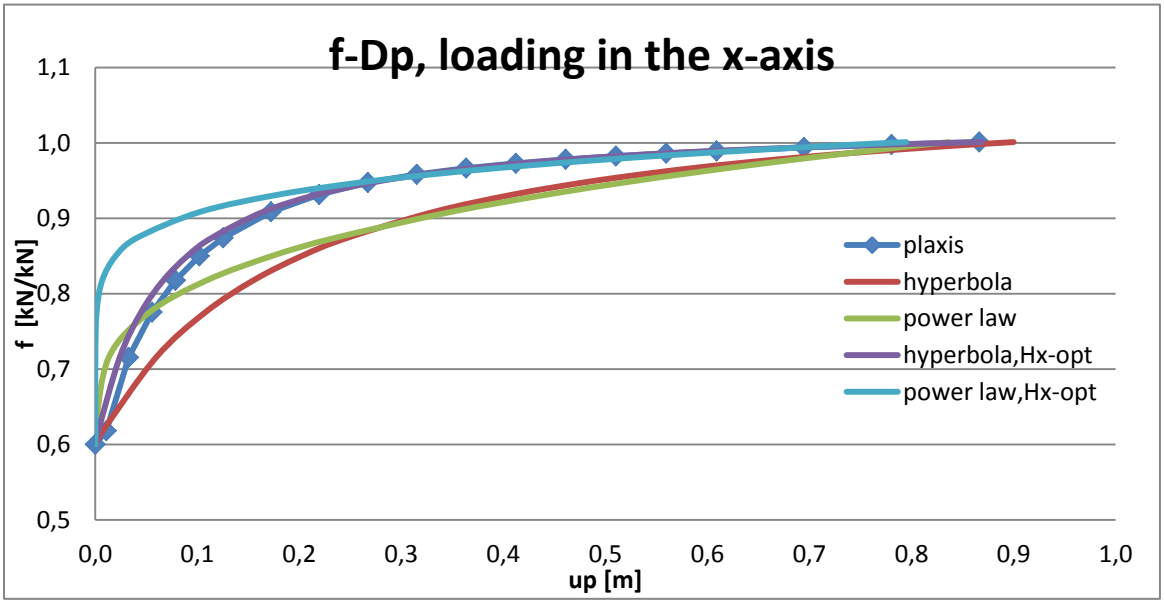

Figure 94 - Empirical curve fitting for hardening; loading in the x-direction

Figure 94 plots the plastic load against the mobilization factor f, for loading in the x-direction. It is noted that the power law does not offer a good fit with the Plaxis results. It is also observed that the optimization for this load case gave a good fit for the hyperbola.

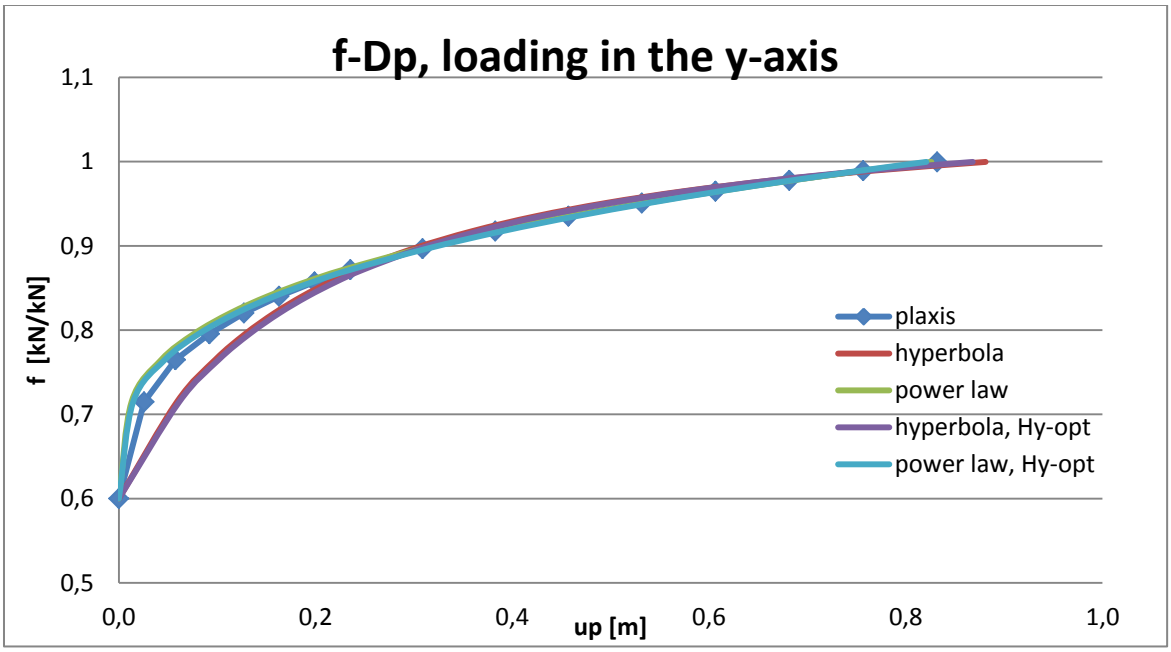

Figure 95 - Empirical curve fitting for hardening; loading in the y-direction

Figure 95 plots the plastic load against the mobilization factor f, for loading in the y-direction. The empirical curves correspond well with the Plaxis results.

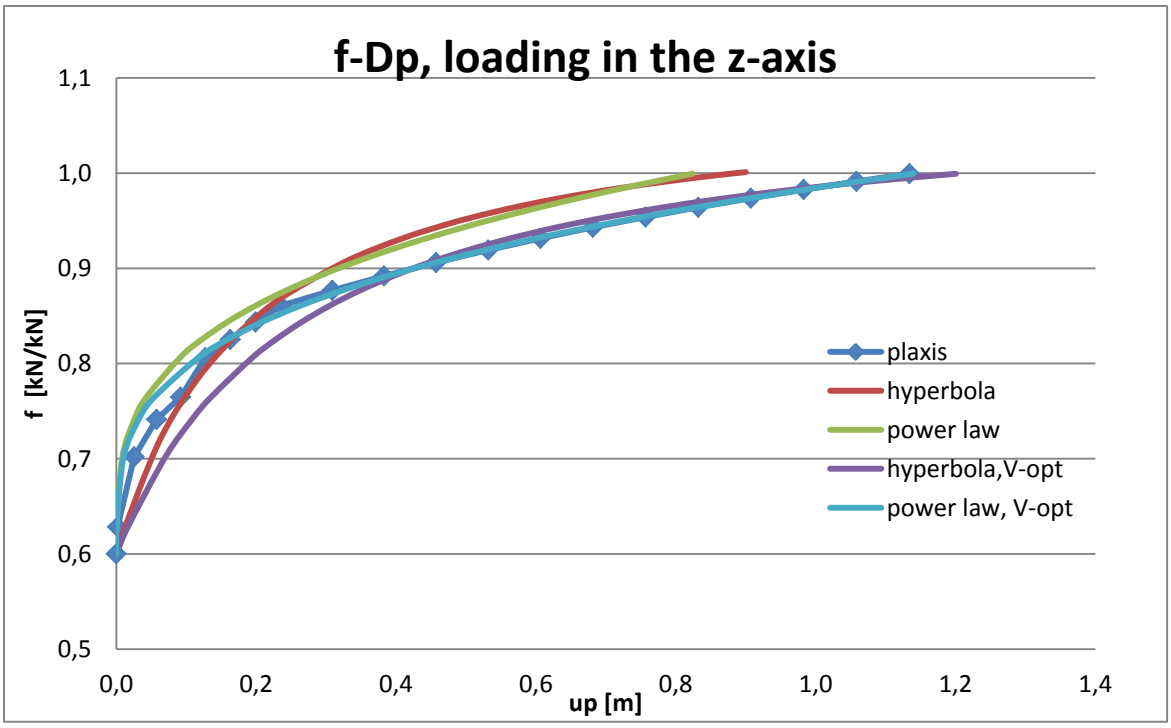

Figure 96 - Empirical curve fitting for hardening; loading in the z-direction

Figure 96 plots the plastic load against the mobilization factor f, for loading in the z-direction. The curve fitting optimized on the basis of vertical loading interpolates the Plaxis results well, and the empirical curves optimized for all the three load cases correspond adequately.

Based on the three load cases, it can be concluded that the hyperbola is the best function for this problem. When each load case is optimized separately, the accuracy increases, although the hyperbola optimized on the basis of the three load cases also delivers quite good results. The following coefficients were obtained after the method of least squares was applied:

Optimization	a	b
All load cases	2.056	0.393
x-direction	2.318	0.152
y-direction	2.051	0.544
z-direction	2.030	0.410

Figure 97 - Empirical coefficient values hyperbola

Anisotropic hardening properties have now been demonstrated. The anisotropy can be implemented by interpolation, although it will increase the complexity of the formulation. One possible interpolation function is the following:

$$\begin{Bmatrix} a(Q) \\ b(Q) \end{Bmatrix} = \begin{bmatrix} a_x & a_y & a_z \\ b_x & b_y & b_z \end{bmatrix} \begin{Bmatrix} H_x \\ H_y \\ V \end{Bmatrix} / \sqrt{\{Q\}^T \{Q\}} \tag{6.16}$$

However, it will in the following be shown that the interpolation actually delivers less accurate results for a chosen load case, where α=30 degrees and β=10 degrees:

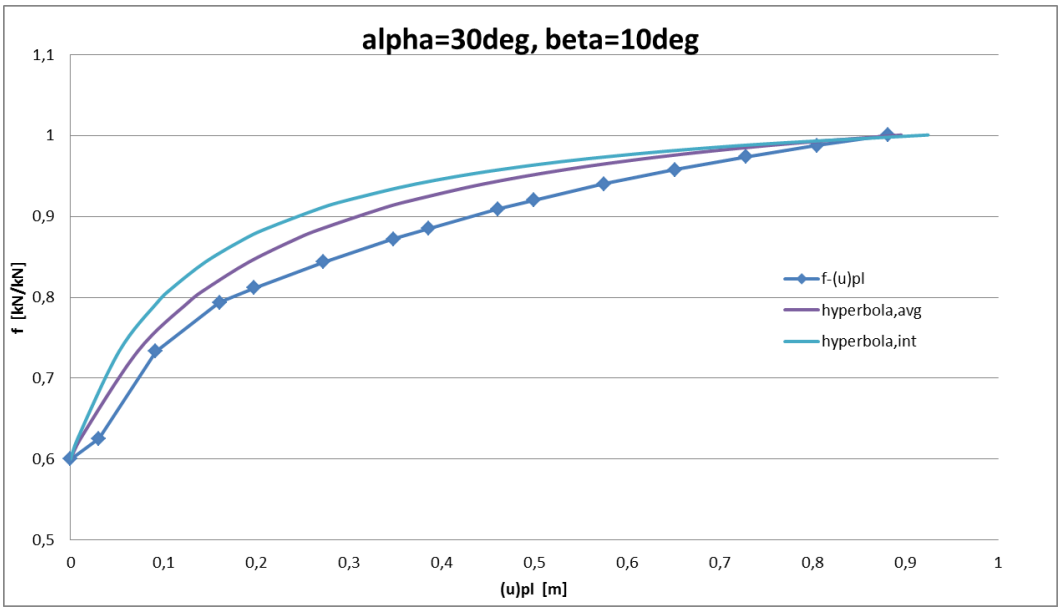

Figure 98 - Hardening curve, α=30 degrees, β=10 degrees; interpolated and optimized based on three LC, hyperbola

A modified weighted interpolation function is thus needed, if interpolation is considered being used. The following equation is chosen:

$$\begin{Bmatrix} a(Q) \\ b(Q) \end{Bmatrix} = \frac{\begin{bmatrix} a_x & a_y & a_z \\ b_x & b_y & b_z \end{bmatrix} \begin{Bmatrix} \zeta_x H_x \\ \zeta_y H_y \\ \zeta_z V \end{Bmatrix}}{\sqrt{\begin{Bmatrix} \zeta_x H_x \\ \zeta_y H_y \\ \zeta_z V \end{Bmatrix}^T \begin{Bmatrix} \zeta_x H_x \\ \zeta_y H_y \\ \zeta_z V \end{Bmatrix}}} \tag{6.17}$$

where $\zeta_x, \zeta_y, \zeta_z$ are empirical coefficients that weigh the impact of load direction

The weighting coefficients are then determined from the same load case; α=30 degrees, β=10 degrees. The method of least squares gave the values ζ_x=0, ζ_y=2.03 and ζ_z=0.99, respectively. This implies that the empirical hardening behavior in the x-direction is disregarded, which would not be favorable. The weighting coefficients gave the following hardening behavior:

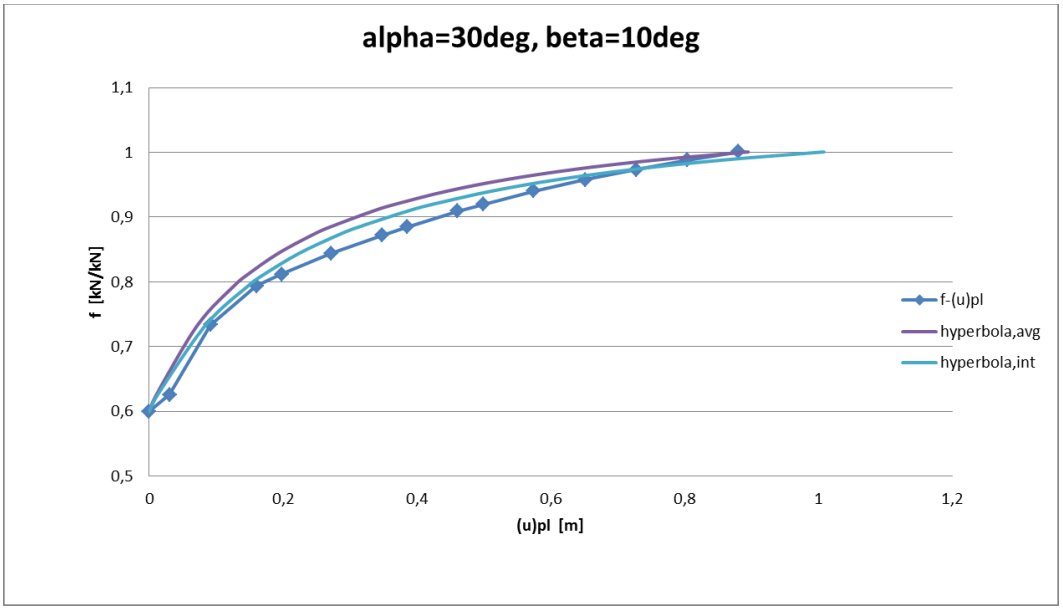

Figure 99 - Hardening curve, α=30 degrees, β=10 degrees; weighted interpolation and optimized based on three LC

It is seen that the increase in accuracy is not significant, and that the initial hardening model actually provides proper results. The initial hardening response, which was obtained by optimization of the three orthogonal load cases, will for that reason be applied.

6.1.6 Putting it all together

The pieces have now been presented, and it remains to put the puzzle together. The procedure is done accorded to Nordal (2010). Firstly, it is solved for the plastic resistance:

$$A = -\frac{\partial F}{\partial f}\frac{df}{dD_p}\frac{dD_p}{d\lambda} \tag{6.18}$$

The first term in the equation is the derivative of the yield surface with respect to the state parameter; f, the second term is obtained from curve fitting as shown, while the third term gives a relation between the plastic displacements and the plastic multiplier.

The first term will be as follows for the first yield surface:

$$\frac{\partial F}{\partial f} = -\frac{1}{f}\left[a\left(\frac{H_x}{f * H_u}\right)^{a-1} + \left(\frac{H_y}{f * H_u}\right)^{a-1}\right]$$

$$+\left(\frac{V}{f * V_u}\right)^{b-1} + \left(\frac{H_x * ez}{f * M_u}\right)^{c-1} + \left(\frac{|H_x * ez - V * ex|}{f * M_u}\right)^{c-1} + \left(\frac{H_y * ex}{f * T_u}\right)^{d-1} \quad (6.19)$$

The third term is the plastic resistance equation, given as:

$$\frac{dD_p}{d\lambda} = \sqrt{\left\{\frac{\partial F}{\partial Q}\right\}^T * \left\{\frac{\partial F}{\partial Q}\right\}} \quad (6.20)$$

Then it is solved for the plastic parameter:

$$d\lambda = \frac{1}{A}\left\{\frac{\partial F}{\partial Q}\right\}^T \{dQ\} \quad (6.21)$$

Thereafter, it is solved for the plastic deformation:

$$\{dD_p\} = \frac{1}{A}\left\{\frac{\partial F}{\partial Q}\right\}^T \{dQ\}\left\{\frac{dF}{dQ}\right\} \quad (6.22)$$

The tangential stiffness matrix of the system can be solved by the following formula:

$$\left[K_{ep}\right] = [K] - \frac{[K]\left\{\frac{dF}{dQ}\right\}\left\{\frac{\partial F}{\partial Q}\right\}^T [K]}{A + \left\{\frac{\partial F}{\partial Q}\right\}^T [K]\left\{\frac{dF}{dQ}\right\}} \quad (6.23)$$

And finally, the displacement vector can be updated:

$$\{du_{tot}\} = \{du_{el}\} + \{du_{pl}\} \quad (6.24)$$

The displacements will then be as follows after load step n:

$$\{du_{el}\}_{n+1} = \{u_{el}\}_n + \{du_{el}\}_n \quad (6.25)$$

$$\{du_{pl}\}_{n+1} = \{u_{pl}\}_n + \{du_{pl}\}_n \quad (6.26)$$

$$\{du_{tot}\}_{n+1} = \{u_{tot}\}_n + \{du_{tot}\}_n \quad (6.27)$$

6.2 Implementation

This section describes how the elasto-plasticity has been implemented. A spreadsheet has been developed in Excel, applying the formulas already presented. However, the method uses load control, rather than displacement control. Firstly, the solution steps used in the spreadsheet will be presented. Thereafter, a simple demonstration will show how the model works.

6.2.1 Solution steps

The theory has been presented, and it is time for solving the system of equations (the equations in this section will not be numbered, but listed in steps). The following procedure has been used:

1. Choose an arbitrary load vector. If the force components are H_X, H_Y and V, the force vectors will be as follows:

$$\{\Delta Q_n\} = \begin{Bmatrix} \Delta H_{X,n} \\ \Delta H_{Y,n} \\ \Delta V_n \end{Bmatrix} \tag{6.28}$$

$$\{Q\}_{n+1} = \{Q\}_n + \{\Delta Q\}_{n+1} = \begin{Bmatrix} H_X \\ H_Y \\ V \end{Bmatrix}_n + \begin{Bmatrix} \Delta H_{X,n} \\ \Delta H_{Y,n} \\ \Delta V_n \end{Bmatrix}_{n+1} \tag{6.29}$$

   The load-step vector and the total load vector will the same for the first load step.

2. Divide the load-step vector into a large number of smaller incremental load vectors. Each load step is divided into m=100 load increments.

$$\{dQ\}_l = \frac{1}{m}\{\Delta Q\}_n\,, \qquad l = [1, m] \qquad \{Q\}_{n+l+1} = \{Q\}_{n+l} + \{dQ\}_{n+l+1} \tag{6.30}$$

3. Calculate the incremental elastic deformations caused by the incremental load vector.

$$\{du_{el}\}_{n+l+1} = [K]^{-1} * \{dQ\}_{n+l+1} \tag{6.31}$$

4. Calculate the mobilization factor of the system and the corresponding state parameter, which expresses how mobilized the soil is. The mobilization factor is obtained by solving the equation F(f*)=0, where F is the yield criterion and f* is the mobilization factor. Note that the yield criterion is only depended on f*, since finite values for the force components are already substituted into the equation. The equation is solved by Newton's iterations:

$$f^*_{n+l+1} = f^*_n - \frac{F(f^*_{n+l})}{F'(f^*_{n+l})} \tag{6.32}$$

   It is important to perform sufficient iterations to ensure convergence of the yield surface. The following error tolerance has been applied:

$$error = \left|1 - \frac{f^*_{n+l+1}}{f^*_{n+l}}\right| < 10^{-5} \tag{6.33}$$

   The following conditions express the yields for the corresponding state parameters:

$$f^*_{n+l+1} = F(\{Q\}_{n+l+1}) \quad (6.34)$$

$$f_{n+l+1} = max\begin{Bmatrix} f_{n+l} \\ f^*_{n+l+1} \end{Bmatrix} \quad (6.35)$$

Note that the state parameter; f, cannot decrease; only increase.

5. Calculate the accumulated incremental plastic displacement measure.

$$\begin{aligned} &if && f_{n+l+1} = f_{n+l}\,; \;\; d\bar{u}_{pl,n+l} = 0 \\ &otherwise && d\bar{u}_{p,n+l+1} = \bar{u}_p(f_{n+l+1}) - \bar{u}_{p,n+l} \end{aligned} \quad (6.36)$$

6. Calculate the plastic scalar; dλ.

$$\mathrm{d}\lambda_{n+l+1} = \frac{d\bar{u}_{p,n+l+1}}{\sqrt{\left\{\frac{\partial F}{\partial Q_{n+l+1}}\right\}^T \left\{\frac{\partial F}{\partial Q_{n+l+1}}\right\}}} \quad (6.37)$$

7. Calculate the incremental plastic displacement vector. The trapezoidal rule is applied to increase the accuracy.

$$\{du_{pl}\}_{n+l+1} = \frac{1}{2}(\mathrm{d}\lambda_{n+l+1} + \mathrm{d}\lambda_{n+l}) * \left\{\frac{\partial F}{\partial Q_{n+l}}\right\} \quad (6.38)$$

8. Update the displacement vectors.

$$\{u_{el}\}_{n+l} = \{u_{el}\}_{n+l-1} + \{du_{el}\}_{n+l} \quad (6.39)$$

$$\{u_{pl}\}_{n+l} = \{u_{pl}\}_{n+l-1} + \{du_{pl}\}_{n+l} \quad (6.40)$$

$$\{u\}_{n+l} = \{u_{el}\}_{n+l} + \{u_{pl}\}_{n+l} \quad (6.41)$$

9. Repeat the process until l = m, and a new load step can be applied.

The process applies load control rather than displacement control, which is usual practice for elasto-plasticity due to stress-strain relations. The elasto-plastic stiffness matrix is not needed, but might be calculated if desired.

6.2.2 Elasto-plastic spreadsheet

The spreadsheet was implemented in Excel. The properties of the spreadsheet will be explained in the following. First of all, the properties obtained have to be specified. All the values can easily be changed, for instance if used with other projects.

Input, coefficients:	
Type	Value
fo []	0.6
a []	5.0
b []	5.0
c []	2.0
d []	2.0
Hu [kN]	38,000
Vu [kN]	15,400
Mu [kNm]	230,000
Tu [kNm]	23,800
ex [m]	3.75
ez [m]	3
k1 []	2.056
k2 []	0.393

Table 8 - Input parameters

The stiffness matrix were also given as input. The load history also needs to be specified. Up to 10 load steps can be included in the model, with each step being divided into 100 load increments.

Load step	dHx	dHy	dV
1	30,000	0	0
2	-30,000	0	0
3	-30,000	0	0
4	30,000	0	10,000
5	3,000	0	-10,000
6	0	0	0
7	0	0	15,000
8	0	0	-15,000
9	0	6,000	0
10	1,000	-1,000	1,000
Total	4,000	5,000	1,000

Table 9 - Load history

The model continuously calculates the response due to the solution steps explained in the previous section. The second yield surface was chosen, since the yield surface provided remarkably accurate results.

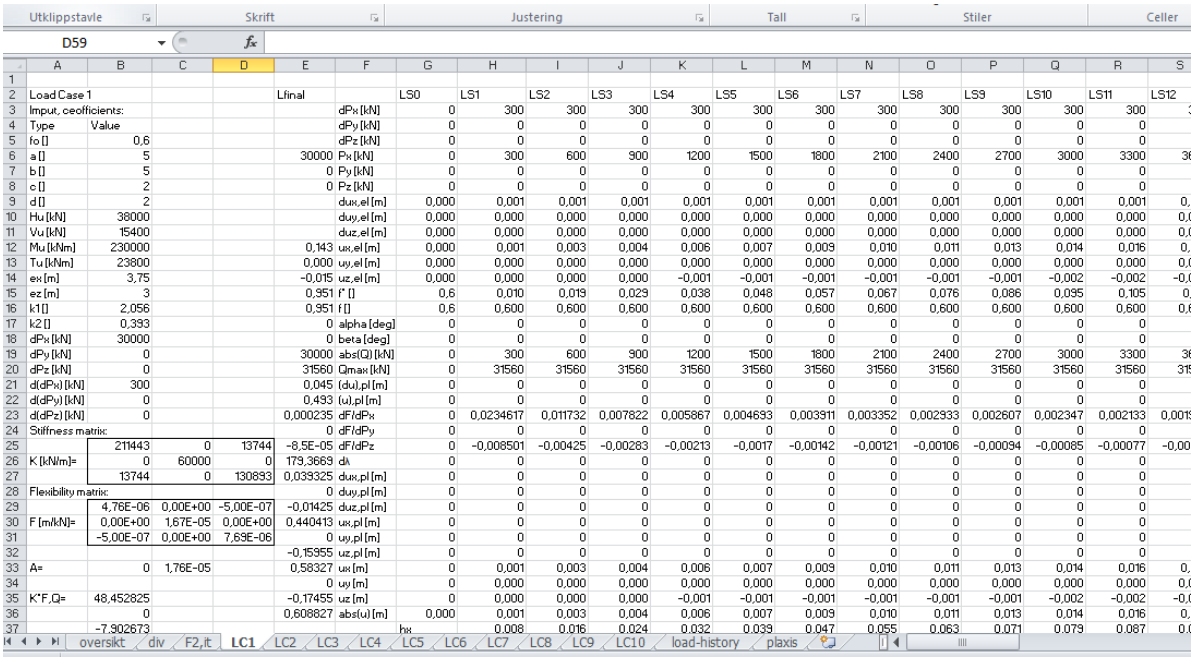

Load Case 1				Lfinal		LS0	LS1	LS2	LS3	LS4	LS5	LS6	LS7	LS8	LS9	LS10	LS11	LS12
Imput, ceoficients:					dPx [kN]	0	300	300	300	300	300	300	300	300	300	300	300	
Type	Value				dPy [kN]	0	0	0	0	0	0	0	0	0	0	0	0	
fo []	0,6				dPz [kN]	0	0	0	0	0	0	0	0	0	0	0	0	
a []	5			30000	Px [kN]	0	300	600	900	1200	1500	1800	2100	2400	2700	3000	3300	3
b []	5			0	Py [kN]	0	0	0	0	0	0	0	0	0	0	0	0	
c []	2			0	Pz [kN]	0	0	0	0	0	0	0	0	0	0	0	0	
d []	2				dux,el [m]	0,000	0,001	0,001	0,001	0,001	0,001	0,001	0,001	0,001	0,001	0,001	0,001	0,
Hu [kN]	38000				duy,el [m]	0,000	0,000	0,000	0,000	0,000	0,000	0,000	0,000	0,000	0,000	0,000	0,000	0,(
Vu [kN]	15400				duz,el [m]	0,000	0,000	0,000	0,000	0,000	0,000	0,000	0,000	0,000	0,000	0,000	0,000	0,(
Mu [kNm]	230000			0,143	ux,el [m]	0,000	0,001	0,003	0,004	0,006	0,007	0,009	0,010	0,011	0,013	0,014	0,016	0,
Tu [kNm]	23800			0,000	uy,el [m]	0,000	0,000	0,000	0,000	0,000	0,000	0,000	0,000	0,000	0,000	0,000	0,000	0,(
ex [m]	3,75			-0,015	uz,el [m]	0,000	0,000	0,000	0,000	-0,001	-0,001	-0,001	-0,001	-0,001	-0,001	-0,002	-0,002	-0,(
ez [m]	3			0,951	f* []	0,6	0,010	0,019	0,029	0,038	0,048	0,057	0,067	0,076	0,086	0,095	0,105	0,
k1 []	2,056			0,951	f []	0,6	0,600	0,600	0,600	0,600	0,600	0,600	0,600	0,600	0,600	0,600	0,600	0,(
k2 []	0,393			0	alpha [deg]	0	0	0	0	0	0	0	0	0	0	0	0	
dPx [kN]	30000			0	beta [deg]	0	0	0	0	0	0	0	0	0	0	0	0	
dPy [kN]	0			30000	abs(Q) [kN]	0	300	600	900	1200	1500	1800	2100	2400	2700	3000	3300	3
dPz [kN]	0			31560	Qmax [kN]	0	31560	31560	31560	31560	31560	31560	31560	31560	31560	31560	31560	31
d(dPx) [kN]	300			0,045	(du),pl [m]	0	0	0	0	0	0	0	0	0	0	0	0	
d(dPy) [kN]	0			0,493	(u),pl [m]	0	0	0	0	0	0	0	0	0	0	0	0	
d(dPz) [kN]	0			0,000235	dF/dPx	0	0,0234617	0,011732	0,007822	0,005867	0,004693	0,003911	0,003352	0,002933	0,002607	0,002347	0,002133	0,001
Stiffness matrix:				0	dF/dPy	0	0	0	0	0	0	0	0	0	0	0	0	
	211443	0	13744	-8,5E-05	dF/dPz	0	-0,008501	-0,00425	-0,00283	-0,00213	-0,0017	-0,00142	-0,00121	-0,00106	-0,00094	-0,00085	-0,00077	-0,00
K [kN/m]=	0	60000	0	179,3669	dλ	0	0	0	0	0	0	0	0	0	0	0	0	
	13744	0	130893	0,039325	dux,pl [m]	0	0	0	0	0	0	0	0	0	0	0	0	
Flexibility matrix:				0	duy,pl [m]	0	0	0	0	0	0	0	0	0	0	0	0	
	4,76E-06	0,00E+00	-5,00E-07	-0,01425	duz,pl [m]	0	0	0	0	0	0	0	0	0	0	0	0	
F [m/kN]=	0,00E+00	1,67E-05	0,00E+00	0,440413	ux,pl [m]	0	0	0	0	0	0	0	0	0	0	0	0	
	-5,00E-07	0,00E+00	7,69E-06	0	uy,pl [m]	0	0	0	0	0	0	0	0	0	0	0	0	
				-0,15955	uz,pl [m]	0	0	0	0	0	0	0	0	0	0	0	0	
A=	0	1,76E-05		0,58327	ux [m]	0	0,001	0,003	0,004	0,006	0,007	0,009	0,010	0,011	0,013	0,014	0,016	0,
				0	uy [m]	0	0,000	0,000	0,000	0,000	0,000	0,000	0,000	0,000	0,000	0,000	0,000	0,(
K*F,Q=	48,452825			-0,17455	uz [m]	0	0,000	0,000	0,000	-0,001	-0,001	-0,001	-0,001	-0,001	-0,001	-0,002	-0,002	-0,(
	0			0,608827	abs(u) [m]	0,000	0,001	0,003	0,004	0,006	0,007	0,009	0,010	0,011	0,013	0,014	0,016	0,
	-7,902673				hx		0,008	0,016	0,024	0,032	0,039	0,047	0,055	0,063	0,071	0,079	0,087	0,(

Table 10 - Calculation process for Load Step 1, which is further divided into 100 smaller increments

The output from the different load steps is summarized in order to interpret the data. Only the output from the five first load cases is shown.

Output	Final	Load Step 1	Load Step 2	Load Step 3	Load Step 4	Load Step 5
f* []		0.951	0.001	0.951	0.649	0.095
f []	0.974	0.951	0.951	0.951	0.951	0.951
alpha [deg]	8.88	0	0	0	90	0
beta [deg]	51.34	0	0	0	0	0
abs(Q) [kN]	6,481	30,000	0	30,000	10,000	3,000
Qmax [kN]	6,654	31,560	0	31,560	15,400	31,560
(u)pl [mm]	636.329	493.3	493.3	493.3	493.3	493.3
ux,el [mm]	18.5	142.9	0.0	-142.9	-5.0	14.3
uy,el [mm]	83.3	0.0	0.0	0.0	0.0	0.0
uz,el [mm]	5.7	-15.0	0.0	15.0	76.9	-1.5
ux,pl [mm]	440.4	440.4	440.4	440.4	440.4	440.4
uy,pl [mm]	0.0	0.0	0.0	0.0	0.0	0.0
uz,pl [mm]	-50.0	-159.5	-159.5	-159.5	-159.5	-159.5
ux [mm]	459.0	583.3	440.4	297.6	435.4	454.7
uy [mm]	83.3	0.0	0.0	0.0	0.0	0.0
uz [mm]	-44.3	-174.5	-159.5	-144.5	-82.6	-161.0
abs(u)[mm]	468.6	608.8	468.4	330.8	443.2	482.4

Table 11 - Output data

The data in the spreadsheet are also plotted in load-deflection diagrams where the response is automatically showed.

6.3 Elasto-plastic response

The following sections will cover the elasto-plastic behavior of the model compared to the response obtained by Plaxis analyses.

6.3.1 Response against Plaxis results

The spreadsheet has been presented, and it is time to show how the empirical results correspond to the numerical results. The load-deflection curves where the torsional angle β is 0 and 10 degrees, except for the vertical load case, are as follows:

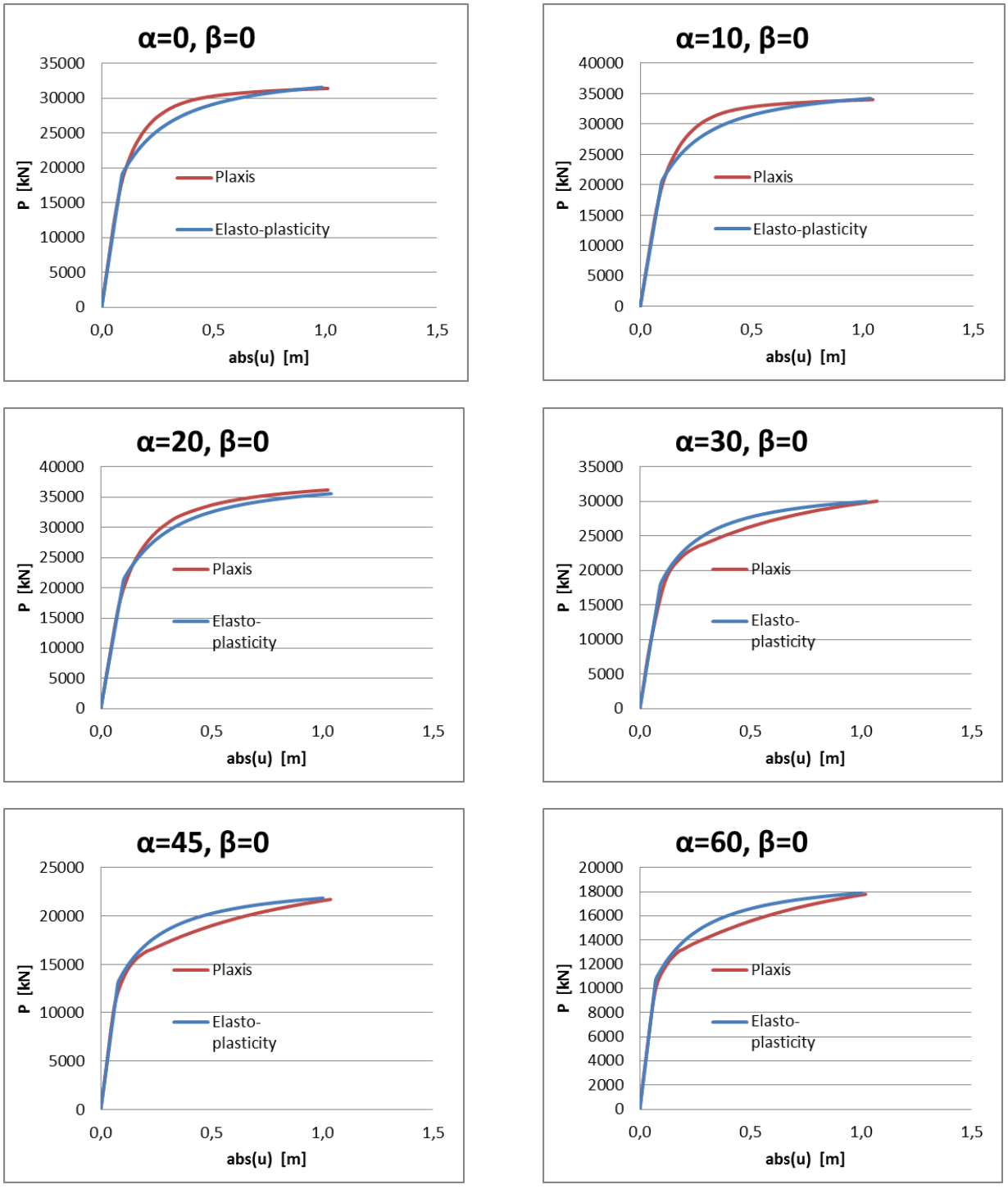

Figure 100 - Elasto-plastic response; Plaxis and empirical results, β=0 degrees

Figure 100 shows the elasto-plastic behavior from Plaxis curves and empirical curves when the torsional angle is 0 degrees. It is observed that the best curve fitting is obtained when the inclination angle is between 20 and 30 degrees.

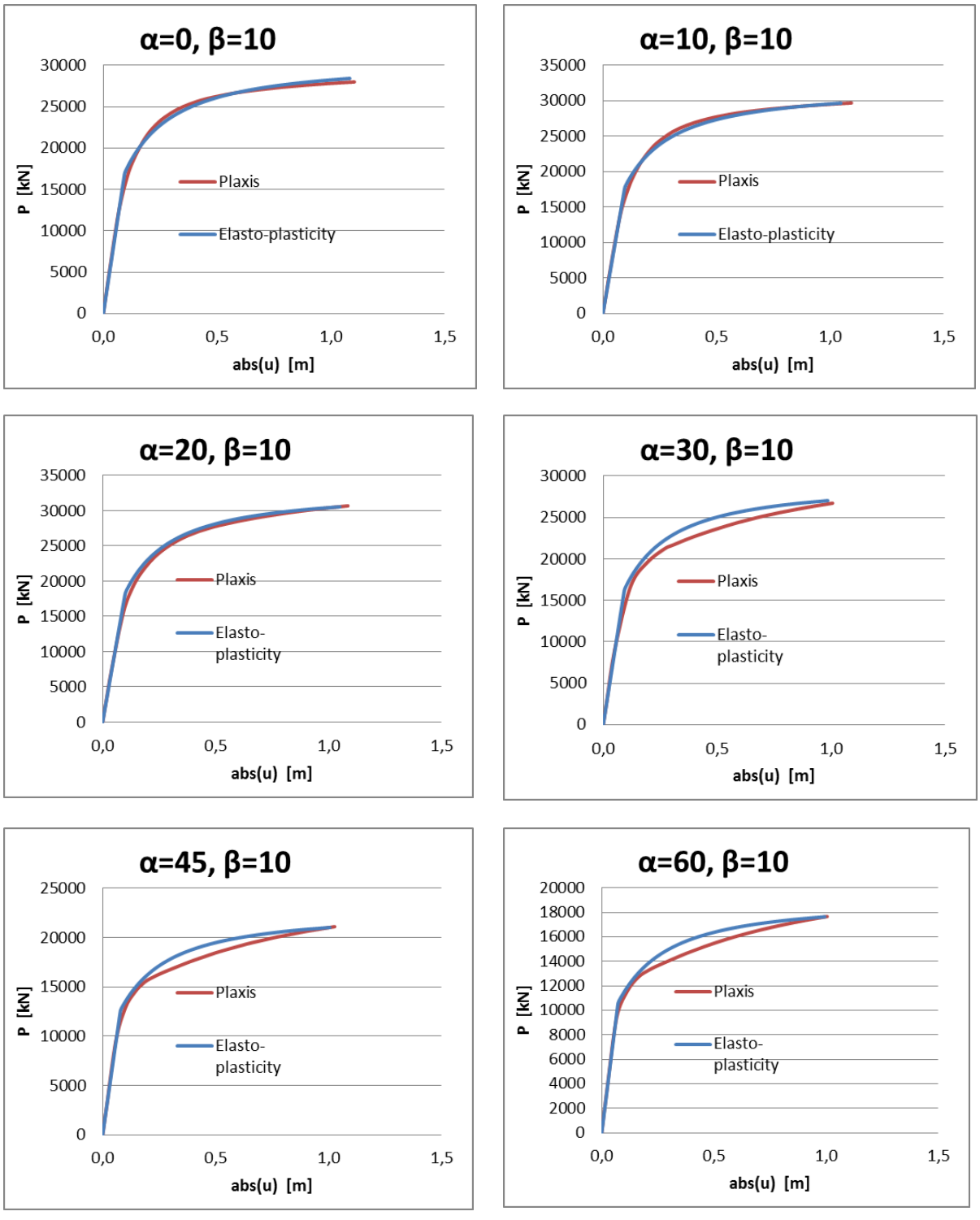

Figure 101 - Elasto-plastic response; Plaxis and empirical results, β=10 degrees

Figure 101 shows the elasto-plastic behavior from Plaxis curves and empirical curves when the torsional angle is 10 degrees. The curve fitting for all the horizontal load cases interpolates the Plaxis

results in a proper way; the tendency is thus for the quality of the curve fitting to increase with the torsional angle β.

6.3.2 Two-way loading

It can be concluded that the elasto-plasticity behaves accurately for proportional loading, especially since the plastic anisotropy of the anchor response is disregarded, and instead optimized as a whole. Since isotropic hardening is assumed, the formulation would, however, not provide realistic results for two-way loading due to the Bauschinger effect. A load cycle in the x-direction is applied to illustrate its limitation.

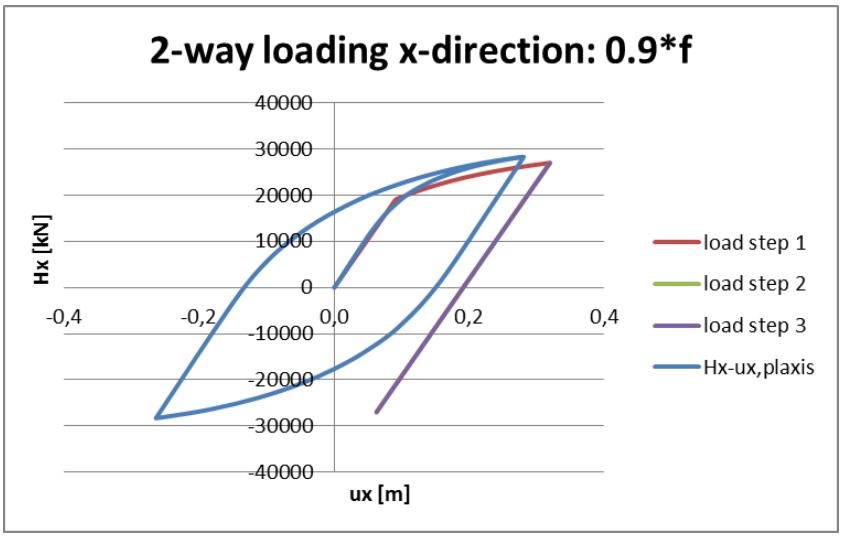

Figure 102 - Load cycle in the x-direction; Plaxis and empirical isotropic response

If cyclic two-way loads were expected, kinematic hardening would clearly be favorable due to the soil parameters applied in this thesis.

6.3.3 Normality

Another interesting aspect of the Plaxis results is whether the normality assumption is applicable at a macro level between padeye loads and padeye displacements. The soil parameters in the thesis impose associate flow at element level since the dilatational angle equaled zero. The question is then whether the normality assumption remains valid after all the elements have been integrated at the global level. Some degree of discretization error will in any case be present, due to the finite element discretization. The yield surface, which the Plaxis results will be compared against, will also contain a degree of error; even though the chosen yield surface provides accurate results, the points are still not interpolated exactly. Plastic displacement vectors in the xz-plane were normalized and plotted against the yield surface when the rotational angle β was zero. The normalized plastic incremental displacements were isolated by subtracting the incremental elastic displacements, obtained from the stiffness matrix, from the total incremental displacements, and then normalized:

$$\{du_{pl}\}_{normalized} = \frac{\{du_{tot}\} - [K]^{-1}\{dQ\}}{\sqrt{(\{du_{tot}\} - [K]^{-1}\{dQ\})^T(\{du_{tot}\} - [K]^{-1}\{dQ\})}} \quad (6.42)$$

The following normality is observed:

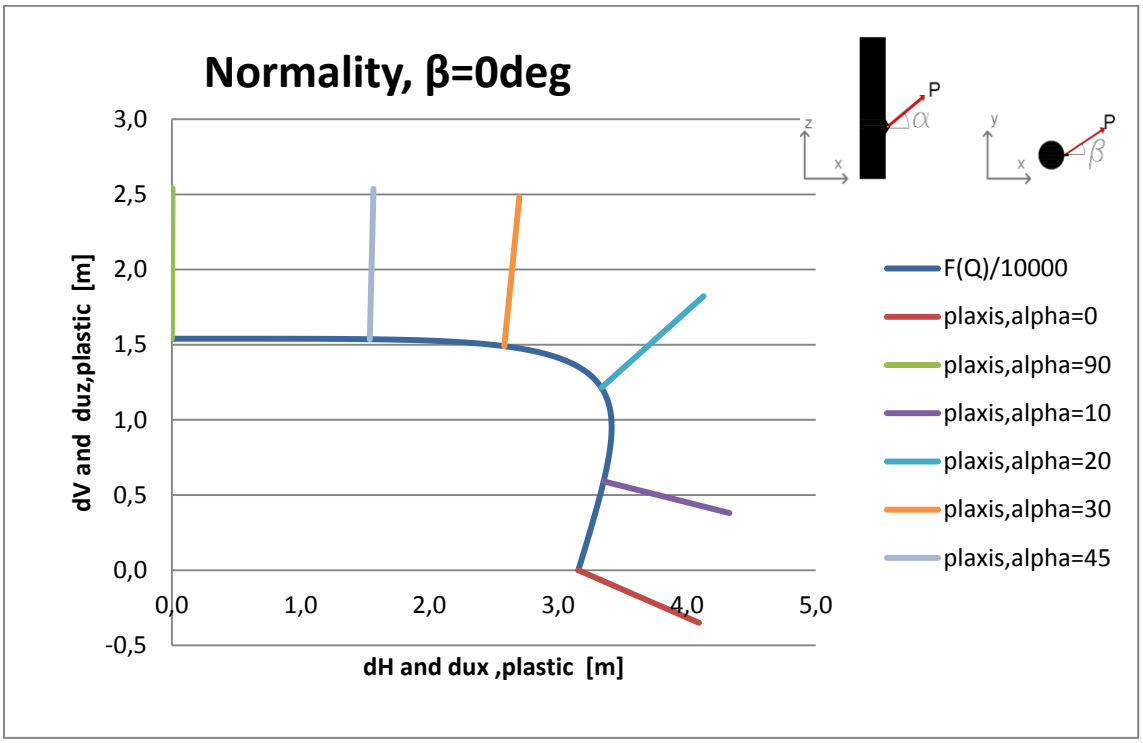

Figure 103 - Normality; plastic displacement vectors

Figure 103 shows that the normality assumption is valid for the global system. The elasto-plastic formulation also assumes associated flow, which means that the plastic displacement increments will be normal to the yield surface.

6.4 Elasto-plasticity: Summary

The elasto-plasticity has been implemented in an Excel spreadsheet. The hardening rule is represented by the hyperbola, and isotropic hardening is assumed. The second yield surface was taken as the yield criterion, with the mobilization factor taken as the state parameter. The results for proportional loading corresponded well, but were not appropriate in relation to two-way loading. The normality assumption was applicable at the global level with respect to padeye loads and padeye deflections.

7 Generalization

In this chapter, the results will be presented in a generalized way. The capacity will first be presented in a non-dimensional way, before showing normalized capacity curves. Thereafter, the focus will be on stiffness. Generalization of elasto-plasticity will then be dealt with. Finally, it will be shown how the generalized response corresponds to suction anchors with aspect ratios L/D equal to three and eight. Note that the generalization is still limited to undrained conditions.

7.1 Non-dimensional results

Non-dimensional results will be presented in the following, thus making the results applicable to situations with other anchor geometries and other soil conditions. It is debatable which parameters the anchor should be generalized with respect to. For horizontal loads, it has been chosen to generalize the results with respect to the width and the length of the anchor, as well as the average shear strength. The generalization should provide a good fit for other anchors as well, since the flow-around mechanism gives the same unit resistance with depth, while for shallow suction anchors, the base shear will compensate somewhat for the decrease in earth pressure resistance. For vertical loading, both the base resistance and the shaft resistance contribute significantly to overall capacity. While the shaft resistance is dependent on both the length and the width of the anchor, the base resistance is not directly dependent on the length, but is dependent on the width to the power of two. The shaft resistance will also be dependent on the roughness of the wall, and might change from project to project. The vertical results will be generalized on the basis of the same parameters as for horizontal loading, and a simple diagram will be presented illustrating how the results may be applicable to other suction anchors. Non-dimensional capacity coefficients are introduced:

$$N_h = \frac{H}{LD\bar{s}_u} \tag{7.1}$$

$$N_v = \frac{V}{LD\bar{s}_u} \tag{7.2}$$

For interaction between horizontal and vertical loads, the non-dimensional coefficient will be obtained by combining equation 4.10 and 4.14.

$$N = \sqrt{{N_h}^2 + {N_v}^2} = \frac{\sqrt{H^2 + V^2}}{LD\bar{s}_u} = \frac{P}{LD\bar{s}_u} \tag{7.3}$$

where P is the magnitude of the failure capacity
N is a non-dimensional factor
L is the length of the anchor
D is the diameter of the anchor
$\bar{s_u}$ is the average undrained strength.

The capacity curves from Plaxis can now be presented in a non-dimensional fashion:

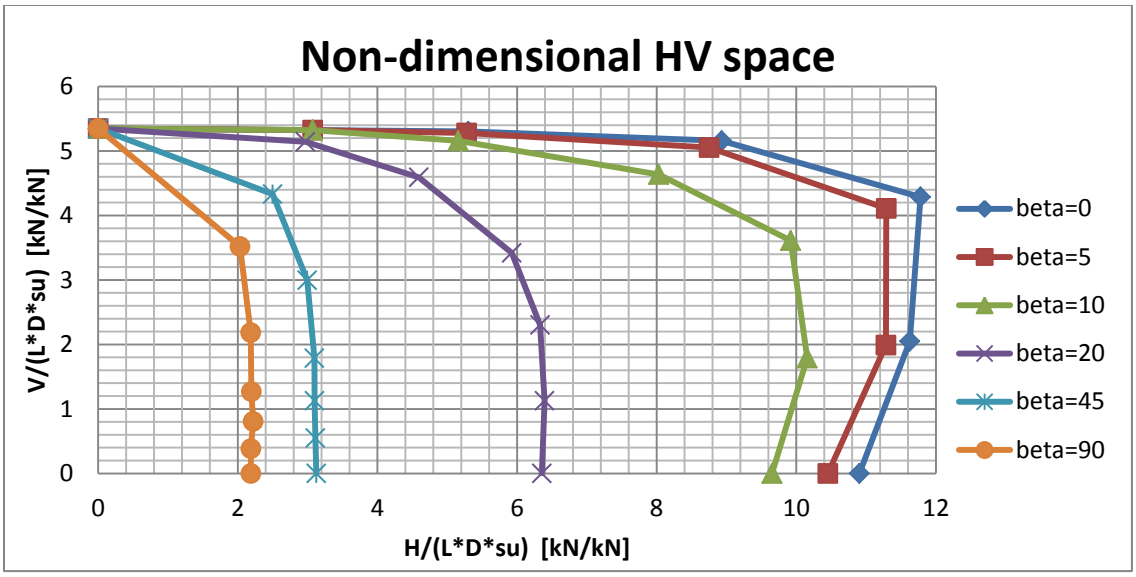

Figure 104 - Non-dimensional HV space

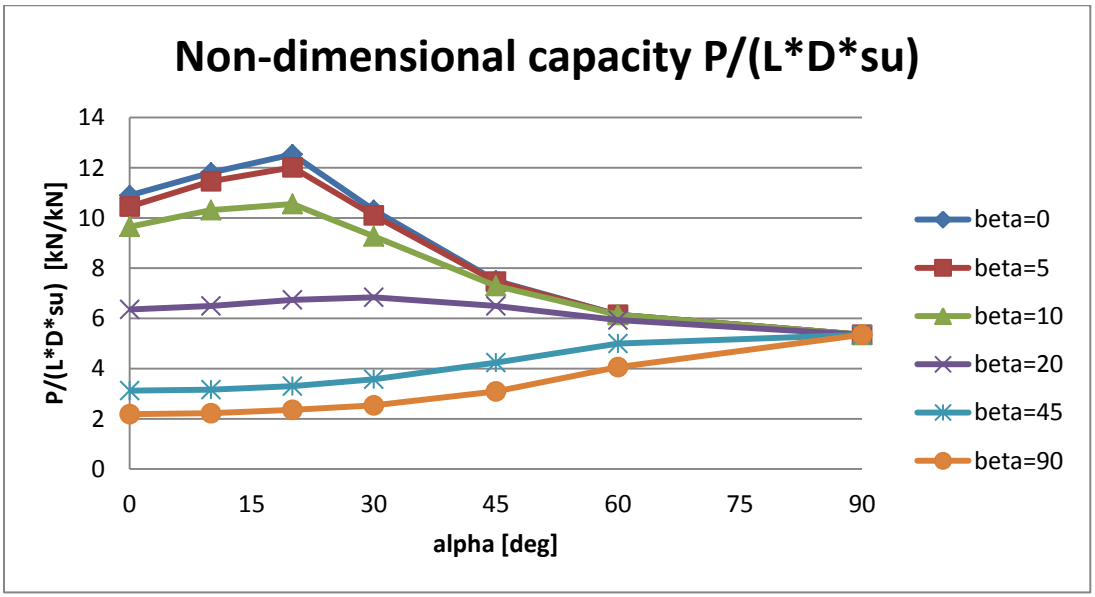

Figure 105 - Non-dimensional capacity

The figures show the capacities in a non-dimensional way, and include the reduction in capacity due to the other force components present. The non-dimensional capacity curves can now be used to calculate capacity for other suction anchors. It should be noted that non-dimensional results will overestimate capacity, due to the discretization error with finite elements. Comparisons against hand calculations show that the vertical and the horizontal loads are overestimated by approximately 10%, while the torsional moment is overestimated by 50%. If the capacity curves are used, these should be adjusted for the discretization error.

The following expression makes the results from the vertical and the inclined loading applicable to other projects:

$$N_v = \frac{V}{LD\bar{s}_u} = \frac{\pi LD\alpha\bar{s}_u + \frac{1}{4}\pi N_c LD^2 s_u(L) + W'}{LD\bar{s}_u} = \pi\alpha + \frac{1}{4}\pi N_c \frac{D}{L}\frac{s_u(L)}{\bar{s}_u} + \frac{W'}{LD\bar{s}_u} \qquad (7.4)$$

It involves three terms; a shaft term, a base term and a weight term. A diagram with the following assumptions is presented below: It is assumed that the weight ratio remains constant, that the ratio between the shear strength at the base and the average shear strength is the same as for this project, i.e. 32kPa/17kPa=1.89, and that the reversed end bearing coefficient is taken to be 9. The following diagram is then obtained, with a roughness factor of the wall equal to r=0.4, 0.6 and 0.8, respectively:

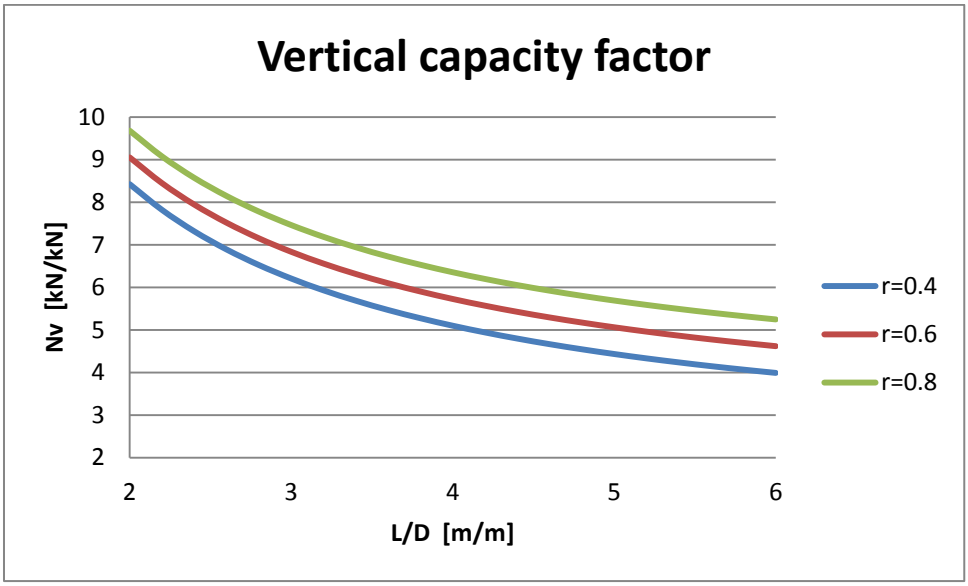

Figure 106 - Vertical capacity factor; wall roughness = 0.4, 0.6, 0.8, Nc=9, W'/(LDsu)=0.54, su(L)/su=1.89

Figure 106 shows that the vertical capacity factor changes significantly depending on the aspect ratio.

7.2 Normalized strength

The Plaxis results in the HV space can be normalized with respect to the maximum horizontal and vertical force components. The maximum horizontal load that can be applied to the system is 38,000kN, while the maximum vertical force is 15,500 kN.

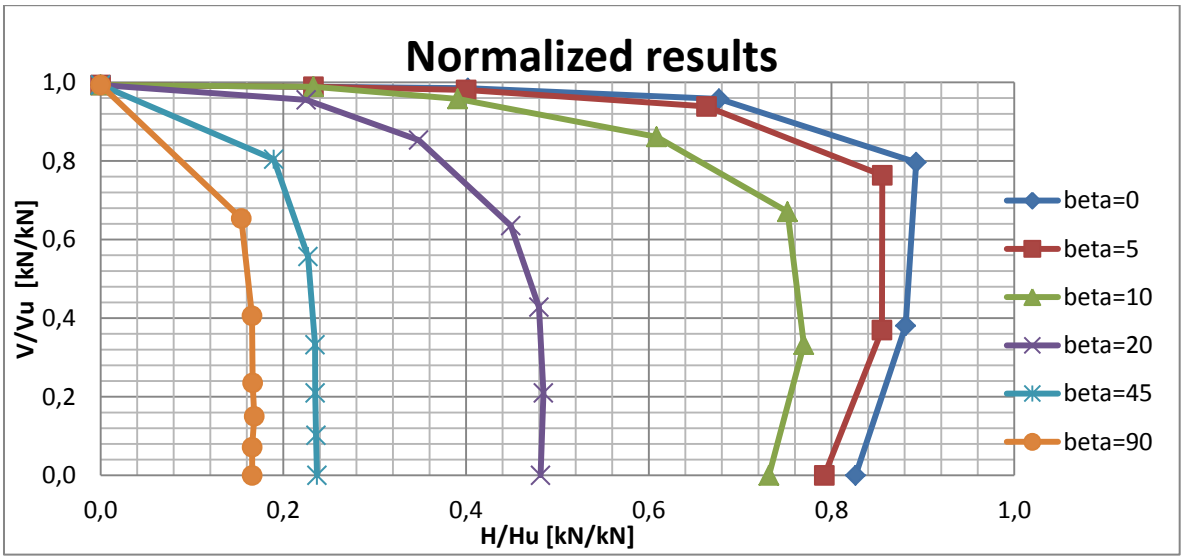

Figure 107 - Normalized results

Figure 107 shows that horizontal loading at the padeye will mobilize the horizontal capacity at about 83%. This means that the vertical distance between the load attachment point and the neutral plane reduces the moment by approximately 17%. The diagram does not capture the normalization due to torsion. A change in the aspect ratio will change of torsional resistance differently than the horizontal. The normalization is thus limited to suction anchors with an aspect ratio equal to 5 for the load cases where the torsional angle is different from zero.

The empirical yield surface will, however, be capable of normalizing all the force components in a proper way. The empirical yield surface interpolated the Plaxis results almost perfectly, and will be a powerful tool in estimating the capacity of suction anchors with an arbitrary geometry and, at least, for normally consolidated clay conditions. The following equation is presented:

$$(\frac{h_x}{1-{m_y}^d})^a + (\frac{h_y}{1-{m_y}^d})^a + v^b + t^c = 1 \qquad (7.5)$$

where a, b c, and d are empirical coefficients, which gave values of 5, 5, 2 and 2, respectively, due to curve fitting
hx, hy, v, t, my and mx are normalized force components, resulting from the following expressions:

$$h_x = \frac{H_x}{H_u}, \qquad h_y = \frac{H_y}{H_u}, \qquad v = \frac{V}{V_u}, \qquad (7.6)$$

$$t = \frac{H_y * e_x}{T_u}, \qquad m_x = \frac{H_y * ez}{M_u}, \qquad m_y = \frac{|H_x * ez - V * ex|}{M_u}$$

The ultimate force components and the eccentricities for a given project can then be inserted into the equations, thus obtaining the capacity surface. The surface can also be presented in the HVT-space:

$$(\frac{h}{1-m^d})^a + + v^b + t^c = 1 \qquad (7.7)$$

where $h = \sqrt{h_x^2 + h_y^2}$ and $m = \sqrt{m_x^2 + m_y^2}$

The latter equation imposes an insignificant adjustment of the original yield surface, since the resultant direction of the moment and the direction of the horizontal force will, in general, not coincide. However, this can safely be disregarded. The normalized HV space with constant torque-mobilization curves will now be shown:

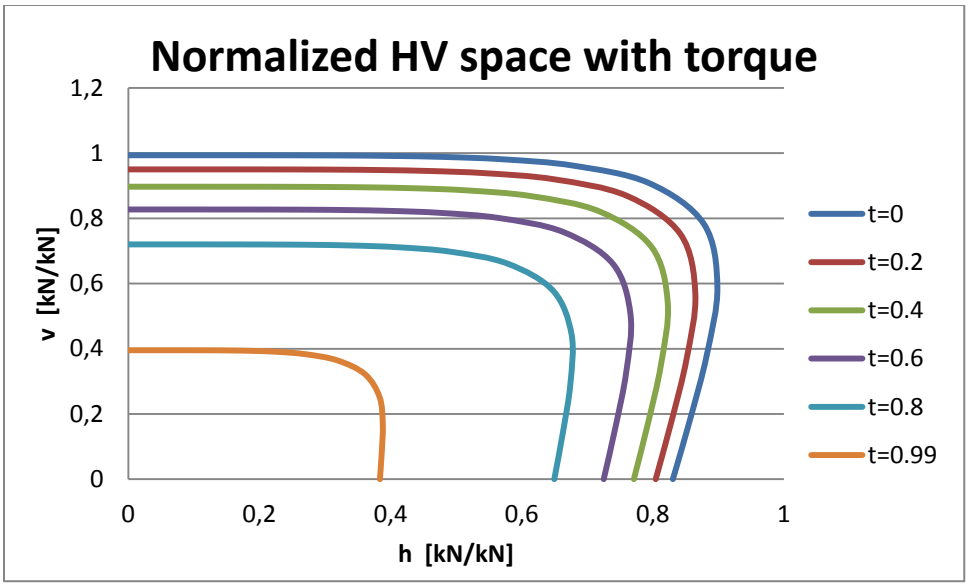

Figure 108 - Normalized HV space with constant mobilized torque

The ultimate force components can be roughly estimated from the following equations:

$$H_u = N_h * LD\bar{s}_u, \tag{7.8}$$

$$V_u = \pi LD\alpha\bar{s_u} + \frac{1}{4}\pi N_c LD^2 s_u(L) + W' \tag{7.9}$$

$$M_u = 2.0 * L^2 D\bar{s}_u \tag{7.10}$$

$$T_u = \frac{1}{2}\alpha * \bar{s}_u * L * \pi * D^2 + \frac{1}{12} * s_u(L) * D^3 + T_{padeye} \tag{7.11}$$

$$e_z = 0.73L - z^* \quad \text{for } \frac{s_{uL}}{\bar{s}_u} = \frac{32kPa}{17kPa} = 1.88 \tag{7.12}$$

where Hu, Vu, Mu and Tu are ultimate force components

N_h is the horizontal capacity factor, which can be given a value in the range of 10-11, although this study has given it a value of 38,000/(30*6*17)=12.4

z* is the distance between the seabed and the load attachment point

e_z is, in this context, the distance from the seabed to the plastic neutral plane minus the distance from the seabed to the padeye

$e_x$is the horizontal distance between the neutral axis and the load attachment point

α is the roughness factor for the shafts

W' is the effective weight of the anchor

Nc is the reverse end bearing capacity factor, often taken to be 9

T_{padeye} is the torsional resistance due to the area of the padeye, which may be disregarded

Note that the equation for the bending moment was derived for a linearly increasing earth pressure resistance per unit length. For situations were the earth pressure per unit length can be considered as constant, the ultimate capacity would be $0.25LH_u$, obtained from limit equilibrium. How the normalized yield surface can be applied in practice, will be showed by varying the padeye location based on the properties addressed by the thesis:

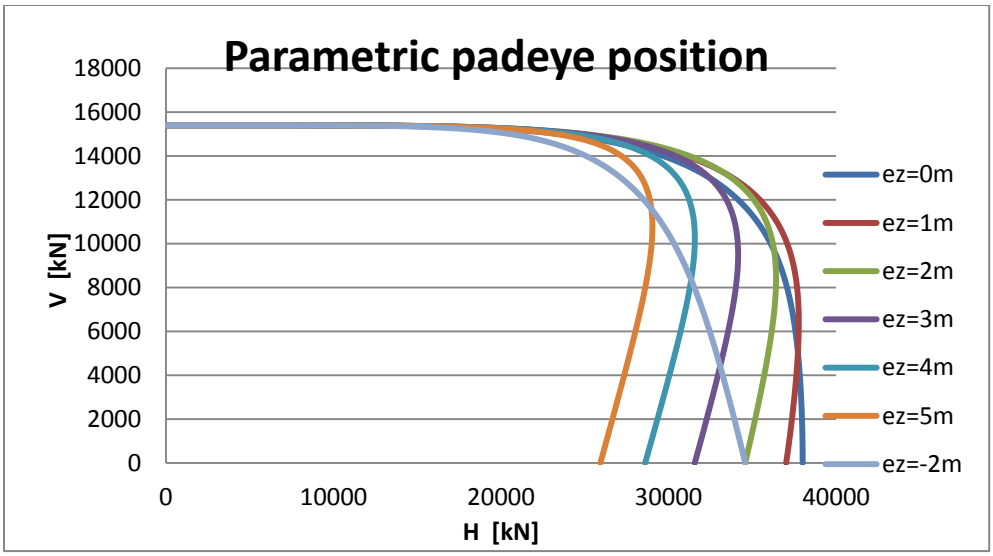

Figure 109 - Parametric padeye positions, ez=0-5 meters

A quite interesting conclusion can be drawn from the figure; that it would be beneficial to lower the padeye position in response to any kind of inclined loading. The vertical plastic eccentricity for this project is 3 meters from the plastic neutral plane. The optimum padeye position for most kinds of inclined loading will be one meter above the neutral plane. Due to horizontal loads, the optimum padeye position will be at the neutral plane; which is the definition of the plastic neutral plane. A padeye position 2 meters below the plastic neutral plane was included as well; the curve shows that an increase in the vertical load causes a larger bending moment, rather than unloading of the bending moment as observed when the padeye position is above the neutral plane. This can also be shown by the constraint loading equations.

It is also interesting to use the empirical yield surface with respect to the hand calculations obtained in this thesis. The ultimate components are inserted in equation 7.6, and compared against the Plaxis results:

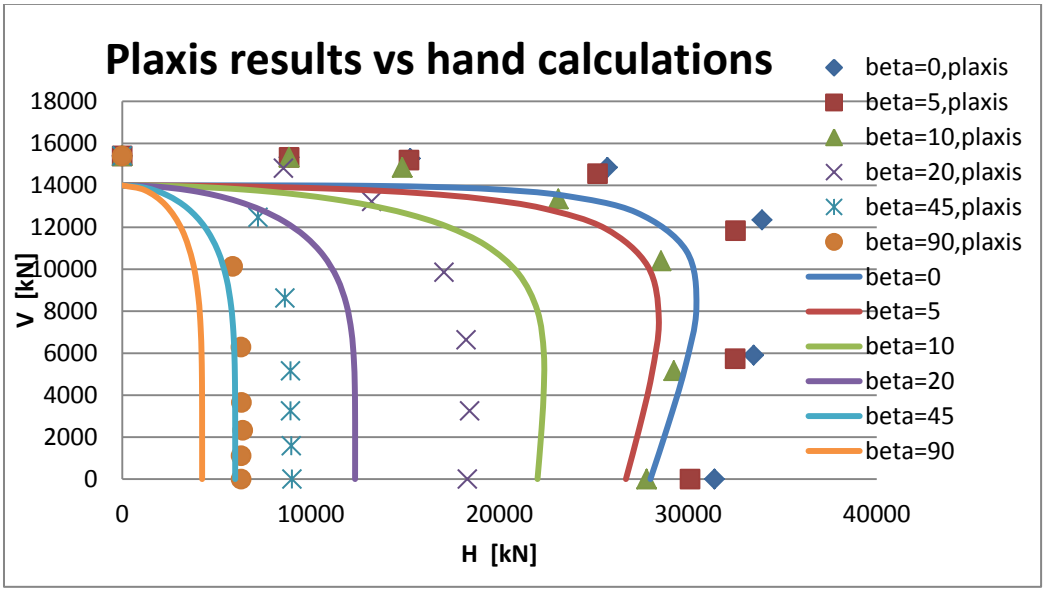

Figure 110 - Plaxis results compared to hand calculations

Figure 110 show that the capacity curves overestimates is entire load space compared to the hand calculations, and that the system is more sensitive in terms of misorientation with respect to the installation.

7.3 Non-dimensional stiffness

It can also be useful to present the stiffness of the system in a non-dimensional manner. It will then be possible to measure the displacements for small loads, and the elasto-plastic stiffness matrix will be given for arbitrary suction anchors (formulas will not be numbered).

Several factors have an influence on the stiffness of the system:

- Soil conditions
- Stiffness profile
- Type of loading
- Geometry of the anchor

The non-dimensional stiffness of the system will be limited to the undrained condition, which implies that the applied loads can be considered short-term loads. When the loads are acting on the system for a sufficiently long period of time, the soil will start to consolidate, and the displacements will be extended without any change in external loading. The stiffness profile of the soil and the geometry of the anchor will obviously have an impact on stiffness. The stiffness profile for this project is as follows:

$$G(z) = n * s_u(z) = 100 * s_u(z) = 200 + 100z \quad [kPa] \tag{7.13}$$

$$K_u \gg G \tag{7.14}$$

where G is the shear modulus
K is the bulk modulus, which can be regarded as infinite, due to the undrained conditions
n is a constant, which implies that G is proportional to the strength

The average shear stiffness will be used in defining the non-dimensional stiffness of the system. The most significant anchor geometries for this project are the length and the diameter of the anchor. It has already been shown that the suction anchor can be considered as rigid, which means that the stiffness of the anchor is much greater than the stiffness of the surrounding soil. The stiffness equation for the system is as follows:

$$\{Q\} = [K]\{u\} \tag{7.15}$$

where $\{Q\}$ is the load vector at the padeye
$[K]$ is the stiffness matrix
$\{u\}$ is the displacement vector at the padeye

It might be convenient for formulation purposes if all terms in the stiffness equation are non-dimensional. This will be accomplished if both the load vector and the displacement vector are non-dimensional. The following generalization can be chosen:

$$\{q\} = \frac{\{Q\}}{L * D * \bar{G}}, \qquad \{d\} = \frac{\{u\}}{D} \tag{7.16}$$

where $\{q\}$ is the non-dimensional load vector determined by the length, the diameter and the average shear stiffness
$\{d\}$ is the non-dimensional displacement vector determined by the diameter

The non-dimensional system equation will then be:

$$\{q\} = [k]\{d\}, \qquad [k] = \frac{[K]}{L * \bar{G}} \tag{7.17}$$

The following non-dimensional stiffness matrix is obtained by insertion:

$$[k] = \begin{bmatrix} 4.14 & 0 & 0.27 \\ 0 & 1.18 & 0 \\ 0.27 & 0 & 2.57 \end{bmatrix} \tag{7.18}$$

The stiffness matrix for a project can then be expressed as follows:

$$[K] = L\bar{G} \begin{bmatrix} 4.14 & 0 & 0.27 \\ 0 & 1.18 & 0 \\ 0.27 & 0 & 2.57 \end{bmatrix} \tag{7.19}$$

Since the shear modulus and the shear strength profile are proportional, the stiffness matrix can also be specified in terms of the proportional factor, the length and the average shear strength:

$$[K] = nL\bar{s_u} \begin{bmatrix} 4.14 & 0 & 0.27 \\ 0 & 1.18 & 0 \\ 0.27 & 0 & 2.57 \end{bmatrix} \tag{7.20}$$

where n is the proportional factor between the shear modulus and the shear strength, which equals 100 for this project

The model applied for the thesis focuses on the ultimate state. A larger soil volume should be applied if the focus is on the stiffness properties. The obtained matrix is for that reason likely to overestimate the stiffness, and should not be used for other projects without adjustment.

The obtained matrix is defined in terms of padeye loads and deflections. The matrix is only suited for other projects if the eccentricities between neutral planes and load attachment points are the same, relative to the anchor geometries. This is highly unlikely, and a stiffness relation in terms of loads and responses at the optimum load attachment point would for that reason be more suited. The optimum load attachment point in this sense is where the three neutral planes intersect. The stiffness matrix at this point can then be transposed to any point at the suction anchor, under the assumption that the anchor can be considered rigid.

The displacements are therefore constrained. The constraint relations between the padeye and the optimum load attachment point will be shown. Both the loads and the displacements will be constrained. The displacement relations are as follows:

$$\begin{Bmatrix} Ux, padeye \\ Uy, padeye \\ Uz, padeye \\ \theta x, padeye \\ \theta y, padeye \\ \theta t, padeye \end{Bmatrix} = \begin{Bmatrix} Ux + ez * \theta y \\ Uy + ez * \theta x + ex * \theta t \\ Uz - ex * \theta y \\ \theta x \\ \theta y \\ \theta t \end{Bmatrix} \quad (7.21)$$

The expression can also be stated the other way around:

$$\begin{Bmatrix} Ux \\ Uy \\ Uz \\ \theta x \\ \theta y \\ \theta t \end{Bmatrix} = \begin{Bmatrix} Ux, padeye - ez * \theta y \\ Uy, padeye - ex * \theta x - ex * \theta t \\ Uz, padeye + ex * \theta y \\ \theta x, padeye \\ \theta y, padeye \\ \theta t, padeye \end{Bmatrix} = \begin{Bmatrix} Ux, padeye - ez * \theta y, padeye \\ Uy, padeye - ex * \theta x, padeye - ex * \theta t, padeye \\ Uz, padeye + ex * \theta y, padeye \\ \theta x, padeye \\ \theta y, padeye \\ \theta t, padeye \end{Bmatrix}$$

(7.22)

There is a similar relation between forces applied at the padeye and force resultants:

$$\begin{Bmatrix} Hx \\ Hy \\ V \\ Mx \\ My \\ T \end{Bmatrix} = \begin{Bmatrix} Hx, padeye \\ Hy, padeye \\ Vpadeye \\ Hy * ez \\ Hx * ez - V * ex \\ Hy * ex \end{Bmatrix} \quad (7.23)$$

The equation states that an applied force vector at the padeye can be expressed as a transformed force vector at the optimum load attachment point.

One assumption is required to determine the stiffness matrix; namely an uncoupled stiffness matrix at the optimum load attachment point. Due to the padeye plate, the system is not fully symmetrical, but this will not influence the coupling significantly. The neutral plane normal to the z-axis is defined as the plane that causes translations without rotations due to horizontal loads. The uncoupling assumption is thus appropriate. Plaxis results confirm the assumption.

$$\begin{Bmatrix} Hx \\ Hy \\ V \\ Mx \\ My \\ T \end{Bmatrix} = \begin{bmatrix} Kh & 0 & 0 & 0 & 0 & 0 \\ 0 & Kh & 0 & 0 & 0 & 0 \\ 0 & 0 & Kv & 0 & 0 & 0 \\ 0 & 0 & 0 & Km & 0 & 0 \\ 0 & 0 & 0 & 0 & Km & 0 \\ 0 & 0 & 0 & 0 & 0 & Kt \end{bmatrix} \begin{Bmatrix} Ux \\ Uy \\ Uz \\ \theta x \\ \theta y \\ \theta t \end{Bmatrix} \quad (7.24)$$

$$\begin{Bmatrix} Ux \\ Uy \\ Uz \\ \theta x \\ \theta y \\ \theta t \end{Bmatrix} = \begin{bmatrix} 1/Kh & 0 & 0 & 0 & 0 & 0 \\ 0 & 1/Kh & 0 & 0 & 0 & 0 \\ 0 & 0 & 1/Kv & 0 & 0 & 0 \\ 0 & 0 & 0 & 1/Km & 0 & 0 \\ 0 & 0 & 0 & 0 & 1/Km & 0 \\ 0 & 0 & 0 & 0 & 0 & 1/Kt \end{bmatrix} \begin{Bmatrix} Hx \\ Hy \\ V \\ Mx \\ My \\ T \end{Bmatrix} \quad (7.25)$$

where Kh is the horizontal stiffness
Hv is the vertical stiffness
Km is the bending stiffness
Kt is the torsional stiffness

The stiffness coefficients are determined from load-deflection curves.

Inserting the constraint equations, the following system equations are obtained between the padeye load and the deflection:

$$\begin{Bmatrix} Ux, padeye \\ Uy, padeye \\ Uz, padeye \end{Bmatrix} = \begin{bmatrix} \frac{1}{K_H} + \frac{(ez)^2}{K_M} & 0 & -\frac{ex * ez}{K_M} \\ 0 & \frac{1}{K_H} + \frac{(ez)^2}{K_M} + \frac{(ex)^2}{K_T} & 0 \\ -\frac{ex * ez}{K_M} & 0 & \frac{1}{K_V} + \frac{(ex)^2}{K_M} \end{bmatrix} \begin{Bmatrix} Hx, padeye \\ Hy, padeye \\ Vpadeye \end{Bmatrix} \quad (7.26)$$

And finally:

$$K, padeye = \begin{bmatrix} \frac{1}{K_H} + \frac{(ez)^2}{K_M} & 0 & -\frac{ex * ez}{K_M} \\ 0 & \frac{1}{K_H} + \frac{(ez)^2}{K_M} + \frac{(ex)^2}{K_T} & 0 \\ -\frac{ex * ez}{K_M} & 0 & \frac{1}{K_V} + \frac{(ex)^2}{K_M} \end{bmatrix}^{-1} \quad (7.27)$$

where K_H, K_V, K_M and K_T are the elastic stiffness coefficients resulting from the force components of the anchor

ex is the eccentricity in the x-direction between the padeye and the neutral plane; 3.75 m

ez is the eccentricity in the z-direction between the padeye and the elastic neutral plane, which is defined as the plane that causes translation without rotation due to horizontal loads.

The padeye position is not restricted to a fixed position under this formulation, which makes the formulation general with respect to anchor geometry and the stiffness profile of the soil.

Note that the definition of ez in terms of capacity was different from the elastic definition. In the latter case, ez was the eccentricity between the load attachment point and the plastic neutral plane, which is the plane that provides the largest horizontal capacity.

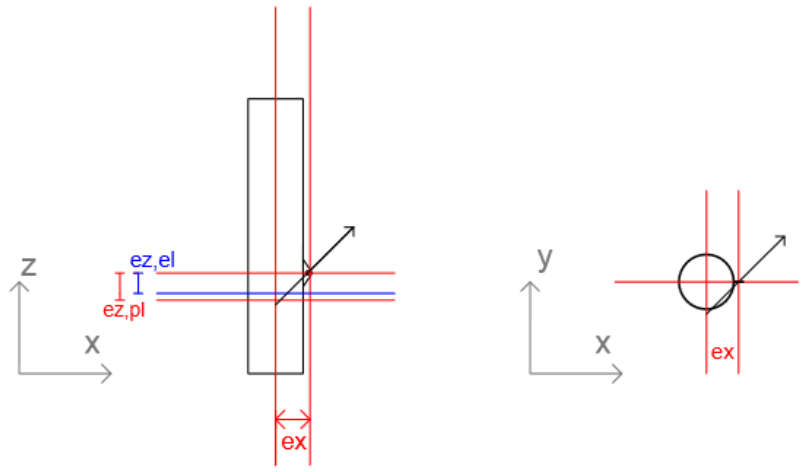

Figure 111 - The suction anchor; difference between elastic and plastic eccentricities

The planes will, in general, not coincide. This can be illustrated by comparing the responses caused by an applied bending moment, where the soil is first modeled as linearly elastic, then as elasto-plastic, with the moment giving rise to a failure mechanism. The plastic eccentricity, which was presented in section 4.3, is 3.0 meters, while the elastic eccentricity is 2.2 meters.

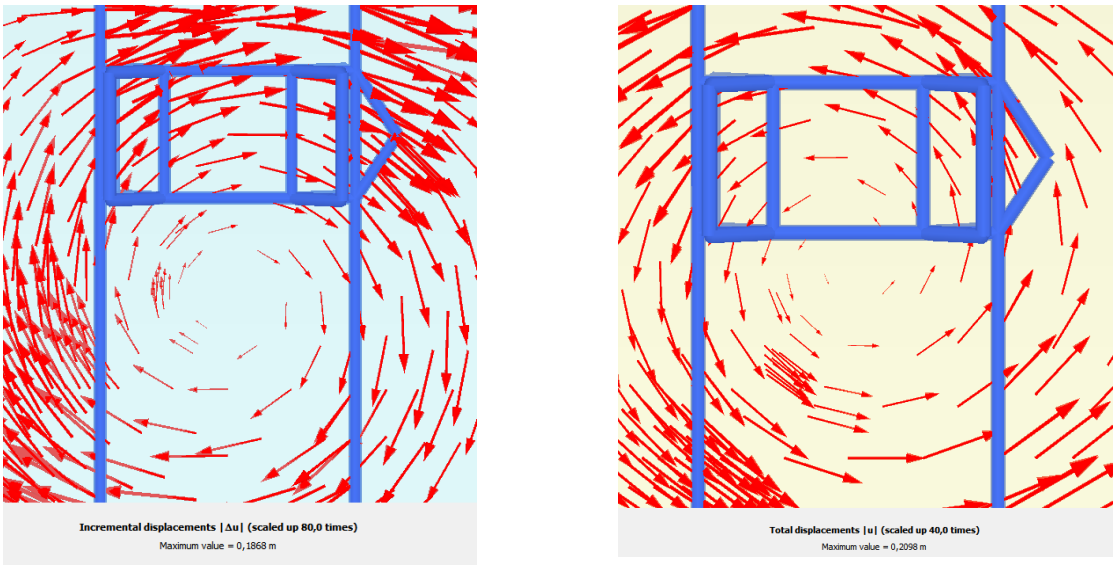

Figure 112 - Response caused by applied bending moment; (a) failure mechanism, (b) linearly-elastic response

7.4 Elasto-plasticity generalization

The generalization presented so far can also be implemented in the elasto-plastic formulation. A generalized stiffness matrix, yield surface and normalized ultimate strength have been presented, and only the hardening remains to be determined. The hardening rule in the elasto-plastic formulation was obtained by curve fitting between the mobilization factor and the displacements. If the displacements are normalized, for instance with respect to the diameter of the anchor, the hardening rule is also obtained. Other considerations, like for instance whether kinematic hardening should be applied, will be the same for the conventional formulation.

The spreadsheet made for the project was implemented in a generalized way; the empirical coefficient, the ultimate components, the stiffness matrix and the eccentricities can all be easily changed for purposes of another project. However, the hardening rule needs to be determined.

8 Discussion

In this chapter, the results from the project will be evaluated. Firstly, the modeling considerations will be discussed. The reliability of the model and the results will be addressed, before the tendencies of the results will be presented. These include tendencies of the load-deflection curves, the failure mechanisms and the capacity curves. The empirical data will then be addressed, before discussing generalization.

8.1 Modeling considerations

Modeling considerations are examined prior to analyses. Simplifications will always be necessary, however it is important that the physical behavior remains modeled in a proper way, and that operation of the model is not too time-consuming. This section discusses some of these considerations.

Geometrical nonlinearities due to combined loading have been disregarded. The geometrical nonlinearities will have a large impact on some of the load cases; when a vertical pull-out load is applied, the contact area between the shaft and the soil will decrease, implying that a lower capacity will be obtained when implementing the nonlinearity, due to displacement boundaries. The geometrical load boundaries will also be important for the load cases where a large torsional moment is present. The failure mechanism of the anchor is then governed by anchor rotation about the z-axis. During rotation, the misorientation of the anchor will decrease, implying that the torque will also decrease. This response will only be obtained if geometrical nonlinearities are included. Geometrical nonlinearities will only be important for large deformations, and will be more time-consuming to model. The load cases where the load vectors were pointed in the y- and z-directions were additional to conventional analyses, calculated with the updated mesh option. The updated mesh option will update the mesh due to the deformed geometry, and the strain measure is also different; nonlinearities between displacements and strains will be accounted for. The following response was obtained:

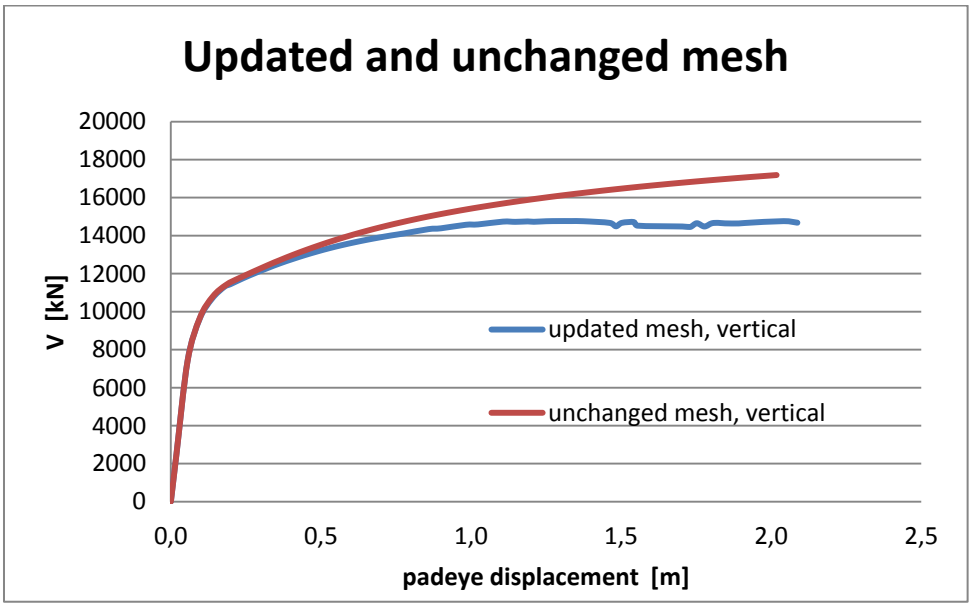

Figure 113- Updated and unchanged mesh for vertical load case

Figure 113 shows that the updated mesh gives a reduced capacity for the vertical load case. The difference between the curves is especially prominent when the padeye has deflected about one meter. The updated mesh calculation had approximately reached the failure state when deflected one meter and a further increase in load would result in infinite deflections; the system is singular. The ultimate capacity with the updated mesh is 14,700 kN, which means that the conventional calculation, with failure taken as one meter padeye deflection, overestimated the capacity by about 5%. It might thus be appropriate to adjust the failure definition for purposes of later projects. For instance, failure can be defined as D/10. It should be noted that the simple material model; the linearly-elastic Mohr-Coulomb model, does not account for softening at large shear strains. This means that in reality, the true load-deflection curve would most likely have an even larger softening response. The load case where loading was pointed in the y-direction gave the following response under the updated mesh option, compared to the conventional calculation:

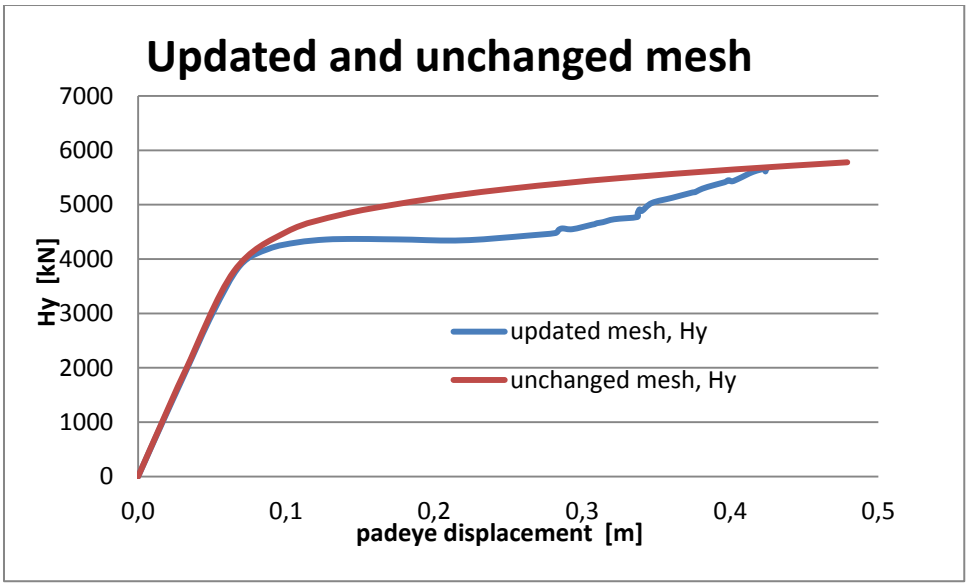

Figure 114 - Updated and unchanged mesh for the load case pointed in y-direction

Figure 114 shows that the geometrical nonlinearities are of benefit to the system for large torsional angles. After a horizontal yielding plateau, the system shows a hardening behavior due to a decrease in the eccentricity between the loading line and the neutral axis.

The response changes significantly for large deflections. However, since failure was defined as one meter padeye deflection, the analysis without geometrical nonlinearities will have a limited impact. A smaller deformation criterion might be adopted in order to limit the differences between the analyses. Alternatively, a correction factor, which accounts for the nonlinearity, can be introduced.

Soil volume of the model is also a major consideration. In order to achieve the best failure mechanisms, it is important that the element mesh is dense where the failure mechanisms are expected. However, it would also be important, due to stiffness, to have a sufficiently large soil volume, in order to capture deflections that will have an influence on the response. The main focus of the thesis was on capacity. Soil volume of the model was therefore chosen for reasons of capacity, and the stiffness obtained should either be adjusted to reflect the distances to the boundaries, or calculated by other methods.

The geometry of the anchor was modeled with few simplifications. The ring stiffeners used for installation stability purposes were omitted, since the installation phase in Plaxis does not simulate the self-weight and the suction penetration. Compression forces in the anchor due to installation will therefore not be present. This simplification makes the modeling of the anchor more convenient.

37 load combinations were chosen for the main analyses. The load cases were designed to map the entire load space with regard to tensile forces. Even though large torsional angles due to misorientation are highly unlikely, these were still included in order to obtain the response in the entire load space. The load cases were constructed in such a way as to have the most load cases where needed. For instance, since the failure mechanism and the vertical capacity were more or less exactly the same whether the inclination angle was 60 or 90 degrees, there was no need for load cases in between these. The same can be said for the torsional angle; most of the capacity due to torsional resistance was mobilized when the torsional angle was 20 degrees, and only one torsional angle was placed in between, in order to obtain a smoother capacity surface.

8.2 Reliability of the model

In any numerical study, it is essential to evaluate the reliability of the results. The reliability of the results can first be compared against hand calculations. Mesh refinements are also essential for the finite element model. It will also be important to examine the responses, and look for unphysical behavior. This can for instance be irregularities in the load-deflection curves, unreasonable changes in stress states caused by loads, unrealistic failure mechanisms, interface mobilization, continuity of the anchor, etc. If any one of the said responses gives answers that cannot be explained, something is likely to be wrong with the model.

The results from the hand calculations gave answers that differed slightly from the corresponding load cases in Plaxis with the model of 20,500 soil elements:

Force component	Hand calculation	Plaxis	Error [%]
Horizontal [kN]	34,000	38,000	12
Vertical [kN]	14,000	15,400	10
Bending moment [kNm]	204,000	230,000	12
Torque [kNm]	16,000	23,800	49

Figure 115 - Results from hand calculations and from Plaxis

Figure 115 compares the hand calculated results to the results from Plaxis. The results from Plaxis are 10-12% overestimated compared to the corresponding hand calculation, except for the torsional moment, which is overestimated by 49%. It should be noted that the hand calculations are not exact solutions either, and that 10-12% does not mean that the discretization error of the model is 10-12%. Nonetheless, the discretization error of the torsional resistance is more than one would desire. As described in the theoretical chapter, the resistance caused by torsion is due to three features; the shaft resistance, the base resistance, and the resistance due to the padeye. The shaft resistance contributed most significantly. It was suspected that the large error was caused by the padeye, and a load case with torsion, where the padeye plate was not activated was executed.

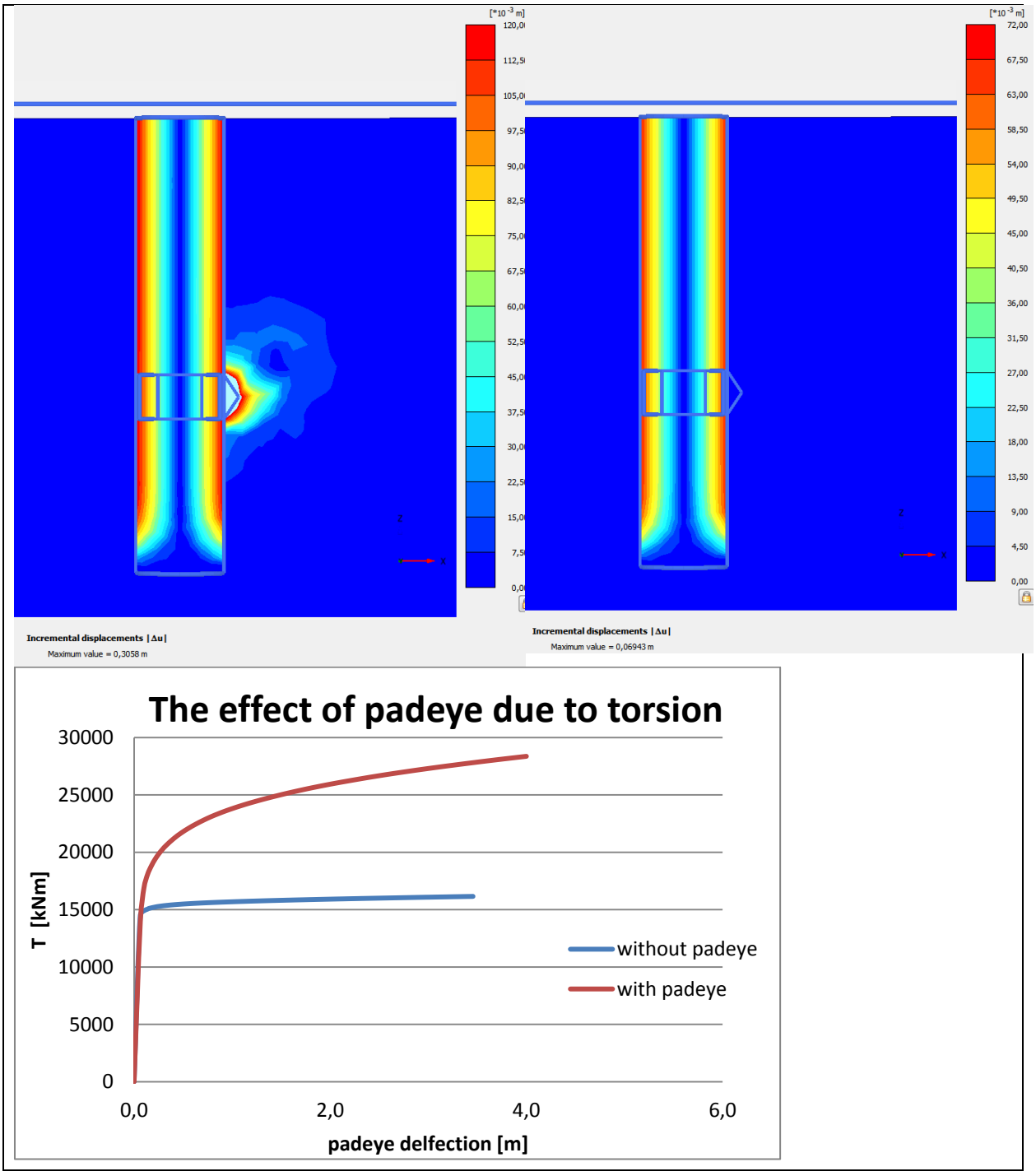

Figure 116 – Respnce with and without the padeye with respect to torsion, inc disp; (a) with padeye (b) without padeye, (c) response

Figure 116 shows that the torsional stiffness will be calculated accurately if the padeye is not activated. At failure, a flow around mechanism is developed around the padeye. It turns out that a very fine mesh is needed around the plate in order to compute the response accurately. It would for that reason be better to not model the padeye at all. Equivalent padeye loads could rather be applied as a set of load vectors.

The mesh refinements could indicate that the model offered a good convergence. However, a slow convergence rate might also be a possibility, which could convey a false impression. five mesh refinements were executed and compared in section 4.7. It was observed that the horizontal load

case for mesh refinement number three actually gave a more accurate answer than mesh refinement number four. Due to the nature of finite elements, the response should move towards correct results when the number of elements increases in a uniform way. However, the users of Plaxis 3D have limited control over the meshing options, and the difference between the mesh refinements will not be increased in a uniform way. Uniform mesh refinements are not desired either, since it is more important to increase the density of the mesh where the critical response is located. In the case of mesh refinement number four, the elements where positioned in a way that favored the vertical failure mechanism more than the horizontal one. Since mesh refinement number four was substantially more time consuming and provided only slightly better accuracy, mesh refinement number three was chosen for the main analyses. Mesh number five was too time-consuming for this parametric study.

8.3 Observations of the capacities

The capacity curves were given in terms of a load vector applied at the padeye position, with the inclination angle and the torsional angle mapping the entire load space for tensile forces. First of all, it was shown that the horizontal load-deflection curves for horizontal loading had a better defined yield plateau than for vertical loading. This can be explained by the failure mechanisms; the horizontal failure mechanism, consisting of the wedge mechanism at the upper part, and the flow-around mechanism at the lower part, is closer to a rigid slip-plane mechanism than the vertical failure mechanism, which mechanism involves soil movements into the anchor, thus implying that the capacity will constantly increase with larger deflections. However, when the geometrical nonlinearities are included, the softening response will dominate after approximately one meter of padeye deflection.

The failure mechanisms can roughly be divided into four categories:

- Vertical failure mechanism, where the soil plug translates with the anchor, and a classical reversed end-bearing capacity is observed.
- Horizontal failure without anchor rotation, involving a wedge mechanism that gradually converts into the flow-around mechanism.
- Horizontal translations with rotations. The rotation center is then close to the anchor. The horizontal capacity is then reduced in order to maintain equilibrium due to the moment.
- Torsional failure mechanism, where the anchor rotates about the z-axis.

Vertical failure dominates when the load inclination angle is 30 degrees or more, and the maximum horizontal force is observed when the inclination angle is 20 degrees, due to the unloading of the bending moment, which is more beneficial than vertical loading with respect to capacity. When the inclination angle is zero, the rotation center is almost at the anchor base, and the soil at the lower part is not mobilized in any significant way. A torsional angle of 5 degrees does not reduce the capacity to any large extent; when the inclination angle is zero, the capacity is reduced by 4%. When the torsional angle is 10 degrees, the maximum reduction is present when the inclination angle is 20 degrees; the capacity has now been reduced by 16%, which is a relatively large reduction. When the torsional angle is further increased to 20 degrees, only half of the capacity is left for the horizontal load cases, and the capacity and the corresponding failure mechanism are totally governed by the torsion. It should be noted that torsional angles of these magnitudes are definitely not realistic in practice, and are primarily included to obtain a complete surface, and to gain a deeper

understanding of the system. The torsional resistance of the system is likely to overestimate capacity more than the other force components, when considering comparisons against hand calculations. This implies that the true torque reduction will be increased. However, the normalized curves are still applicable, where the ultimate forces are either hand calculated or obtained by numerical studies. The normalized curves will then interact with all six force components in a constrained way, since the loads will be applied at the padeye.

8.4 Evaluation of the empirical data

Two different yield surfaces were considered, both focusing of the relation between the six different force components of the system. Constrained loading conditions were then introduced, and both yield surfaces could be expressed in terms of three unknowns. The three translational forces were chosen, since these are the forces imposed as a load vector at the padeye. When the three padeye forces are represented in space, information will actually be provided on all the six force components. The first yield surface had a simpler form than the second one, but the second provided by far the most accurate curve fitting. Comparisons between them can be made, assuming mobilization f=1:

Yield Surface 1	Yield Surface 2
$(\frac{H_x}{H_u})^a + (\frac{H_y}{H_u})^a + (\frac{V}{V_u})^b + (\frac{M_x}{M_u})^c + (\frac{M_y}{M_u})^c + (\frac{T}{T_u})^d = 1$	$(\frac{H_x}{H_u\left(1-\left(\frac{M_y}{M_u}\right)^d\right)})^a + (\frac{H_y}{H_u\left(1-\left(\frac{M_x}{M_u}\right)^d\right)})^a + (\frac{V}{V_u})^b + (\frac{T}{T_u})^c = 1$
Simple form ☺	Slightly more extensive ☹
Easy to implement in elasto-plasticity ☺	Time consuming to implement ☹
Provides a decent curve fitting ☺	Provides excellent curve fitting ☺
No physical foundation ☹	Has a physical foundation ☺

Figure 117 - Comparisons yield surfaces

Both capacity curves are quite good, although the second yield surface is more accurate. Optimizing showed that the average expected error for a load case was only 0.7%.

The elastic stiffness coefficients were obtained by examination of load cases in the three normal directions, where linear curves were curve fitted based on the initial response of the load-deflection curves. The flexibility and stiffness matrix were then obtained. It was chosen to measure the loads and the displacement directly from the padeye. It would also be possible to load and measure the response at the optimum load attachment point, and then transpose the response to the padeye. The latter method would be generally applicable to other projects, although the eccentricity ez would also be needed.

The curve fitting between the mobilization factor and the plastic deflections was based on elasto-plasticity. Power law, Voce rule and hyperbola were all considered. The hyperbola offered the most

suitable shape and gave the best estimation through the method of least squares. The same hardening rule with the same coefficients was applied in all directions.

Elasto-plasticity in terms of padeye loads and deflections was implemented by isotropic hardening, although specific load cycles in Plaxis indicated that kinematic hardening would be more appropriate. However, since the anchor will be loaded from a mooring chain, two-way loads are not likely due to loads from the platform.

8.5 How to apply the generalized results

Generalized results were presented in chapter 7. The generalized results can be applied in other projects, and a lot of time can be saved. However, it is important to first understand that the non-dimensional results obtained from this study are upper bound solutions. Adjustments and comparisons are thus required. The second curve-fitted capacity curve will, however, be a powerful tool, which can be used to estimate the capacity surface. The fact that the generalization directly reflects the padeye loads makes it especially practical to use.

The values of the stiffness coefficients are likely to be overestimated, because of the distances to the boundaries, which is just in excess of six diameters. In other words, the model is sufficiently large for capacity, but will overestimate stiffness.

The generalized stiffness matrix, in which the eccentricities can easily be changed from project to project, may also be useful; if the various stiffness coefficients are known, the stiffness matrix with regard to any padeye position can be obtained. However, the elastic neutral plane is then needed.

9 Conclusion & further work

9.1 Conclusion

Capacity curves in Plaxis 3D for a suction anchor with an aspect ratio equal to 5 have been obtained, based on ultimate loads applied at the padeye, which is located approximately 2/3 of the anchor length from the seabed. The thesis is limited to undrained loading conditions. A parametric variation of the load directions has been executed, so that the entire loading space defined by tensile forces has been studied. The capacity curves show that misorientation of the anchor caused by the mooring plane will reduce capacity by about 3% when such misorientation is 5 degrees and 12% when such misorientation is 10 degrees, due to horizontal and slightly inclined loads. There is in practice no reduction in capacity when the inclination angle is 45 degrees or more, for realistic torsional angles.

Two empirical curves have been determined in order to make the results applicable to other projects. The empirical formulas combine the six force components present in terms of padeye loads. Due to eccentricities to the three neural planes, there will be three forces and three moments present. One of the empirical curves interpolated all the Plaxis results with an average error of 0.7%, consisting of four empirical coefficients. This yield surface has been used to derive an elasto-plastic formulation, in terms of padeye loads and padeye deflections. Isotropic displacement hardening has been applied, and a general Excel spreadsheet has been established. The elastic and the plastic relationships have been determined from curve fitting.

The results have been further generalized, so that the work in the thesis can be used for other suction anchors. The normalized capacity curve, in particular, can be efficiently used in other projects.

The reliability of the results is mainly acceptable, although the torsional moment is overestimated by about 50%, due to the discretization error. It is showed that the overestimation is mainly due to the flow around mechanism of the padeye.

9.2 Further work

In further work, the numerical modeling can be executed in other programs, a kinematic hardening formulation can be constructed and experiments based on combined loading can be performed. More advanced material models can be applied, and capacity curves can be designed for drained conditions as well.

References

Andersen, K.H. & Jostad H.P. (2002). Shear Strength Along Outside Wall of Suction Anchors in Clay after Installation. *Proceedings of the Twelfth (2002) ISOPE Conference.*

Andersen, K.H. & Jostad H.P. (2004). Shear Strength Along Inside of Suction Anchor Skirt Wall in Clay. *Offshore Technology Conference,* Paper OTC 16844

Andersen K.H., Murff, J.D., Aubeny,C., Randolph, M.F., Supachawarote, C., Sharma, P., Jostad H.P., Clukey E.C., Erbrich, C. T. & Hansen, B. (2005). Suction anchors for deepwater applications. *Proceedings of the International Symposium. on Frontiers in Offshore Geotechnics (IS-FOG 2005)*, 3-30

Aubeny, C & Murff, D. (2005). Suction Caissons & Vertically Loaded Anchors: Design Analysis Methods*, Department of Civil Engineering Texas A&M University*

Augustin, L.C. (1828). Exercises de mathématiques. Paris: Bure frères

Cook, R.D., Malkus, D.S., Plesha, M.E. & Witt, R.J. (2001). *Concepts and Applications of Finite Element Analysys* (4nd edition). New York: John Wiley & Sons

Coulomb, C.A. (1776). *Essai sur une application des règles de maximis & minimis à quelques problèmes de statique, relatifs à l'architecture.* Paris: De l'Imprimerie Royale

Dean E.T.R. (2009). *Offshore Geotechnical Engineering.* London: Thomas Telfond

Deng, W. & Carter J. P. (2000). A Theoretical Study of the Vertical Uplift Capacity of Suction Caissons. *Proceedings of the 10th International Offshore and Polar Engineering conference*, 342-349

El-Sherbiny, R.M., Vanka, S.K., Olson, R.E. & Gilbert, R.B. (2005) Capacity of suction caissons under inclined loading in normally consolidated clay. *Proceedings of the International Symposium. on Frontiers in Offshore Geotechnics (IS-FOG 2005)*, 281-287

Irgens, F. (2008*). Continuum Mechanics*. Berlin: Springer

Leffler, Pattarozzi, W.L., Sterling R. & Gordon. (2011*). Deepwater Petroleum Exploration and Production* (2nd Edition). Tulsa: PennWell.

Jeanjean, P. (2006). Setup Characteristics of Suction Anchors for Soft Gulf of Mexico Clays: Experience from Field Installation and Retrieval. *Offshore Technology Conference,* Paper OTC 18005

Jostad H.P & Andersen, K.H. (2002). Foundation Design of Skirted Foundations and Anchors in Clay. *Offshore Technology Conference,* Paper OTC10824

Kreyszig, E. (2006). *Advanced Engineering Mathematics* (9nd edition). Singapore: John Wiley & Sons

Lee, Y.C., Tjok, K.M. & . Audibert J.M.E (2005). Lessons learned from several suction caisson installation projects in clay. *Proceedings of the International Symposium. on Frontiers in Offshore Geotechnics (IS-FOG 2005)*, 235-239

Martin, C. M. & Randolph, M. F. (2006). Upper-bound analysis of lateral pile capacity in cohesive soil. *Geotechnique*, *56*(2), 141–145

Nordal, S. (2010). *Lecture Notes PhD course BA8304 Soil Modeling.* Trondheim: Norwegian University of Science and Technology, Geotechnical Division

Plaxis. (2010). *Plaxis reference manual.*

Plaxis. (Unknown). *About Plaxis - History.* Obtained 25th April 2013, http://www.plaxis.nl/page/4863/

Poisson, D.S (1833). Traite de mecanique (2nd edition). Paris: Bachelier, Imprimeur-Libraire

Poulos, H.G., & Davis, E.H. (1974). Elastic Solutions for Soil and Rock Mechanics. New York: John Wiley

Randolph, M.F.,.O'Neill M.P., Stewart D.P. & C.Erbrich. (1998). Performance of Suction Anchors in Fine-Grained Calcareous Soils. *Offshore Technology Conference.* , Paper OTC8831

Randolph, M.F. & Gourvenec, S. (2011). *Offshore Geotechnical Engineering*. New York: Spon Press

Rankine, W. (1857). On the stability of loose earth. *Philosophical Transactions of the Royal Society of London, 147, 9-27*

Supachawarote, C., Randolph, M.F. & Gourvenec S. (2004). Inclined Pull-out Capacity of Suction Caissons. *Proc. Int. Symp. Offshore Polar Eng., 2*, 500-506

Taiebat, H.A. & Carter, J.P. (2005). A failure surface for caisson foundations in undrained soils. *Proceedings of the International Symposium. on Frontiers in Offshore Geotechnics (IS-FOG 2005)*, 289-295

Terzaghi, K. (1943). *Theoretical Soil Mechanics.* New York: John Wiley and Sons

Thorel, L., Rault, G., Garnier, J. & Bisson, A. (2005). Vertical uplift capacity of suction caisson in clay. *Proceedings of the International Symposium. on Frontiers in Offshore Geotechnics (IS-FOG 2005)*, 273-279

Wilson, J.F. (2003). Dynamics of Offshore Structures (2nd edition). New Jersey: John Wiley & Sons

Wood, D.M. (2009). *Soil Mechanics; A One-Dimensional Introduction.* Cambridge: Cambridge University Press

Young, T. (1845). A course of lectures on natural philosophy and the mechanical arts. London: Taylor and Walton

Zdravkovic, L. & Potts, D.M. (2005). Parametric finite element analyses of suction anchors. *Proceedings of the International Symposium. on Frontiers in Offshore Geotechnics (IS-FOG 2005)*, 297-302

Zienkiewicz, O.C., Taylor, R.L. & Zhu, J.Z. (2005). *The Finite Element Method: Its Basis and Fundamentals* (6. edition). USA: Elsevier

Zienkiewicz, O.C. & Taylor, R.L. (2005). *The Finite Element Method for structural mechanics* (6. edition). USA: Elsevier

10 Attachments

Attachment A 113

Attachment B 114

Attachment C 115

Attachment D 116

Attachment E 117

10.1 Attachment A - Horizontal capacity (Deng & Carter, 2000)

Course increments, showed as an ilustration

z [m]	Nps	Su(z)	q(z) [kN/m]	v(z)	M(z)
0	2,35	2	28,2	28,2	28,2
1	4,76	3	85,7	113,9	142,1
2	6,46	4	155,1	269,0	411,2
3	7,66	5	229,8	498,9	910,0
4	8,51	6	306,2	805,1	1715,1
5	9,10	7	382,2	1187,3	2902,4
6	9,52	8	456,9	1644,2	4546,6
7	9,81	9	530,0	2174,2	6720,8
8	10,02	10	601,4	2775,6	9496,4
9	10,17	11	671,2	3446,8	12943,2
10	10,27	12	739,7	4186,5	17129,7
11	10,35	13	807,0	4993,5	22123,2
12	10,40	14	873,4	5866,9	27990,1
13	10,43	15	939,0	6805,9	34796,0
14	10,46	16	1004,1	7810,0	42606,0
15	10,48	17	1068,7	8878,7	51484,7
16	10,49	18	1132,9	10011,6	61496,2
17	10,50	19	1196,9	11208,4	72704,6
18	10,50	20	1260,6	12469,0	85173,7
19	10,51	21	1324,2	-19647,8	109715,7
20	10,51	22	1387,7	-18260,2	91455,5
21	10,51	23	1451,0	-16809,1	74646,4
22	10,52	24	1514,3	-15294,8	59351,6
23	10,52	25	1577,6	-13717,2	45634,4
24	10,52	26	1640,8	-12076,4	33558,0
25	10,52	27	1704,0	-10372,3	23185,7
26	10,52	28	1767,2	-8605,1	14580,6
27	10,52	29	1830,4	-6774,8	7805,8
28	10,52	30	1893,5	-4881,2	2924,6
29	10,52	31	1956,7	-2924,6	0,0
30	10,52	32	2924,6	0,0	0,0
		Vmax [kN]=	33441,0	-44189,9	Mst

10.2 Attachment B - Incremental displacements, horizontal planes

Incremental displacements for horizontal planes, located at z=-5m, z=-10m and z=-15m

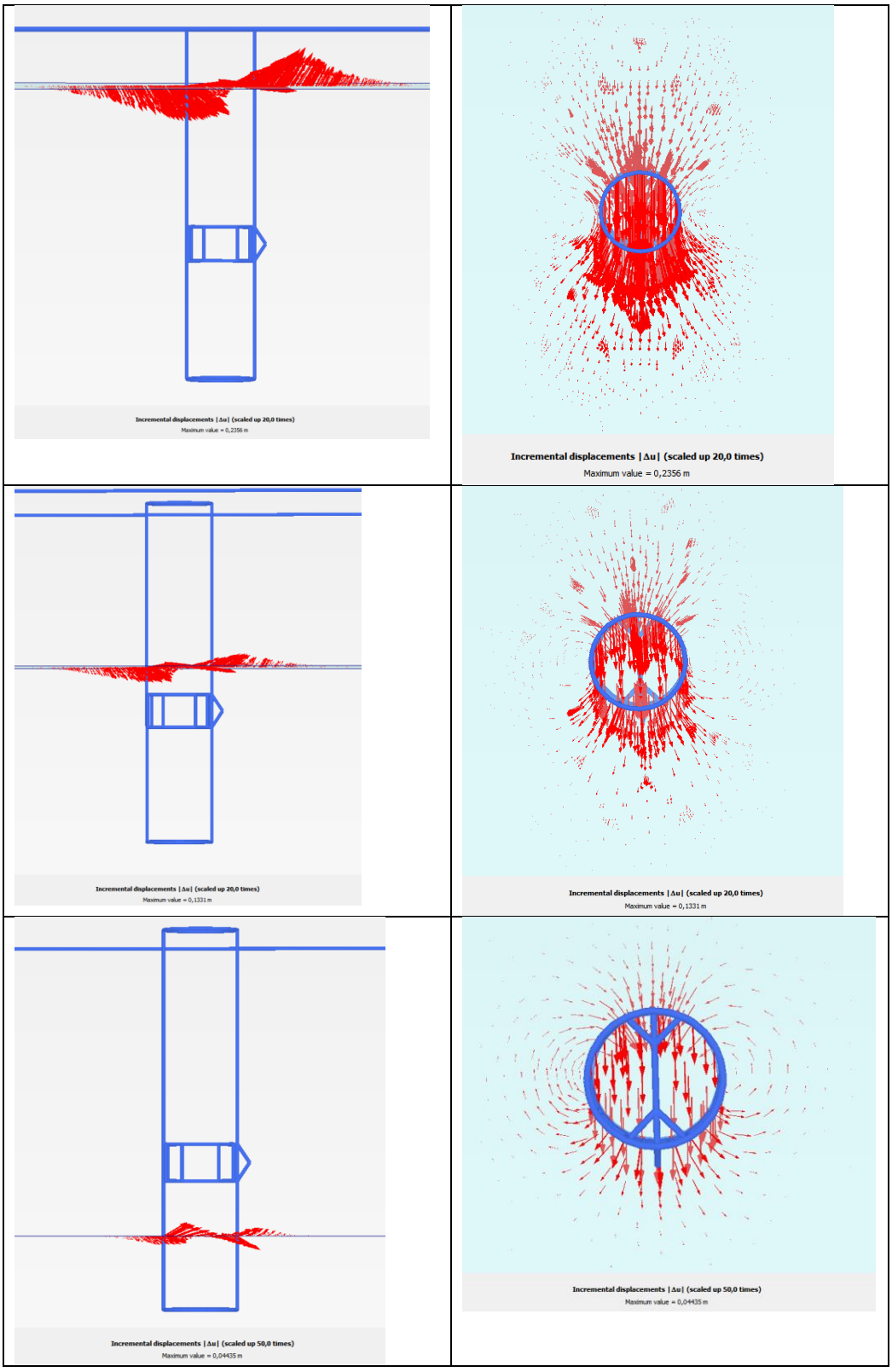

10.3 Attachment C - Flow around mechanism padeye, incremental displacements

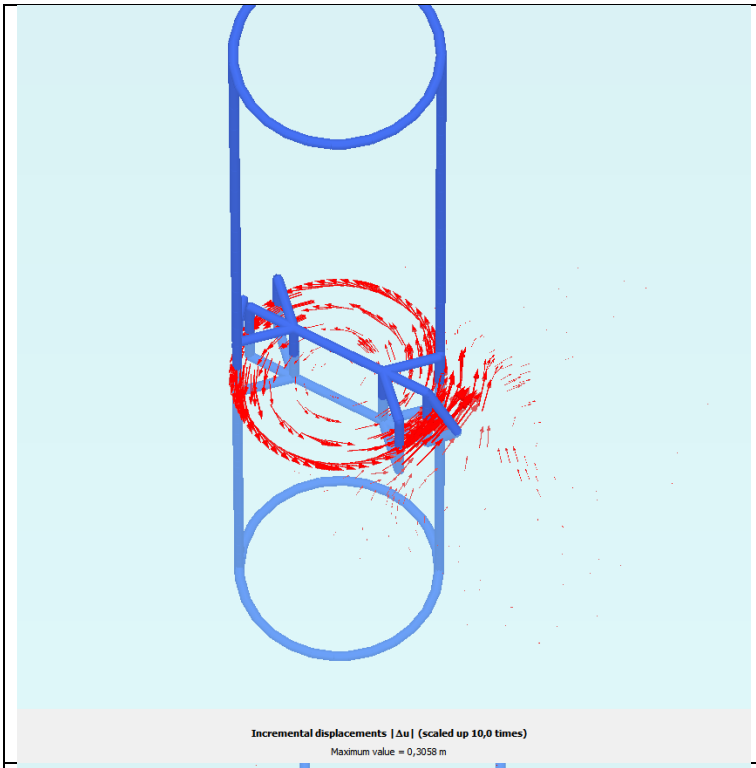	Horizontal plane, z=-19m.
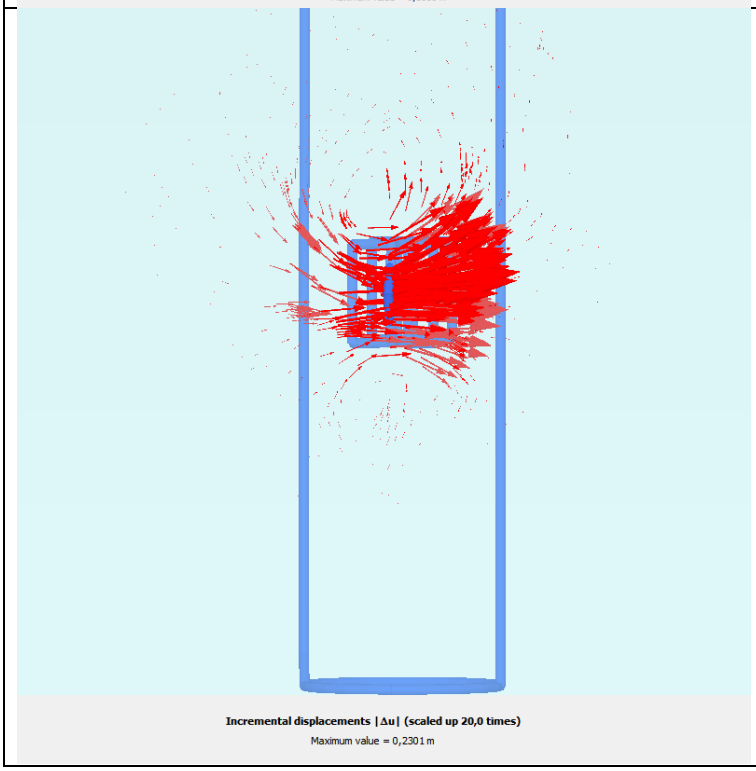	yz-plane, x=3.5m.

10.4 Attachment D - Example elasto-plasticity

Input:

Imput, ceofficients:	
Type	Value
fo []	0,6
a []	5,0
b []	5,0
c []	2,0
d []	2,0
Hu [kN]	38000
Vu [kN]	15400
Mu [kNm]	230000
Tu [kNm]	23800
ex [m]	3,75
ez [m]	3
k1 []	2,056
k2 []	0,393

Input, load history

Load step	**dHx**	**dHy**	**dV**
1	15000	0	0
2	-35000	0	0
3	45000	0	0
4	-53000	0	0
5	58000	0	0
6	-61000	0	0
7	62500	0	0
8	0	0	0
9	0	0	0
10	0	0	0
tot	31500	0	0

Stiffness matrix:

	211443	0	13744
K [kN/m]=	0	60000	0
	13744	0	130893

Flexibility matrix:

	4,76E-06	0	-5,00E-07
F [m/kN]=	0	1,67E-05	0
	-5,00E-07	0	7,69E-06

Output:

output	Final	Load step 1	Load step 2	Load step 3	Load step 4	Load step 5	Load step 6	Load step 7	Load step 8	Load step 9	Load step 10
f* []		0,475	0,634	0,792	0,887	0,951	0,982	0,998	0,998	0,998	0,998
f []	0,998	0,600	0,634	0,792	0,887	0,951	0,982	0,998	0,998	0,998	0,998
alpha [deg]	0,00	0	0	0	0	0	0	0	0	0	0
beta [deg]	0,00	0	0	0	0	0	0	0	0	0	0
abs(Q) [kN]	31500	15000	20000	25000	28000	30000	31000	31500	31500	31500	31500
Qmax [kN]	31560	31560	31560	31560	31560	31560	31560	31560	31560	31560	31560
(u)pl [mm]	861,793	0,0	14,2	124,8	275,6	493,3	701,6	861,8	861,8	861,8	861,8
ux,el [mm]	150,0	71,4	-95,2	119,0	-133,3	142,9	-147,6	150,0	150,0	150,0	150,0
uy,el [mm]	0,0	0,0	0,0	0,0	0,0	0,0	0,0	0,0	0,0	0,0	0,0
uz,el [mm]	-15,8	-7,5	10,0	-12,5	14,0	-15,0	15,5	-15,8	-15,8	-15,8	-15,8
ux,pl [mm]	72,5	0,0	-11,0	85,2	-38,4	126,7	-2,8	72,5	72,5	72,5	72,5
uy,pl [mm]	0,0	0,0	0,0	0,0	0,0	0,0	0,0	0,0	0,0	0,0	0,0
uz,pl [mm]	-26,3	0,0	4,0	-30,9	13,9	-45,9	1,0	-26,3	-26,3	-26,3	-26,3
ux [mm]	222,5	71,4	-106,2	204,3	-171,8	269,6	-150,4	222,5	222,5	222,5	222,5
uy [mm]	0,0	0,0	0,0	0,0	0,0	0,0	0,0	0,0	0,0	0,0	0,0
uz [mm]	-42,0	-7,5	14,0	-43,4	27,9	-60,9	16,5	-42,0	-42,0	-42,0	-42,0
abs(u)[mm]	226,5	71,8	107,1	208,8	174,0	276,4	151,3	226,5	226,5	226,5	226,5

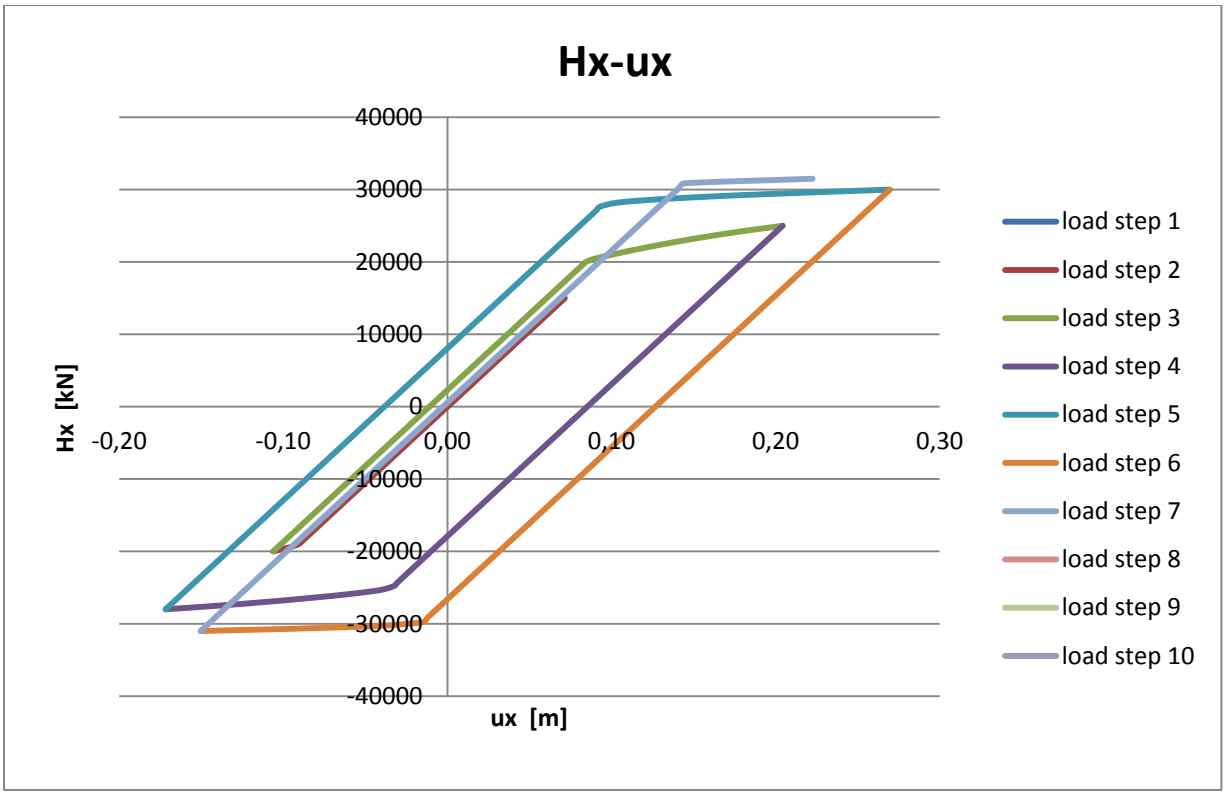

10.5 Attachment E - Deflection space Plaxis, β=0